2022

# Observation of Novel Phases of Quantum Matter Beyond Topological Insulator

Sabin Regmi
*University of Central Florida*

# OBSERVATION OF NOVEL PHASES OF QUANTUM MATTER BEYOND TOPOLOGICAL INSULATOR

by

SABIN REGMI
B.S. Tribhuvan University, Nepal, 2011
M.S. Tribhuvan University, Nepal, 2015

A dissertation submitted in partial fulfilment of the requirements
for the degree of Doctor of Philosophy
in the Department of Physics
in the College of Sciences
at the University of Central Florida
Orlando, Florida

Fall Term
2022

Major Professor: Madhab Neupane

# ABSTRACT

Because of the unique electronic properties, intriguing novel phenomena, and potentiality in quantum device applications, the quantum materials with non-trivial band structures have enticed a bulk of research works over the last two decades. The experimental discovery of the three-dimensional topological insulators (TIs) - bulk insulators with surface conduction via spin-polarized electrons - kicked off the flurry of research interests towards such materials, which resulted in the experimental discovery of new topological phases of matter beyond TIs. The topological semimetallic phase in Dirac, Weyl, and nodal-line semimetals is an example, where the classification depends on the dimensionality, degeneracy, and symmetry protection of the bulk band touching. The field of topology has extended to the materials that possess non-trivial topological states at/along lower-dimensional regions of the crystals as well. A class of such materials is the higher-order topological insulator in which both bulk and surface are insulating, but symmetry-protected conducting channels can appear along the hinges or corners of the crystal. Recently, significant focus has been given to the study of the interplay among various physical parameters such as topology, geometry, magnetism, and electronic correlation. Kagome systems have emerged as a fertile ground to study the interaction among such parameters in a material class. Charge density wave (CDW) order in quantum materials remains an important topic of study given its co-existence or competence with superconductivity and magnetic ordering.

In this dissertation, we study the electronic structure of quantum material systems beyond TIs, particularly the lanthanide element-based and correlated systems, by utilizing state-of-art angle-resolved photoemission spectroscopy with collaborative support from first-principles calculations and transport and magnetic measurements. The lanthanide-based materials are interesting because of the possible magnetic ordering and electron correlations that the lanthanide $4f$ electrons may bring into the table. Our work on the Europium-based antiferromagnetic material $\mathrm{EuIn_2As_2}$ high-

lights this material as a promising ground to study the interplay of different kinds of topological orders including higher-order topology with magnetism. Temperature-dependent measurements reveal a band splitting near the Fermi level below the antiferromagnetic transition. Another study on the samarium-and neodymium-based materials $\mathrm{SmSbTe}$ and $\mathrm{NdSbTe}$ shows the presence of multiple nodal lines that remain gapless even in the presence of spin-orbit coupling. We also studied a van der Waals kagome semiconductor $\mathrm{Nb_3I_8}$, where we observed flat and weakly dispersing bands in its electronic structure. These bands are observed to be sensitive to light polarization and originate from the breathing kagome plane of niobium atoms. Next, our study in Gadolinium-based van der Waals material $\mathrm{GdTe_3}$ shows the presence of a momentum-dependent CDW gap and the presence of antiferromagnetic ordering that could prove important to study the interaction of CDW and magnetic orders in this material. Overall, the works under this dissertation reveal the electronic properties in correlated systems that range from insulator to metals/semimetals and from topological insulator to topological semimetals, kagome semiconductor, and CDW material.

Dedicated to my parents - Bodha Narayan Regmi and Parbati Regmi, my wife - Ashmita Sharma Regmi and my Nephews - Alexa Sharma, Shanvi Poudel, Aniza Sharma, and Aayansh Poudel

# ACKNOWLEDGMENTS

This wonderful academic journey would not have been possible without the support of some wonderful people. This thesis would be incomplete without acknowledging them for their support in so many ways.

I would like to begin by expressing my sincere gratitude to my advisor *Dr. Madhab Neupane* for providing me a wonderful opportunity to undertake this endeavor. From being a role model as an able and talented researcher to helping me to dig out my potential as a researcher, he has been a constant driving force throughout this academic journey. It were his systematic training, proper guidance, and constant encouragement that brought me into the path of doing the right things in scientific research. I will always be thankful to him for providing freedom to learn and explore novel ideas, for being patient during my development as a researcher, and not to forget, for his immense help outside the academic world.

I would like to say thank you to my dissertation committee members, *Dr. Talat S. Rahman*, *Dr. Yasuyuki Nakajima*, and *Dr. Alexei Fedorov*, for their assistance and advisement.

I am also grateful to all the members of Neupane group, past and present, for their support. It was a pleasure working together with these intelligent minds. I would like to thank *Gyanendra Dhakal*, with whom I spent most of the lab time, shared laughs, and enjoyed productive conversations, for his assistance not only in research but also in life outside research. Him and *Md Mofazzel Hosen* taught me the basic of the experiments and data analysis as well as helped me during different phases of my projects. I am thankful to *Anup Pradhan Sakhya*, who was a source of diverse knowledge and my beamline partner most of the times, for his support on and off the research field. Thank you to *Firoza Kabir* for being there for help when needed. I would like to acknowledge *Yangyang Liu* for helping us with time-resolved experimental set-up and experiments. Thanks

should also go to *Christopher Sims*, *Klauss Dimitri*, *Milo Sprague*, *Mazharul Islam Mondal*, *Iftakhar Bin Elius*, *Robert Smith*, *Hector Vazquez*, *William Neff*, *Luis Persaud*, *Alexis Agosto*, and *Nathan Valadez* for their support.

My projects would not have been possible without the support of some wonderful research collaborators. I am thankful to *Dr. Dariusz Kaczorowski* at Polish Academy of Sciences and *Dr. Xiaodong Xu* and his group at University of Washington for sending us high-quality crystals for measurements. I am grateful to *Dr. Arun Bansil* at Northeastern University and his group for providing us with first-principles calculations. I am equally grateful to *Dr. Peter Oppeneer* and his group at Uppsala University as well as *Dr. Ting Cao* and his group at University of Washington for their computational results. I would also like express my gratefulness to *Dr. Krzysztof Gofryk* at Idaho National Laboratory for providing electric transport and magnetic measurements. Many thanks to *Dr. John Mitchell* and his group at Argonne National Laboratory (for high-quality single crystals), *Dr. Andrzej Ptok* at Polish Academy of Sciences (for calculations), *Dr. Amit Agarwal* and his group at Indian Institute of Technology Kanpur (for calculations), *Dr. Nirmal Ghimire* at George Mason University (for crystals), and *Dr. Filip Ronning* and *Dr. Eric Bauer* at Los Alamos National Laboratory (for crystals).

I would like to extend my sincere thanks to *Dr. Sun-Kwan Mo*, *Dr. Alexei Fedorov*, and *Dr. Jonathan Denlinger* at the Advanced Light Source in Lawrence Berkeley National Laboratory, *Dr. Makoto Hashimoto* and *Dr. Donghui Lu* at the Stanford Synchrotron Radiation Lightsource in SLAC National Accelerator Laboratory, and *Dr. Nicholas Clark Plumb*, *Dr. Ming Shi*, *Dr. Hang Li*, and *Dr. Sailong Ju* at Swiss Light Source for their beamline assistance.

To my parents, *Bodha Narayan Regmi* and *Parbati Regmi*, thank you for showing me good examples and for providing unconditional love, trust, support, and encouragement. This dissertation is dedicated to your hard work in upbringing and educating me. A special mention to my wife, *Ash-*

*mita Sharma Regmi*, for being supportive and always on my side. I would also like to remember my sisters *Sangita Regmi Dhital* and *Samjhana Regmi Poudel*, brothers-in-law *Suman Dhital* and *Yadav Poudel*, and nephews *Alexa Sharma*, *Shanvi Poudel*, *Aniza Sharma*, and *Aayansh Poudel*.

# TABLE OF CONTENTS

# LIST OF FIGURES

# LIST OF TABLES

# CHAPTER 1: INTRODUCTION

The field of condensed matter physics and materials science is ever growing with the discovery of new phases in matter and new materials with exciting and unique properties. The recent experimental realization of novel topological phases in a wide class of materials has not only provided the low-energy condensed matter counterparts of particles that have long been a part of high-energy physics, but also those which have no high-energy physics analog. Rather than some local order parameters, these phases of matter are defined by some topology and the properties of the materials exhibiting such phases would remain robust against any transformations or perturbations as long as the topology remains intact. The history of topological phase in matter goes back to the discovery of Quantum Hall effect (QHE) by Von Klitzing *et al.* in 1980 where by using a Hall setup for two-dimensional electron gas in sufficiently low temperature and high magnetic field, plateaus were observed in the Hall conductivity [1, 2]. The field soon expanded with the discovery of the topological insulators (TIs) [3, 4], topological semimetals (TSMs) [5, 6, 7], topological superconductors [8] and beyond. In recent times, understanding of the interaction between various physical parameters or orders such as topology, geometry, electronic correlations, magnetism, superconductivity, charge density waves, etc. in materials has enticed a significant research interest. In this thesis work, we have investigated on the electronic structures of quantum material systems, in which one or more of these parameters or orders are present. For this purpose, we chose lanthanide element-based and correlated material systems.

This chapter will introduce basic concepts of Hall effects and introduce several topological phases related to the studies under this dissertation. The experimental technique utilized for these studies will be introduced in Chapter 2. The results and conclusions of the studies will follow in Chapters 3-6.

## 1.1 Classical Hall effect

As shown in the schematic diagram in Figure 1.1(a), when current is passed along a sample in a perpendicular magnetic field, the electrons entering the sample (considering electrons are carrying current) experience a magnetic Lorentz force, expression in equation 1.1, curving its path inside the sample.

$$\vec{F}_M = (-e)(\vec{v}\times\vec{B}) \tag{1.1}$$

The result is that one transverse end of the sample gets negatively charged with respect to the opposite end creating a potential difference across the transverse direction. This effect is called the *Hall effect* or the *classical Hall effect* - named after Edwin Hall, who first discovered it in 1879 [9] - and the transverse voltage developed in the sample is called the Hall voltage ($V_H$).

Considering velocity of electrons $\vec{v} = (-v_x, 0, 0)$ and magnetic field $\mathbf{B} = (0, 0, -B_z)$, the component of Lorentz force in the transverse direction is:

$$F_M, y = (-e)(-v_x B_z), \tag{1.2}$$

Transverse electric field ($E_y$) developed across the sample produces a force

$$F_E, y = (-e)E_y \tag{1.3}$$

At equilibrium, $|F_E, y| = |F_M, y|$, therefore:

$$eE_y = ev_x B_z \Rightarrow E_y = v_x B_z \tag{1.4}$$

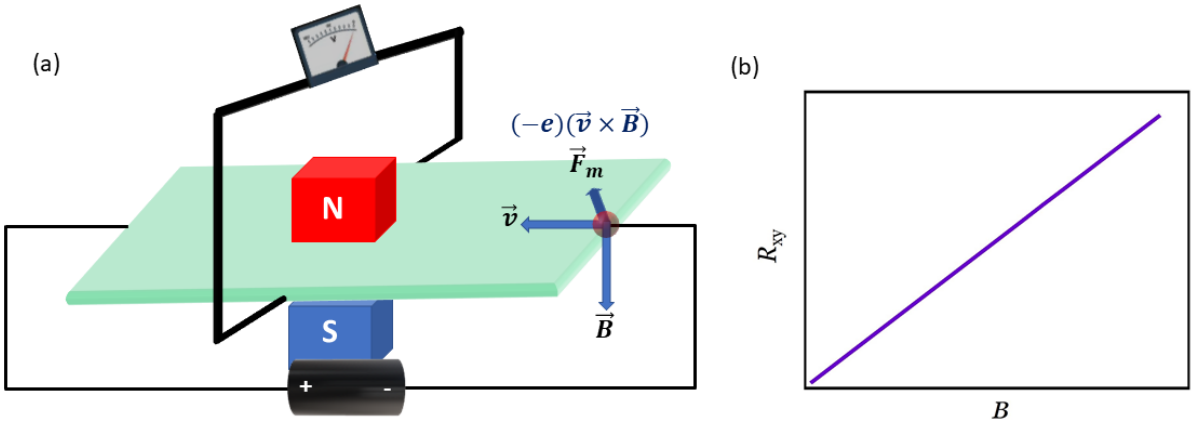


Figure 1.1: Classical Hall effect. (a) Illustration of the classical Hall effect. (b) Hall resistance as a function of magnetic field (for positive charge carriers).

Considering the width of the sample as $w$, the Hall voltage is then

$$V_H = E_y w = v_x B_z w \tag{1.5}$$

The current density ($J_x$) defined as current per unit cross-sectional area is given by

$$J_x = \frac{I_x}{wt} = n(-e)v_x \Rightarrow v_x = \frac{I_x}{n(-e)wt} \tag{1.6}$$

where $t$ is the thickness of the sample and $n$ the electron density. With this, the Hall voltage in equation 1.5 becomes:

$$V_H = \frac{I_x}{n(-e)t}B_z = R_H\frac{I_x B_z}{t}, \tag{1.7}$$

where, $R_H = \frac{1}{n(-e)}$ is the Hall coefficient. The Hall resistance or the transverse resistance ($R_{xy}$) is then:

$$R_{xy} = \frac{V_H}{I_x} = \frac{R_H}{t}B_z \tag{1.8}$$

Therefore, for a given sample of fixed thickness, the Hall or transverse resistance is linear in magnetic field. A graphic relation is shown in figure 1.1(b). Soon after the discovery of Hall effect, Hall himself discovered that even stronger Hall effect can also be achieved in ferromagnetic materials [10] - the effect is commonly known as the *Anomalous Hall effect*. In these ferromagnets, the Hall resistance rises sharply before almost saturating at higher values of the field [11]. More can be found on anomalous Hall effect in Ref. [12].

## 1.2 Integer Quantum Hall effect

The quantum variant of the Hall effect, which was discovered in 1980 by Von Klitzing *et al.* [1], introduced the use of topology in describing the electronic states in solids. A Hall setup of a two-dimensional (2D) electron gas system in sufficiently high magnetic field and low temperatures gives the result that is different from the result in the classical Hall case, where the Hall resistance is linear in magnetic field. In this case, the Hall resistance depicts well defined plateaus at which

$$R_{xy} = \frac{h}{\nu e^2}, \tag{1.9}$$

and the normal/longitudinal resistance ($R_{xx}$) vanishes. The quantization of the Hall conductivity

$$\sigma_{xy} = \nu \frac{e^2}{h}; \quad \nu = 0,\ 1,\ 2, ..... \tag{1.10}$$

is extremely precise and is not altered by the geometry of the system or impurities in the system. TKNN (Thouless, Kohmoto, Nightingale, and den Nijs) [13] later demonstrated the link between this quantization with topology and found that the integer $\nu$ is in fact a topological invariant called the Chern number or TKNN invariant, which distinguishes a quantum Hall (QH) state with a band insulating state. This invariant is obtained from the integration of the Berry curvature over the 2D

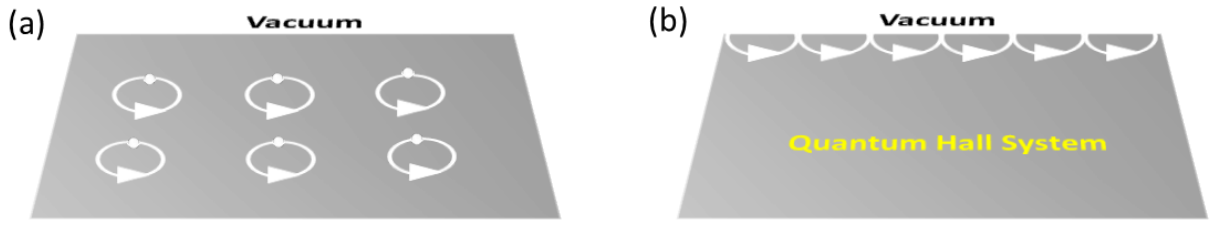


Figure 1.2: Quantum Hall effect. (a) Cyclotron orbits of electrons in a magnetic field. (b) Skipping orbits of electrons at the interface with vacuum leading to edge current.

Brillouin zone (BZ).

$$\nu = \frac{1}{2\pi} \int_{BZ} (\nabla_{\mathbf{k}} \times \mathbf{A})\, d^2\mathbf{k}, \tag{1.11}$$

where $\mathbf{A} = \sum_n < u_n(\mathbf{k}) | i\nabla_{\mathbf{k}} | u_n(\mathbf{k}) >$ is the Berry connection, its curl in the momentum space $\nabla_{\mathbf{k}} \times \mathbf{A}$ is the Berry curvature, $u_n(\mathbf{k})$ defines the electron Bloch state in the $n^{th}$ occupied state, and $\mathbf{k}$ represents the crystal momentum vector.

The QH systems are insulating, but what distinguishes them with the ordinary band insulating systems is this topological invariant. However, if the topological invariant is changing in going from ordinary insulating state to the QH state, then the system can not remain insulating. This is where the presence of the edge states comes into play - the QH state is insulating in its 2D bulk, but differs from the ordinary insulating state due to the conducting edge states at the edges [14].

Under the influence of a perpendicular magnetic field, the electrons tend to move in circles - the cyclotron orbits - as shown in figure 1.2(a). However, if we consider the electrons that are present at the edges as shown in figure 1.2(b), they cannot complete the cyclotron orbit and the electrons are forced to bounce back from the boundary and skip forward thereby creating a unidirectional conducting channel at the edge called the chiral edge mode. The result of this is the presence of extended states connecting the bulk valence and conduction bands in the energy-momentum

dispersion at the edges of a QH system (figure 1.3(a)).

### 1.3 Quantum Spin Hall Effect and 2D topological insulator

One of the key ingredients of QH effect is the perpendicularly applied magnetic field to the direction of current. The necessity of the magnetic field means that the time-reversal (TR) symmetry is broken in QH systems. After the QH effect was discovered and explored, the question that hit the scientific community was whether or not it is possible to obtain the topological states as in the QH effect but in TR invariant systems. This question was answered after the work of Kane and Mele in 2005 [15], in which they proposed that injection of spin-orbit coupling (SOC) would turn graphene - a non-magnetic system - into an insulating system leading to a new topological state, without the need of magnetic field, called the quantum spin Hall (QSH) state. Another work by Bernevig and Zhang in 2006 [16] predicted the generation of the QSH effect in semiconductors with strain gradient with the consideration of SOC. The QSH state may be understood as a combination of Haldane model [17] for spin up and that of spin down in one. A QSH state is insulating and is topologically distinct from an ordinary band insulator, therefore also commonly known as a 2D topological insulator (TI). At the edges, two conducting channels exist, one for each spin, and they propagate in opposite directions resulting into a helical edge mode, which can be visualized as shown in figure 1.3(b) in energy-momentum space. Because they propagate oppositely, the net Hall conductance vanishes, however, a finite spin current can be defined and the corresponding spin Hall conductivity is quantized. The first experimental realization of the QSH state was achieved in the $\mathrm{HgTe}$ quantum well in 2007 [18] following its prediction in 2006 [19].

The non-breaking of the TR symmetry means that the Chern number is zero in a QSH or 2D TI system, however, it is topologically different from the ordinary insulators. That means there should exist another topological index/invariant that distinguishes the QSH with band insulating

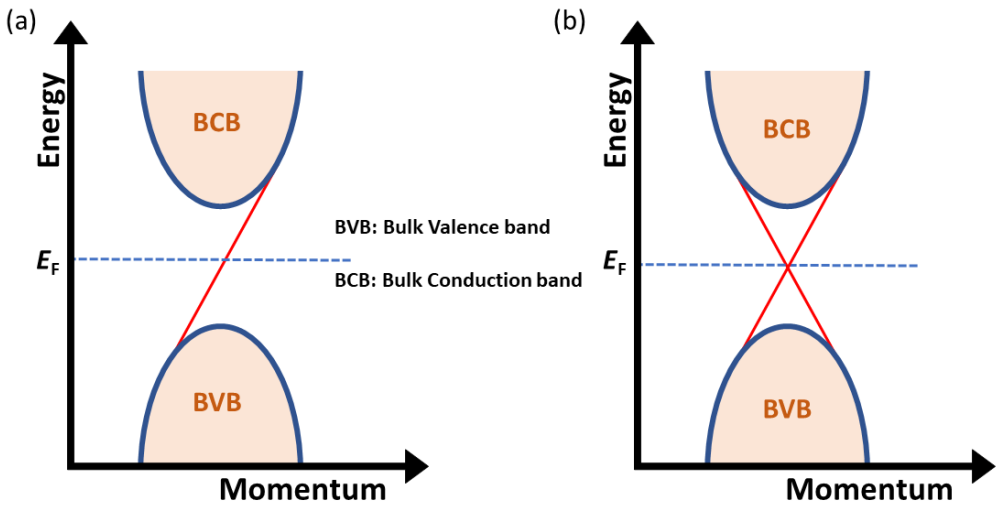


Figure 1.3: Edge dispersion in Quantum Hall and Quantum spin Hall systems. (a) Chiral edge mode in Quantum Hall system. (b) Helical edge state in Quantum spin Hall system.

state. Kane and Mele in 2005 introduced a new topological invariant - the $\mathbb{Z}_2$ topological invariant - that distinguishes the non-trivial QSH insulators from the trivial insulators [20]. While in trivial insulators, it is even ($\nu = 0$), in non-trivial TIs, it is odd ($\nu = 1$). It could also be understood as the number of times (odd or even) the Fermi level crosses the edge states between the TR invariant momentum (TRIM) points in the edge BZ [21]. Because of the SOC, the edge states will be split, however, not at the TRIM points forced by the Kramers' degeneracy requisite [22]. If in between the TRIM points, the Fermi level crosses the edge states an odd number of times, then the edge states would be robust leading to a non-trivial topological insulating phase. In case of even number of crossings, the system would be a trivial insulator.

The $\mathbb{Z}_2$ topological invariant can be obtained from the Fu-Kane model [23] as:

$$(-1)^{\nu} = \prod_{i=1}^{N} \delta_i, \tag{1.12}$$

where $\delta_i$ denotes the parity eigenvalue at the $i^{th}$ TRIM point. Since there are four TRIM points in

2D (considering cubic symmetry), the $\mathbb{Z}_2$ invariant ($\nu$) in 2D is obtained from:

$$(-1)^{\nu} = \prod_{i=1}^{4} \delta_i, \tag{1.13}$$

## 1.4 Three-dimensional topological insulator

The prediction of 2D TI in the $\mathrm{HgTe}$ quantum well [19] and its subsequent realization [18] left the researchers with the question whether or not this topological phase can be seen in higher-dimensions. It was soon realized that it is possible to obtain the topological insulating state in three-dimensional (3D) materials and this state can be characterized by the 3D generalization of the $\mathbb{Z}_2$ topological invariant [21, 23, 24]. Similar to topological conducting channels along the edge of a QSH system, a 3D TI contains topological states on the 2D surface (figure 1.4(a)). In energy-momentum space, the surface states form a conic dispersion, called the Dirac cone, with the crossing point called the Dirac point [3, 4, 25]. A schematic of a Dirac cone is presented in figure 1.4(b). The dispersion is linear near the Dirac point and is given by:

$$E = \pm \hbar v_D |\mathbf{k}| \tag{1.14}$$

and is the eigenvalue of the effective Hamiltonian

$$H = \hbar v_D (k_y \sigma_x - k_x \sigma_y), \tag{1.15}$$

where $v_D$ is the Dirac velocity and $\sigma_i$ $(i = x,\ y)$ represent the Pauli matrices. The spin and momentum are locked at perpendicular direction with each other leading to the helical spin texture in the surface Dirac cone. If a constant energy contour of the Dirac cone is taken, we obtain a circular pocket in $k_x - k_y$ plane that has a spin pointing tangentially at each point.

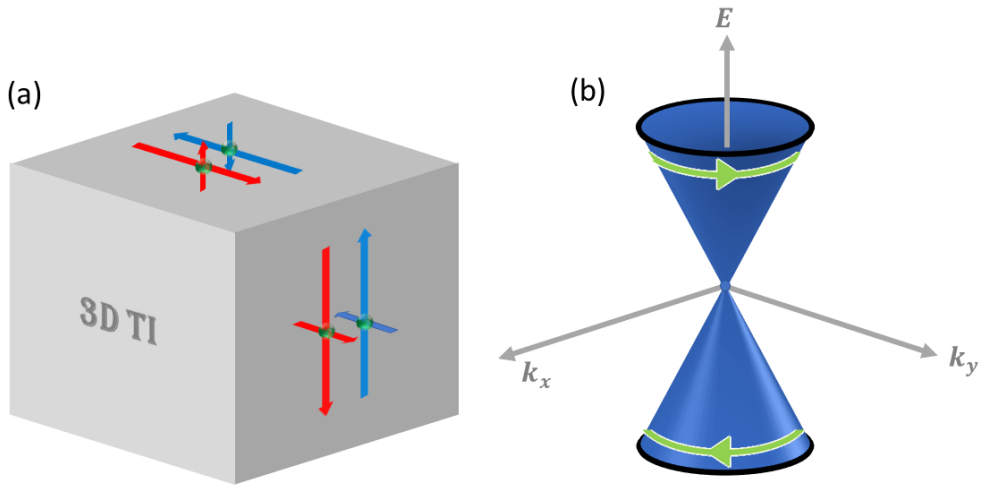


Figure 1.4: Three-dimensional topological insulator. (a) Schematic of 2D surface conduction channels in a 3D topological insulator. (b) Energy-momentum dispersion of the surface state in a 3D topological insulator.

Following the prediction of a 3D TI state in the BiSb alloy [21], the first experimental realization was achieved in 2008 via photoemission measurements [26]. Because of the small bulk band gap and larger number of surface states in this material, the search for materials that are stoichiometric and possess a lesser number of topological surface states went on. As a result of this, the 3D TI family of $(\mathrm{Bi/Sb})_2(\mathrm{Se/Te})_3$ materials was uncovered where the bulk band gap is in the order of 0.3 meV and a single surface Dirac cone resides at the center of the surface BZ (SBZ) [27, 28].

A 3D TI can be weak and strong depending upon the set of four $\mathbb{Z}_2$ topological invariants $(\nu_0; \nu_1\nu_2\nu_3)$, where $\nu_0$ is the strong topological index and is obtained from equation 1.12 as a product of the parity eigenvalues at each of the TRIM points in the 3D BZ [21]. The odd (=1) value of this index defines a strong TI. The other three indices $\nu_1, \nu_2, \nu_3$ are the weak indices and are calculated from the product of parity eigenvalues at the TRIM points that lie in a certain surface [21]. An odd value (=1) of any of these weak indices defines a Weak TI. A trivial insulator has all of the strong and weak indices even (=0). In the case of a strong TI, the Fermi surface encloses an

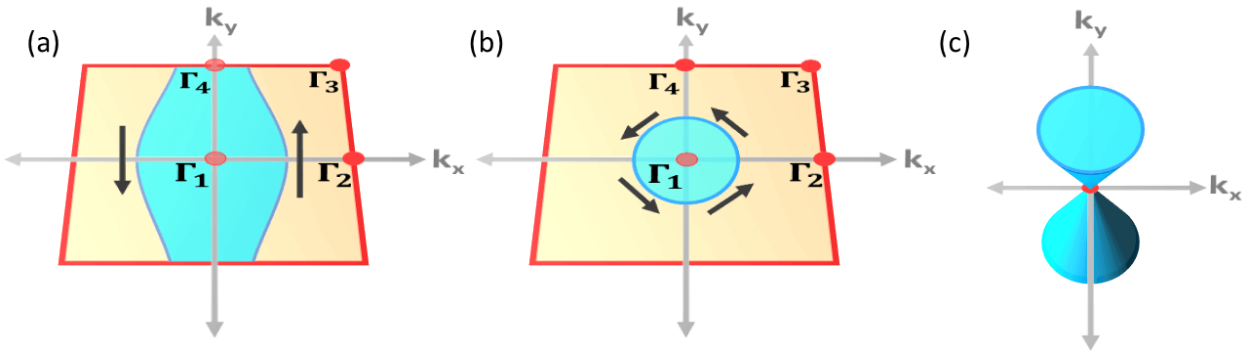


Figure 1.5: Strong and weak topological insulators. (a) Fermi surface of a weak topological insulator. (b) Fermi surface of a strong topological insulator. (c) Single Dirac cone with the Dirac point enclosed by the Fermi surface of a strong topological insulator in (b). This figure is adopted from M. Z. Hasan and C. L. Kane, Rev. Mod. Phys. **82**, 3045 (2010) [3].

odd number of Dirac points, that are strongly protected by the TR symmetry. An schematic of the strong TI is shown in figure 1.5(b), in which the Fermi surface encloses a single Dirac point with Dirac cone dispersion as shown in figure 1.5(c). The 3D TIs discussed above - $\mathrm{BiSb}$ alloy and $(\mathrm{Bi/Sb})_2(\mathrm{Se/Te})_3$ - fall under the strong TI family. A strong TI features topological Dirac surface states on all surfaces. The TR symmetry protected surface Dirac cones in a strong TI can be gapped out by introducing magnetic impurities or intrinsic magnetization leading to massive Dirac fermions [29, 30]. Such magnetic TIs are still interesting as they can host a variety of novel phenomena including the quantum anomalous Hall (QAH) effect and axion insulating phase [31, 32, 33, 34]. A weak TI, on the other hand, encloses an even number of Dirac points on its Fermi surface (figure 1.5(a)). The Dirac states in such TI are not protected by the TR symmetry and can be gapped out easily with perturbations that break the translation symmetry. Topological surface states in these materials are present only on particular surfaces and are absent on other surfaces, which are called topologically dark surfaces [35]. A different class of TI in which the crystal symmetry also plays a vital role in topological protection also exists, and such TI class is called topological crystalline insulators [36, 37, 38]. Such TIs have topological surface states only

on the particular surfaces that respect the protecting symmetry.

## 1.5 Topological semimetal

The experimental discovery of 3D TI prompted an influx of research into finding more material candidates that can host topological phases. In the process, more topological phases beyond TIs got discovered. Topological semimetal (TSM) phase is one of them, in which the bulk valence and conduction bands cross at discrete positions in the momentum space accidentally or enforced by some symmetries [5]. Depending upon the dimensionality, band-degeneracy and symmetry protection, TSMs are generally classified as Dirac semimetals (DSMs) [5, 39, 40, 41], Weyl semimetals (WSMs) [5, 6, 42, 43], and nodal-line semimetals (NLSMs) [7, 44, 45, 46].

A DSM phase is observed in the presence of TR and Inversion symmetries, where both the crossing/touching bands are two-fold degenerate. The bulk Dirac point is, therefore, four-fold degenerate. A schematic of a bulk Dirac cone dispersion in a DSM is presented in figure 1.6(a). When either of the TR or inversion symmetries is broken, then the Dirac fermion splits into a pair of two-fold degenerate Weyl points with opposite chirality that get separated in momentum space giving a realization of a WSM (schematic shown in figure 1.6(b)). In that sense, a Dirac node is a combination of the Weyl node pair. The low-energy band dispersion near the Weyl nodes is governed by the Hamiltonian:

$$\mathcal{H}_{\pm} = \pm v\sigma \cdot \hbar\mathbf{k} = \pm \sum_{i=x,y,z} v\sigma_i \hbar k_i \tag{1.16}$$

where $\pm$ represents the chirality (or the topological charge) of the Weyl node and $v$ is the velocity of the Weyl fermion. The corresponding dispersion is linear and gives a Weyl cone in energy-momentum space.

$$E_{\pm} = \pm v|\hbar\mathbf{k}| \tag{1.17}$$

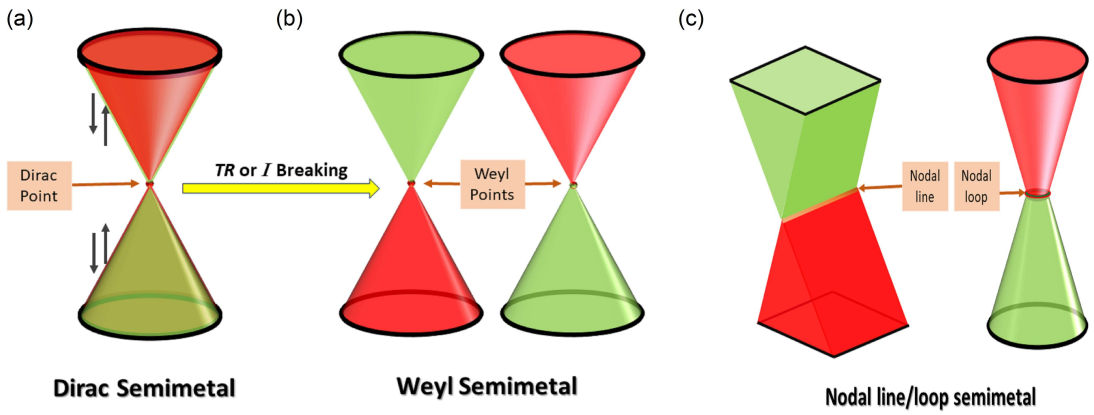


Figure 1.6: Schematic of band crossing in (a) Dirac, (b) Weyl, and (c) nodal-line semimetals.

In a DSM, two Weyl nodes of opposite chirality are coupled together, however the gap opening due to annihilation is prevented by the presence of symmetries. When TR symmetry or inversion symmetry is broken, then they can be separated in momentum space leading to a WSM phase. In TR-invariant non-centrosymmetric case, TR symmetry forces the same chirality at positive and negative momentum positions. Therefore, at least a pair of positive chirality and a pair of negative chirality Weyl nodes (total of minimum four) are present in such WSMs. In TR breaking centrosymmetric case, inversion symmetry allows opposite chirality Weyl nodes at opposite momentum positions, thereby a minimum of two Weyl nodes are possible in such WSMs. The bulk-boundary correspondence ensures the presence of surface states that connect the Weyl nodes of opposite chiral charge [6, 42, 43, 47]. These states are the smoking evidences of Weyl semimetals and are called the Fermi arcs.

Experimental realization of DSM [39, 40, 41] and WSM [42, 43] phases provided the condensed matter physics realization of Dirac or Weyl fermions in high-energy physics as low energy excitations. In these TSMs, if we tune the binding energy position of the Dirac or Weyl nodes at the Fermi level, the resulting Fermi surface would have a point-like pocket. Recent advances in the search of TSMs has introduced new types of Dirac or Weyl semimetals in which the Dirac or

Weyl cone is strongly tilted [48, 49, 50, 51, 52]. A constant energy contour taken at the position of the Weyl or Dirac node in these materials will, therefore, contain both electron and hole pockets and Weyl node exists at the intersection of these pockets. These Weyl or Dirac fermions are called Type-II type and do not have any high-energy physics analogs as they violate the Lorentz invariance. In addition to four-fold Dirac and two-fold Weyl fermions, it is also possible to obtain symmetry protected three-, six-, and eight-fold point degeneracies in condensed matter systems [53, 54, 55, 56, 57, 58, 59].

Different from point degeneracy in the DSM, WSM, and beyond as discussed above, it is also possible to have topological band crossing extended along a line or a loop (schematic shown in figure 1.6(c)), which is the case of NLSM [7, 44, 45, 46, 60, 61] (also referred to as nodal-loop or nodal-ring semimetals). The bulk boundary correspondence in NLSM lies in the occurrence of the drumhead-like surface states [62, 63, 64]. These surface states are almost flat and such flat-type band dispersion could lead to exotic phenomenon such as high-temperature surface superconductivity [65, 66]. A NLSM can be a Dirac-type or a Weyl-type based on the presence of symmetries [61]. A Dirac-type NLSM is realized in TR-invariant centrosymmetric materials with negligible SOC. In presence of strong SOC, gap opening may occur leading to a TI phase [67] or in presence of some crystalline symmetry, a nodal line may split into Dirac nodes leading to a DSM phase [68]. Weyl-type NLSM, on the other hand, is realized when one of TR or inversion symmetry broken and additional crystalline symmetry such as mirror symmetry is required to protect the nodal line [44, 61]. Inclusion of SOC can open up a gap, however, the presence of mirror symmetry may lead to pairs of Weyl nodes mapped by the mirror plane [69, 70]. Moreover, non-symmorphic symmetries, glide mirror or screw rotation, also can generate NLSM [45, 46, 71], in which SOC does not play a significant role because of lattice translation protection [72].

## 1.6 Higher-order topological Insulator

The 3D topological phases we have discussed so far have topological states either in 3D bulk or 2D surface protected by the non-trivial topology of the bulk. New topological phases, where topological states lie in lower dimensional region i.e., one-dimensional (1D) hinges or zero-dimensional corners, have also been discovered and these phases are known as higher-order topological phases [73, 74]. The order is defined by the dimension of the region where the topological edge states reside - if the edge states are present in $d - n$ dimensional region ($d$ being the dimensionality of the system), the topological phase would be of $n^{th}$ order. By this definition, the topological phases discussed in previous sections would fall under first order topological phases. For example, a 3D TI features topological states on the $3 - 1$ dimensional surfaces, therefore, it is a first-order 3D TI. A TI of higher order - called higher order TI (HOTI) - features the topological states in $3 - 2$ or lower dimensional region [75].

Just like a 3D TI, a HOTI in 3D has an insulating bulk. While the 2D surface of a 3D TI contains metallic states that are topologically protected, the surface of a 3D HOTI is gapped out and the metallic states lie along the hinges or at the corners. A HOTI can have a unidirectional hinge mode, analogous to the edge states in a QH system, or a pair of counter-propagating hinge modes, analogous to the edge states in a QSH system [75]. Schematics of second-order 3D TIs with helical hinge states are presented in figure 1.7. Crystalline symmetries play a role in preserving the topology in these novel topological systems [75, 76, 77, 78, 79]. HOTI phase has been experimentally realized in electronic circuits [80], photonic and phononic systems [81, 82] as well as in crystalline systems such as Bismuth [83]. The notion of higher-order topology has been extended to higher-order topological superconductors [76, 78, 79], higher-order Dirac and Weyl semimetals [84, 85, 86] and more [87, 88, 89].

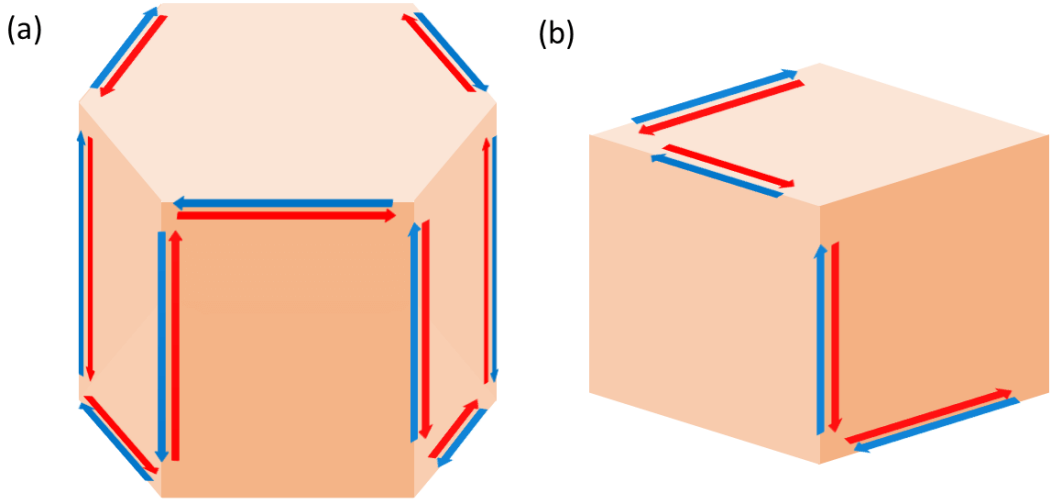


Figure 1.7: Higher order topological insulator. (a) Schematic of hinge states in a hexagonal higher order topological insulator adopted from F. Schindler *et al.*, Nat. Phys. **14**, 918 (2018) [83]. (b) Schematic of reflection-symmetric second order topological insulator adopted from J. Langbehn *et al.*, Phys. Rev. Lett. **119**, 246401 (2017) [76].

### 1.7 Kagome and breathing kagome geometry

A good chunk of researches in the recent years have focused on the interplay among different physical parameters such as geometry, topology, correlation, magnetic ordering, etc. Materials with kagome geometry have come into play as rich grounds in order to study all or some of these parameters. Conventional kagome geometry comprises of six-equivalent triangles which share the corners forming a hexagon with their bases (see Figure 1.8(a)). Flat bands due to geometry forced electronic state localization gives rise to correlation effects, and possible presence of Dirac crossing at the corner of the BZ is indicative of the potential topology [90, 91, 92, 93, 94, 95]. A Chern phase can be induced by opening a gap at the Dirac crossing by introducing SOC and ferromagnetic ordering [96, 97]. Different from the conventional geometry of six equivalent triangles, some kagome systems possess alternating triangles of two different sizes in a so called breathing kagome geometry [98, 99] (See schematic in Figure 1.8(b)). Though the Dirac crossing at the corner of the

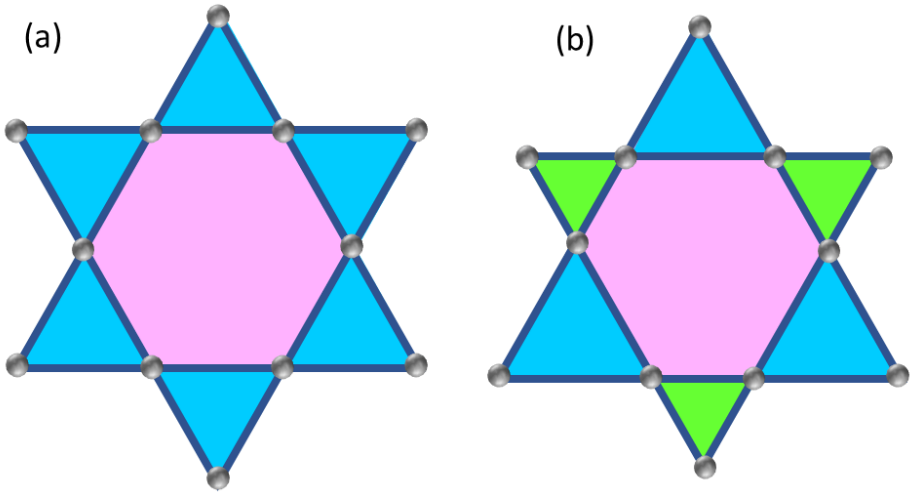


Figure 1.8: Schematic of (a) conventional kagome lattice and (b) breathing kagome lattice.

BZ may be gapped, these breathing kagome systems have the potential of featuring higher-order topological phase along with robust topological flat bands [98, 100, 101].

## 1.8 Charge density wave

Charge density wave (CDW) is a periodic fluctuation of the charge carrier density caused by the periodic lattice deformation [102, 103, 104]. Owing to its relevance in understanding of several properties of solids such as electron-phonon interaction and structural transitions as well as its occurrence with other co-existing or competing exotic phenomena such as superconductivity and magnetism, CDW has remained an important topic of study over the decades [105, 106, 107, 108, 109, 110, 111, 112, 113, 114, 115].

The simplest example of CDW can be picturized in one-dimension via Peierl's distortion [116, 117]. Lattice periodicity ($a$) doubles with electronic disturbance of the system by a wave vector ($q$) twice the Fermi wave vector ($2k_f$). This results in halving of the BZ with boundaries at

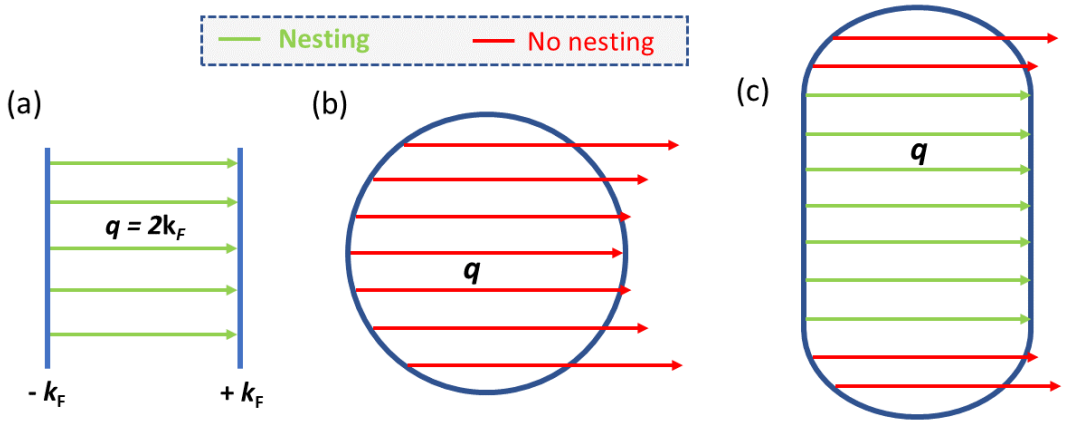


Figure 1.9: Schematic of Fermi surface nesting. (a) Perfect Fermi surface nesting in one dimension by a wave vector equal to twice the Fermi wave vector. (b) Absence of nesting in a 2D circular Fermi surface. (c) An example of partial nesting in 2D. The figure is adopted from P. Aebi *et al.*, J. Electron Spectros. Retal. Phenomena **117-118**, 433 (2001) [120].

$k = \pm\frac{\pi}{2a}$. The wave vector $q$ nests the BZ boundaries on the FS, creating a gap. This process is commonly known as FS nesting. The nesting of the FS is perfect in one dimension, but in moving to higher dimensions, the nesting becomes imperfect or absent (see schematic in Figure 1.9). Imperfect nesting leads to gapping of only a portion of the FS, leaving the system metallic even with CDW ordering [118, 119, 120]. Other than FS nesting, CDW is generally associated with other mechanisms such as electron-phonon coupling and exciton condensation [121].

# CHAPTER 2: EXPERIMENTAL TECHNIQUES

The main experimental technique used for the works included in this dissertation is angle-resolved photoemission spectroscopy (ARPES). In addition to the lab-based ARPES set up at the University of Central Florida, the results presented in this dissertation were obtained using the synchrotron-based ARPES set ups at the Advanced Light Source (ALS) beamlines 10.0.1.1, 10.0.1.2 & 4.0.3.2, Stanford Synchrotron Radiation Lightsource (SSRL) beamline 5-2, and Swiss Light Source (SLS) SIS-ULTRA beamline. This chapter will introduce the concepts related to state-of-the-art ARPES technique.

## 2.1 Angle-resolved photoemission spectroscopy

The study of electronic structure of solids is important as it governs several exotic properties associated with them. ARPES is a powerful experimental tool that can directly probe the electronic structure in solids [122, 123, 124, 125, 126, 127, 128, 129, 130, 131]. An schematic of ARPES experimental set up is presented in Figure 2.1. It is a *photon in electron out* process that bases on the principle of photoelectric effect - current generation with illumination of light. First observed by Hertz in 1887 [132] followed by Hallwachs in 1888 [133] and Lenard in 1900 [134], it was only explained by A. Einstein in 1906 [135], which won him a Nobel prize in 1921. As proposed by Einstein, light is quantized with a quantum of light called the photon with energy $h\nu$, $h$ being the Planck's constant and $\nu$ the frequency.

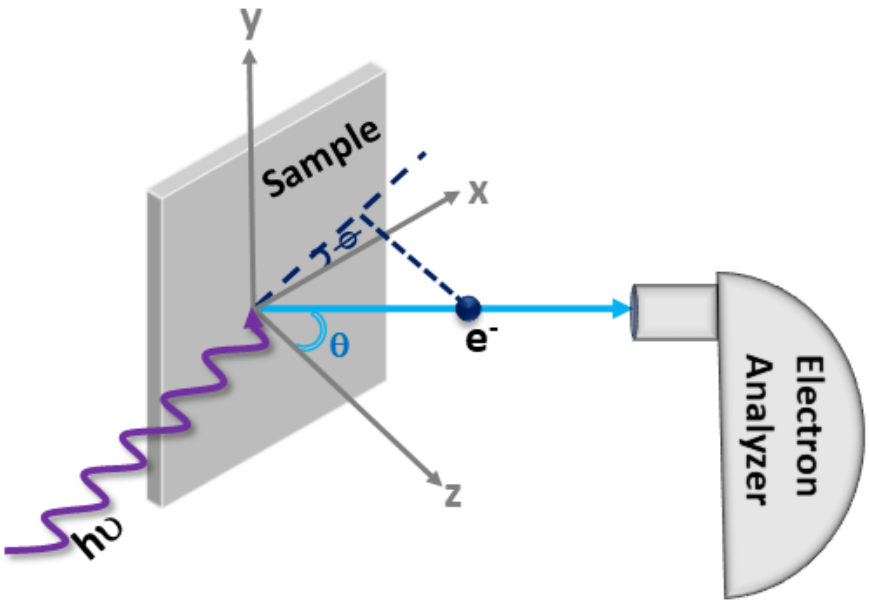


Figure 2.1: Schematic of ARPES experimental setup.

### *2.1.1 Photoemission kinetics*

Photoemission process refers to the process of ejection of electron when light with sufficient energy is shone on the surface of a sample. The kinetics of the photoemission process is presented in Figure 2.2. When the electron is ejected from the surface, the kinetic energy ($E_{\mathrm{K}}$) of the ejected electron, called the photoelectron, is related to the energy of the incident light as:

$$E_{\mathrm{K}} = h\nu - \Phi, \tag{2.1}$$

where, $\Phi$ is the inherent property specific to a material, called the work function, defined as the minimum energy required to eject an electron from the surface of the sample to the vacuum. In order to dislodge the electron from the core of the sample, the incident photon energy should overcome the binding energy ($E_{\mathrm{B}}$) of the electron in addition to the work function. The kinetic

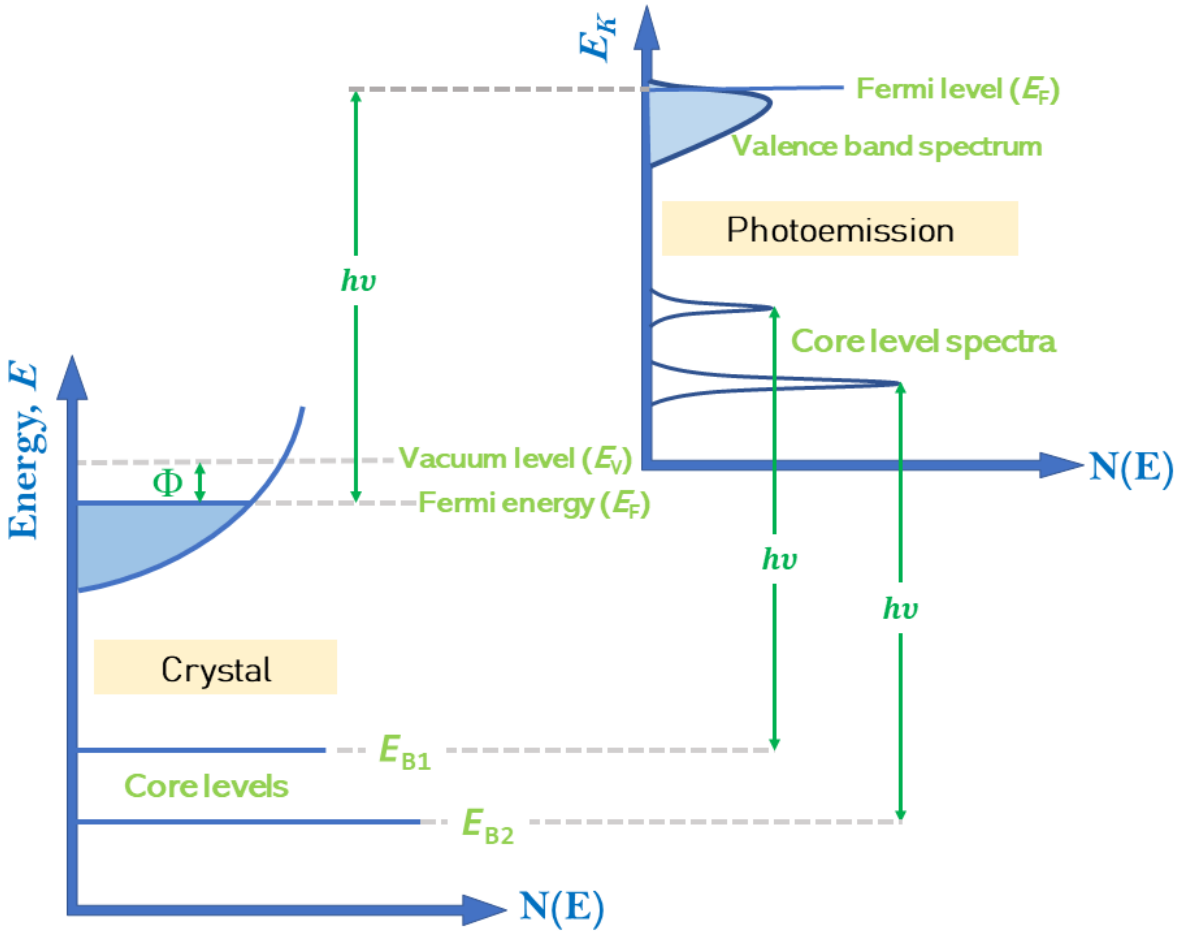


Figure 2.2: Energy levels inside crystal and in photoelectron spectrum. This figure is adopted from S. Hüfner, *Photoelectron Spectroscopy: Principles and Applications* (Springer, 1995) [124].

energy of the ejected electron is then defined as:

$$E_{\mathrm{K}} = h\nu - \Phi - \mid E_{\mathrm{B}} \mid \tag{2.2}$$

The momentum of the photoelectron ($K$ in wave vector units) is defined by;

$$K = \frac{1}{\hbar}\sqrt{2mE_{\mathrm{K}}} \tag{2.3}$$

The momentum vector is the sum of parallel and perpendicular components.

$$\vec{K} = \vec{K}_{\parallel} + \vec{K}_{\perp} \tag{2.4}$$

The magnitude of the parallel and perpendicular components depend on the emission angle $\theta$ (see Figure 2.1) as;

$$K_{\parallel} = \frac{1}{\hbar}\sqrt{2mE_{\mathrm{K}}}\,\sin\theta \tag{2.5}$$

and

$$K_{\perp} = \frac{1}{\hbar}\sqrt{2mE_{\mathrm{K}}}\,\cos\theta \tag{2.6}$$

When the photoelectron is ejected out to the vacuum, the translation symmetry remains conserved parallel to the sample surface, however, it is broken along the direction perpendicular to the sample. Assuming the momentum of the photon is negligible compared to that of the electron, the conservation of momentum implies that the parallel component of the momentum does not change during the photoemission process. The parallel component of the momentum of electron inside the crystal ($k_{\parallel}$) is, therefore:

$$k_{\parallel} = K_{\parallel} = \frac{1}{\hbar}\sqrt{2mE_{\mathrm{K}}}\,\sin\theta \tag{2.7}$$

Assuming the sample surface to be along the $xy$-plane, the $x$ and $y$ components of the parallel momentum are defined by the emission angle $\phi$ (see Figure 2.1) as:

$$k_x = \frac{1}{\hbar}\sqrt{2mE_{\mathrm{K}}}\,\sin\theta\,\cos\phi \tag{2.8}$$

and

$$k_y = \frac{1}{\hbar}\sqrt{2mE_{\mathrm{K}}}\,\sin\theta\,\sin\phi \tag{2.9}$$

### *2.1.2 Three step model and photoemission spectral function*

The photoemission process is most commonly described by the so called *three step model*. A schematic of the three step model is presented in Figure 2.3. Within this model, the photoemission process has three discrete steps:

- Excitaion of the electrons in the bulk of the sample by the incident light
- Propagation of the photoexcited electron from the bulk to the surface of the sample
- Emission of the electrons from the surface of the sample to the vacuum

In the first step, the photon of energy $h\nu$ incident on the system optically excites the electron inside the sample. Considering the system as a $N$ electron system, the transition probability from initial state $\psi_i^N$ to the photoexcited state $\psi_f^N$ is (as described by the Fermi Golden approximation):

$$w_{fi} = \frac{2\pi}{\hbar} |\langle \psi_f^N \mid \mathcal{H} \mid \psi_i^N \rangle|^2 \, \delta(E_f^N - E_i^N - h\nu), \tag{2.10}$$

where $E_f^N$ and $E_i^N$ are the final and initial state energies of the $N$ electron system. The final state energy is the sum of the kinetic energy gained by the photoexcited electron and the energy of the remaining $N-1$ electron system, i.e. $E_f^N = E_{\mathrm{K}} + E_f^{N-1}$. Similarly, the initial state energy is equal to the energy of the remaining $N-1$ electron system minus the binding energy of the electron before being excited, i.e. $E_i^N = E_i^{N-1} - E_{\mathrm{B}}$. $\mathcal{H}$ in equation 2.10 is the interaction Hamiltonian defined by:

$$\mathcal{H} = \frac{e}{2mc} \left( \vec{p} \cdot \vec{A} + \vec{A} \cdot \vec{p} \right) = \frac{e}{mc} \vec{A} \cdot \vec{p}, \tag{2.11}$$

where $\vec{p} = i\hbar\nabla$ is the momentum operator and $\vec{A}$ is the vector potential of the electromagnetic field of light. Assuming the *sudden approximation* (no interaction between post-excitation photo-

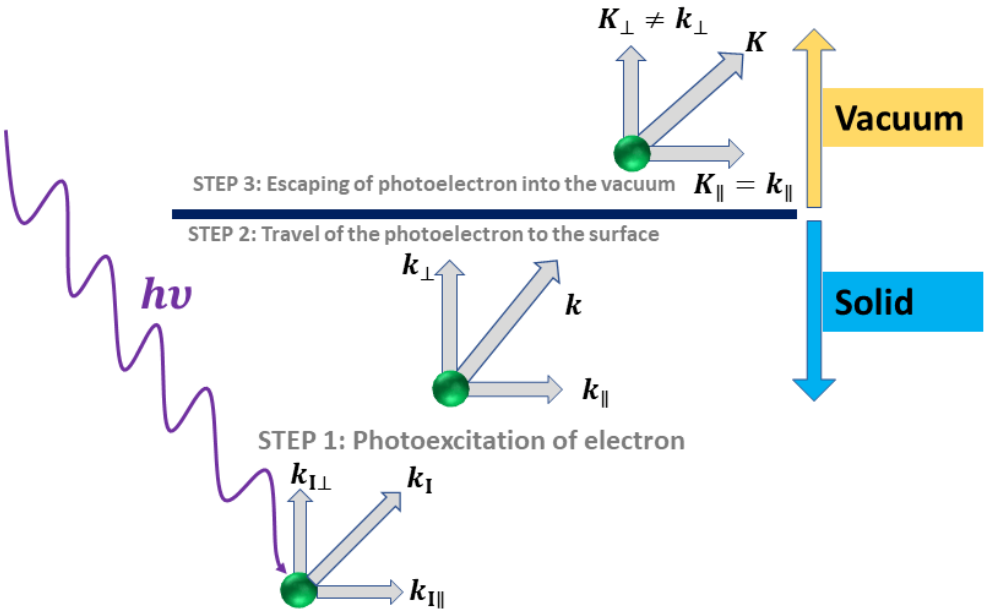


Figure 2.3: Schematic of three-step model of photoemission. This figure is adopted from S. Suga, A. Sekiyama, and C. Tusche, *Photoelectrom Spectroscopy*, (Springer, 2021) [131].

electron and the remaining $N-1$ electron system),

$$\psi_f^N = \mathcal{A}\varphi_f^k \psi_f^{N-1}, \tag{2.12}$$

where $\mathcal{A}$ is an antisymmetric operator, $\varphi_f^k$ is the final state wavefunction of the photoexcited electron with momentum $k$, and $\psi_f^{N-1}$ is the final state wavefunction of the remaining $N-1$ electron system. Under the Hartree-Fock approximation,

$$\psi_i^N = \mathcal{A}\varphi_i^k \psi_i^{N-1}, \tag{2.13}$$

where $\varphi_i^k$ defines the initial state of the electron (before being photoexcited) at some momentum $k$ and $\psi_i^{N-1}$ defines the initial state of the remaining $N-1$ electron system. With the considerations

of sudden approximation and Hartree-Fock approximations, the equation 2.10 becomes:

$$w_{fi} = \frac{2\pi}{\hbar}|\langle\varphi_f^k \mid \mathcal{H} \mid \varphi_i^k\rangle|^2 \, |\langle\psi_m^{N-1}|\psi_i^{N-1}\rangle|^2 \, \delta(E_{\mathrm{K}} + E_m^{N-1} - E_i^N - h\nu) \tag{2.14}$$

Here, $\psi_m^{N-1}$ is the wavefunction of the excited state of the remaining $N-1$ electron system. Assumption of sudden approximation means $\psi_m^{N-1} = \psi_i^{N-1}$. The photoemission intensity for photoelectrons with momentum $k$ and kinetic energy $E_{\mathrm{K}}$ is the sum over all final states, i.e.

$$I(k, E_{\mathrm{K}}) = \sum f, iw_{fi} = \frac{2\pi}{\hbar} \sum_{f,i} |\langle\varphi_f^k \mid \mathcal{H} \mid \varphi_i^k\rangle|^2 \; \sum_m |\langle\psi_m^{N-1}|\psi_i^{N-1}\rangle|^2 \, \delta(E_{\mathrm{K}} + E_m^{N-1} - E_i^N - h\nu) \tag{2.15}$$

The first term $\sum_{f,i}|\langle\varphi_f^k \mid \mathcal{H} \mid \varphi_i^k\rangle|^2 = \sum_{f,i}|M_{f,i}^k|^2$, where

$$M_{f,i}^k = \langle\varphi_f^k \mid \mathcal{H} \mid \varphi_i^k\rangle \tag{2.16}$$

is the one-electron matrix element that contains all information associated with the interaction between the photon and the electron. The term $|\langle\psi_m^{N-1}|\psi_i^{N-1}\rangle|^2 = 1$ for non-interacting systems. However, for correlated systems, $|\langle\psi_m^{N-1}|\psi_i^{N-1}\rangle|^2 \neq 1$. In order to understand the propagation of electrons in such systems, Green's function formalism is used. The one-electron spectral function in this formalism is given by the imaginary part of the Green's function as:

$$A(k, \omega) = -\frac{1}{\pi} ImG(k, \omega) \tag{2.17}$$

The information about the electron propagating in the many-electron system is given by the self-energy $\Sigma(k, \omega) = \Sigma'(k, \omega) + \mathrm{i}\Sigma''(k, \omega)$; $\Sigma'(k, \omega)$ and $\Sigma''(k, \omega)$ being the real and imaginary parts, respectively. With self-energy, the Green's function can be written as:

$$G(k, \omega) = \frac{1}{\omega - \epsilon_k - \Sigma(k, \omega)} = \frac{1}{(\omega - \epsilon_k - \Sigma'(k, \omega)) - \mathrm{i}\Sigma''(k, \omega)} \tag{2.18}$$

The imaginary part of the Green function is, therefore: $ImG(k,\omega) = \frac{\Sigma''(k,\omega)}{(\omega-\epsilon_k-\Sigma'(k,\omega))^2+(\Sigma''(k,\omega))^2}$

The one-electron spectral function becomes:

$$A(k,\omega) = -\frac{1}{\pi}\frac{\Sigma''(k,\omega)}{(\omega-\epsilon_k-\Sigma'(k,\omega))^2+(\Sigma''(k,\omega))^2} \tag{2.19}$$

The photoemission intensity obtained in ARPES is given by:

$$I(k,\omega) = I_0(k,\nu,A)\ f(\omega)\ A(k,\omega) \tag{2.20}$$

The first term in equation 2.20 - $I_0(k,\nu,A)$ is proportional to the one-electron matrix element $M^k_{f,i}$ (equation 2.16). The second term $f(\omega)$ is the Fermi-Dirac distribution function given by:

$$f(\omega) = \frac{1}{1+e^{w/k_BT}} \tag{2.21}$$

$f(\omega)$ is 1 for the occupied states ($\leq$ Fermi energy ($E_{\mathrm{F}}$)) and zero for unoccupied states ($> E_{\mathrm{F}}$). Therefore, ARPES can only probe the electronic structure upto the Fermi level.

### *2.1.3 Matrix elements and polarization dependence*

The term $I_0(k,\nu,A)$ on the photoemission intensity in equation 2.20 is proportional to the one-electron matrix element $M^k_{f,i}$. From equation 2.16, $M^k_{f,i} = \left\langle \varphi^k_f \mid \mathcal{H} \mid \varphi^k_i \right\rangle$ and from equation 2.11, $\mathcal{H} = \frac{e}{mc}\vec{A}\cdot\vec{p}$. Therefore,

$$M^k_{f,i} \sim \left\langle \varphi^k_f \mid \vec{A}\cdot\vec{p} \mid \varphi^k_i \right\rangle \tag{2.22}$$

The vector potential term $\vec{A}$ has dependence on the polarization and energy of the photon source. Therefore, variation in the energy and polarization of the light, which is dependent on the geometry

of the experimental set up, causes photoemission intensity to be modified. This effect is called the matrix element effect. The final one-electron wavefunction $\varphi_f^k$ can be approximated as an even-parity plane wave with respect to a mirror plane defined by the normal to the sample surface and the slit of the electron analyzer. This means, the parity of the operator $\vec{A} \cdot \vec{p}$ and the initial one-electron wave function $\varphi_i^k$ must be either both even or both odd. If they have opposite parity, then the one-electron matrix element term and hence the photoemission intensity will vanish. When the parity of the operator $\vec{A} \cdot \vec{p}$ is even, which is the case of p-polarized light (the field direction of the light is parallel to the mirror plane), only the even parity $\varphi_i^k$'s will produce non-zero matrix elements leading to the finite photoemission intensity. On the other hand, when the parity of the operator $\vec{A} \cdot \vec{p}$ is odd, which is the case of s-polarized light (the field direction of the light is perpendicular to the mirror plane), only the odd parity $\varphi_i^k$'s will produce non-zero matrix elements leading to the finite photoemission intensity.

### *2.1.4 Probing depth and surface/bulk sensitivity*

Within the three step model, the photoexcitation of electron by light is followed by the travel of the photoexcited electron to the surface of the sample. The probability of the photoelectron reaching the surface is proportional to its inelastic mean free path, a measure of average distance the photoelectron can transverse before interacting inelastically. Higher the mean free path, greater the probing depth of the photoemission spectroscopy measurement. The relation between the mean free path and the kinetic energy of the photoelectron is graphically presented in Ref. [124] in a so called *universal curve* of the mean free path (see Figure 2.4). Within 20-100 eV kinetic energies, typical for most ARPES experiments, the mean free path is less than 1 nm, which means only the topmost layer(s) of the atoms in the sample is (are) being probed. This highlights the importance of atomically clean surface for ARPES measurements. In order to increase the bulk-sensitivity of measurements, there are two ways: (i) to use a lower photon energy using ultra-violet laser source

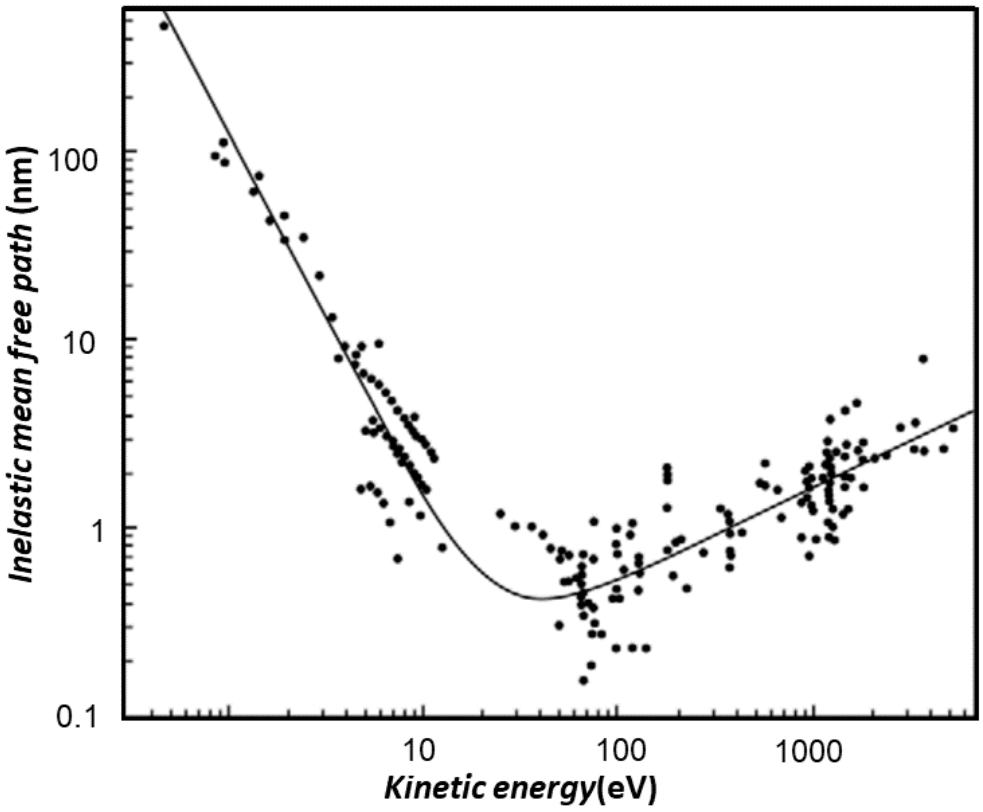


Figure 2.4: Universal curve for electron inelastic mean free path as a function of kinetic energy from Ref. [124].

and (ii) to use high photon energy using soft X-ray source.

### *2.1.5 Determination of $k_z$ and photon energy-dependence*

Because of the breaking of the translation symmetry in the perpendicular direction, the principle of conservation is not applicable for the perpendicular component of the momentum, i.e. $k_\perp$ (or $k_z$) $\neq$ $K_\perp$. In order to determine the perpendicular component of the momentum inside the sample, free-electron approximation is utilized, where the photoelectron is considered as a free electron in a surface potential barrier of height $V_0$. Under this approximations, the kinetic

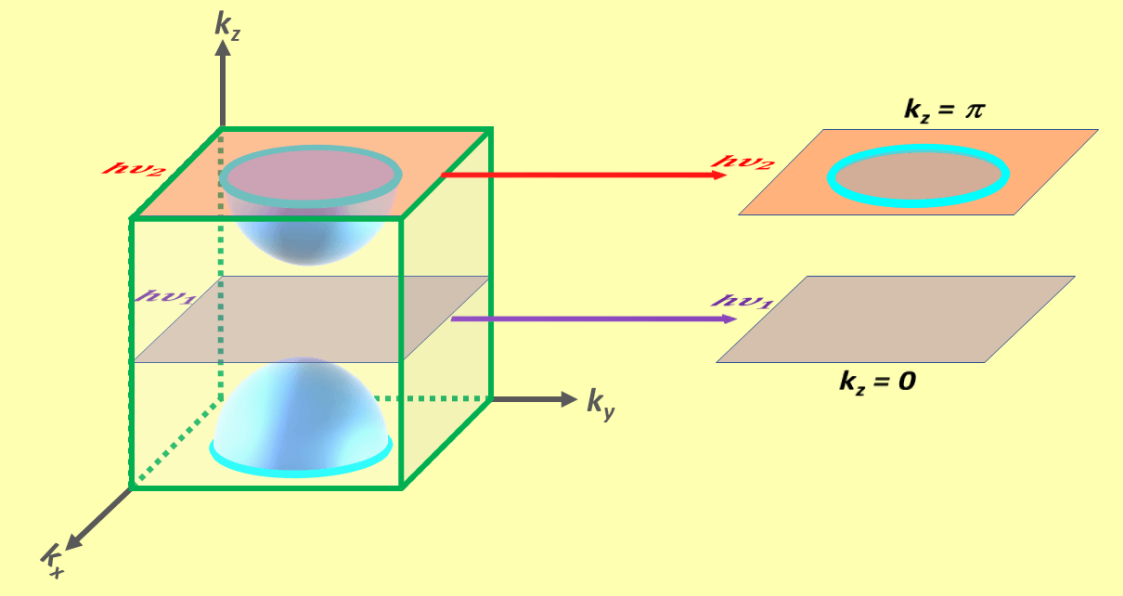


Figure 2.5: Schematic of Photon energy dependent ARPES measurement, where different photon energies can probe different out of plane momentum planes.

energy of the photoelectron can be written as:

$$E_{\mathrm{K}} = \frac{\hbar^2 \left(k_{\parallel}^2 + k_{\perp}^2\right)}{2m} - V_0 \tag{2.23}$$

Thus,

$$k_{\perp}^2 = \frac{2m}{\hbar^2}(E_{\mathrm{K}} + V_0) - k_{\parallel}^2 = \frac{2m}{\hbar^2}(E_{\mathrm{K}} + V_0) - \frac{2m}{\hbar^2}E_{\mathrm{K}}\sin^2\theta = \frac{2m}{\hbar^2}[E_{\mathrm{K}}(1 - \sin^2\theta) + V_0]$$

$$\Rightarrow k_{\perp} = k_z = \frac{1}{\hbar}\sqrt{2m(E_{\mathrm{K}}\cos^2\theta + V_0)} \tag{2.24}$$

The surface potential $V_0$ is also called the *inner potential* and is adjusted to obtain the periodicity along the $k_z$ direction. Since $E_{\mathrm{K}} = h\nu - \Phi - |E_{\mathrm{B}}|$, the equation 2.24 implies that $k_z$ is dependent on the photon energy $h\nu$. Therefore, in photoemission experiment, different photon energies probe different $k_z$ planes in the BZ as depicted in the schematic in Figure 2.5.

## 2.2 Components of ARPES experimental set up

As discussed in the previous section, ARPES uses the basic principle of photoemission, where the incident light ejects electrons from the sample. Therefore, light source is the first and foremost component of an experimental ARPES setup. The ejected electrons are then collected by the ARPES analyzer which collects the information of the kinetic energy and emission angles of the electrons. The need for atomically clean surface of the sample makes ultra-high vacuum (UHV) very very essential in ARPES. Another important component of the ARPES set up is the sample manipulator, which allows different transnational and rotational motion of the sample holder.

### *2.2.1 Light source*

The light sources used in ARPES experiments are either *lab-based*, which include gas discharge lamp and laser, or *synchrotron radiation-based*, which include vacuum ultra-violet (VUV), soft X-ray, and hard X-ray photon sources.

One advantage of lab-based light sources lies in their availability all the time without having to apply for the beamtime. A common gas discharge lamp is the Helium excitation lamp, which can give a very good energy resolution below $2\,\mathrm{meV}$. However, the photon flux is low and the beam spot is large. Also, the continuous flow of Helium gap may cause the sample surface aging sooner. The use of laser in lab-based ARPES systems gives the advantage of increased probe depth. However, the lab-based light sources come with two main disadvantages - inability of tuning photon energy and a large beam spot size. A point to note is that some modern laser-based systems are capable of tuning photon energy, however, only within a small range. Our home-ARPES setup at the Laboratory for Advanced Spectroscopic Characterization of Quantum Materials (LASCQM) has a Scienta Omicron Helium excitation lamp as well as a laser source. The Helium lamp can

generate two discrete photon energy sources - $21.2\ \mathrm{eV}$ $(\mathrm{He\ I}\alpha)$ and $40.8\ \mathrm{eV}$ $(\mathrm{He\ II}\alpha)$. The laser-based source generates $21.4\ \mathrm{eV}$ photon energy pulses by driving high-harmonic generation (HHG) of second harmonics of the laser pulses coming from the commercial $\mathrm{Yb:KGW}$ amplifier [136] (will be discussed in detail in section 2.6).

The aforementioned disadvantages of tunability of photon energy and spot size in lab-based light sources are overcomed in synchrotron radiation-based beamline sources, with added advantage of polarization tunability. However, they are very costly compared to the lab-based light systems and hence are only available at limited user facilities. This creates another disadvantage of having to apply for beamtime in order to perform experiments. Synchrotron sources use the principle similar to Bremsstrahlung radiation, in which a charge particle accelerated by an electric field loses its energy in form of electromagnetic radiation. In case of the synchrotron radiation, the charge particle (electron) is accelerated by a magnetic field resulting in emission of electromagnetic radiation over a wide range of photon energies. Photon energy can then be fixed to a desired value by monochromatizing by a grating monochromator. Highly polarized photon energies ranging from VUV to X-ray region can be generated, thereby providing opportunities for probing different penetration depths and hence for surface as well as bulk sensitive measurements.

### *2.2.2 Electron analyzer*

Once the light source of sufficient energy greater than the work function of the sample (plus the binding energy in case of lower lying electrons) hits the sample, electrons are emitted from the sample surface. These photoelectrons are gathered by the analyzer and the information about the emission angles and kinetic energies of the photon electrons are generated, which are related to the electron momenta and binding energies inside the sample. Most commonly, modern ARPES systems employ a hemispherical electron analyzer [137]. A schematic of a hemispherical electron

analyzer is presented in Figure 2.6. The photoelectrons emitted by the light source are focused into the entrance slit by an electron lens on the basis of the emission angles, which are related to the momenta of the electron. After passing through the entrance slit, the photoelectrons enter into the hemispherical deflector which consists of two concentric hemispheres maintained at a constant potential difference ($V$). The photoelectrons are grouped based on their kinetic energies. One important parameter is the *pass energy*, which is defined to be the energy of the photoelectrons whose motion will be concentric to the hemispheres. The pass energy can be adjusted by altering the potential difference between the hemispheres, the relation is:

$$E_{\mathrm{p}} = eV\left(\frac{R_1}{R_2} - \frac{R_2}{R_1}\right), \tag{2.25}$$

where, $E_{\mathrm{p}}$ is the pass energy and $R_1$ & $R_2$ are the radii of curvature of the outer & inner hemispheres, respectively. The photoelectrons will have different curvatures of motion depending on whether their kinetic energy is larger or smaller than the pass energy. The photoelectrons, already grouped according to their kinetic energy and momenta, hit the detector equipped with a multichannel plate followed by a phosphorous plate and a charge coupled device camera, giving a energy versus momentum picture.

### *2.2.3 Sample manipulator*

Most of the ARPES beamlines have different pre-defined positions for sample loading, transferring, cleaving, and measuring. The sample manipulator is used to move the sample to any of the desired positions. A sample manipulator typically has motion in 6-degrees of freedom. Three of them are translation motion along $x-$, $y-$, and $z-$axes, and the other three are rotational motions. During measurements, the path of the light beam is fixed. In most of the beamlines (including ALS BL 10.0.1.2, ALS BL 4.0.3.2, SSRL BL 5-2, and SIS-ULTRA endstation), the analyzer is kept

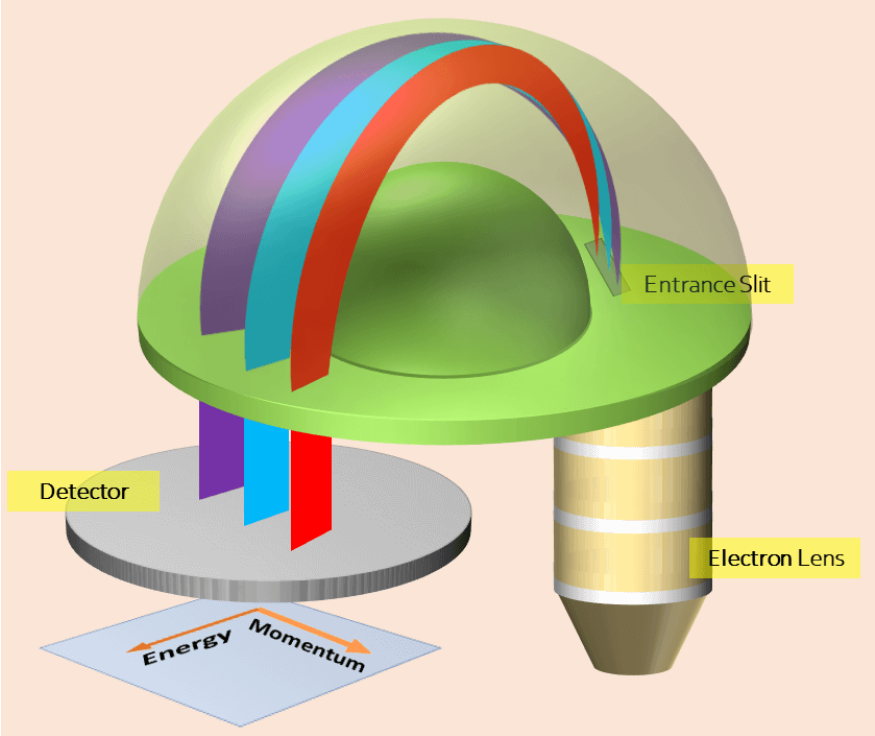


Figure 2.6: Schematic of a hemispherical electron analyzer.

fixed and the detector configuration is changed by moving the sample stage. In ALS BL 10.0.1.1, the sample stage is kept at a fixed measurement position and the analyzer is rotated to acquire the data. Also, in some beamlines that use DA30 analyzer, they require no physical movement of the sample or analyzer during the data acquisition process. The role of sample manipulator is very important in identifying the correct orientation of the sample to be measured. In addition, the sample manipulator is also used to attach thermostats that give the temperature reading at the sample stage and other desired places. Our home-ARPES set up at LASCQM has a sample manipulator with 5-degrees of freedom including 3 translational and 2 rotational ones.

### *2.2.4 Ultra-high vacuum*

ARPES needs the surface of the sample to be atomically clean. This brings the necessity of UHV as an essential component in any ARPES experimental set ups. Typical ARPES measurements last for a day or two. If the vacuum is not ultra-high, then within no time the fresh and clean sample surface will be covered by layers of atoms turning it not a bad sample. In order to achieve UHV conditions inside the ARPES chamber, most of the ARPES systems typically use the following pumps.

1. In order to achieve a rough vacuum condition of $10^{-2}$ torr, *mechanical or roughing pumps* are used. These serve as the backing to the turbo pumps.

2. After bringing the pressure down to rough vacuum condition, *turbomolecular pumps* are used. These pumps can take the pressure down to $10^{-9}$ torr. The pumping speed of the turbo pumps depends on the size and the load of the chamber on which it is to be operated.

3. ARPES experiments are typically performed under pressure better than $10^{-10}$ torr. Therefore, *ion pumps* are needed to take the pressure down to such UHV condition. The ion pumps ionize the gasess and by means of an electric potential maintained between anodes and cathodes, accelerate them to deposit onto the cathode plates.

In addition to vacuum pumps, *baking* is also required to maintain UHV conditions. After pumping with roughing and turbomolecular pumps, the system is usually baked for about a week at temperatures instructed on the manual in order to remove the adsorbed gases inside the walls of the ARPES chambers.

## 2.3 Momentum and energy resolutions

From equation 2.7,

$$\Delta k_{\parallel} = \frac{1}{\hbar}\sqrt{2mE_{\mathrm{K}}}\cos\theta\ \Delta\theta \tag{2.26}$$

Therefore, the momentum resolution in ARPES depends on the angular resolution $\Delta\theta$. As $E_{\mathrm{K}} = h\nu - \Phi - |E_{\mathrm{B}}|$, equation 2.26 implies that the momentum resolution is better for lower photon energies for a given angular resolution limited by the beam spot size.

The total energy resolution has major contributions from the optics part and the analyzer setting. However, the true energy resolution is affected by other factors as well, an example is the residual field inside the ARPES chamber. The contribution to the energy resolution from the optical part depends on the bandwidth of the incident light. The contribution from the analyzer part depends on various factors including the slit width ($s$), pass energy ($E_{\mathrm{p}}$), mean radius of hemispheres ($R_m = \frac{R_1+R_2}{2}$) and the acceptance angle ($\alpha$) as [138]:

$$\Delta E_{analyzer} = E_{\mathrm{p}}\left(\frac{s}{R_m} + \frac{\alpha^2}{4}\right) \tag{2.27}$$

## 2.4 Sample preparation and cleaving

All the works under this dissertation have been performed using single crystals. A schematic showing the general process of sample preparation and cleaving is presented in Figure 2.7. First, the crystals are cut into flat and shiny pieces. They are then attached to sample holders using silver epoxy paste (torr seal in case of hard samples) and cured for a time and at a temperature given in the instruction (for handling epoxy or torr seal). Ceramic posts are attached on top of the cured samples again using silver epoxy paste (or torr seal) and are cured again at the instructed temperatures and

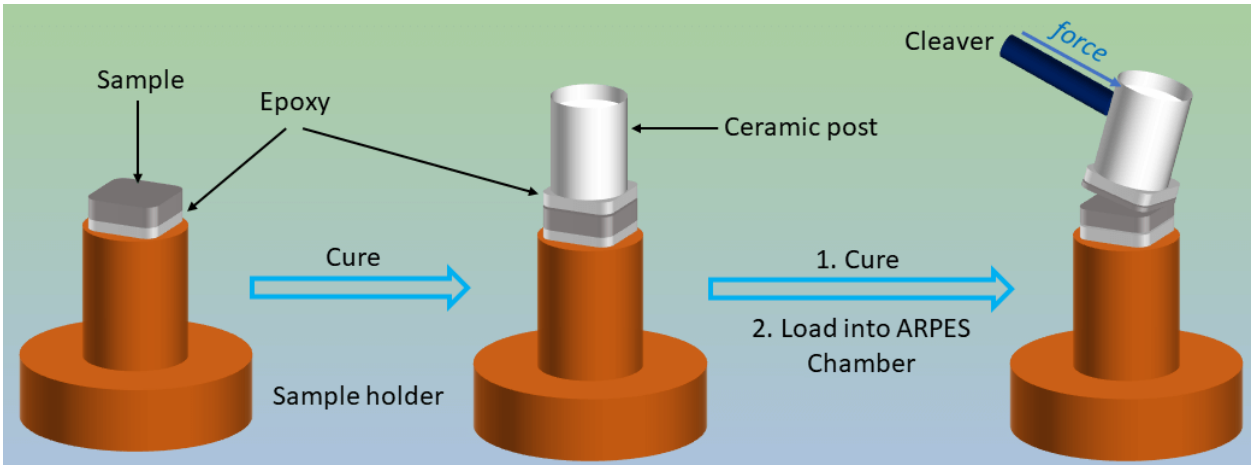


Figure 2.7: Sample preparation and cleaving.

for instructed times. Once they are properly cured, the sample holders (with samples and ceramic posts) are loaded into the ARPES chamber, which is kept under UHV conditions. After cooling the sample stage to a desired temperature, the samples are cleaved using the cleaver. During the cleaving process, the top unclean layers on the samples go away with the epoxy (or torr seal) attached to the ceraic posts, leaving behind a fresh and clean surface. The cleaved samples are then transferred to the measurement position using the sample manipulator stage and measured to get the ARPES data.

## 2.5 Time-resolved ARPES

The dependence of ARPES intensity (equation 2.20) on the Fermi-Dirac distribution function limits the conventional ARPES only upto the Fermi level. However, for many materials, the regions or features of interest may lie in the unoccupied out-of-equilibrium states above the Fermi level. Also, the electronic and phononic processes in quantum materials take place in picosecond to attosecond time scales. With time-resolution combined with conventional ARPES, the time-resolved

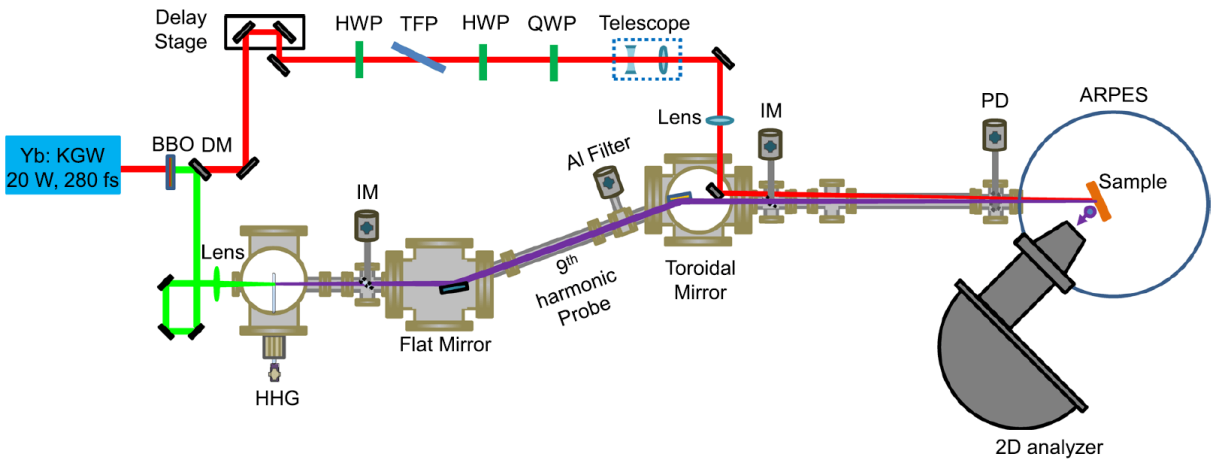


Figure 2.8: Schematic of the trARPES set up at LASCQM taken from [136].

ARPES (trARPES) provides an extensive tool to study the nonequilibrium electronic properties as well as electronic and phononic interactions. trARPES bases on pump-probe set up, where a pump pulse excites the electrons out-of-equilibrium and a subsequent probe pulse captures the momentum-resolved electronic dispersion. The time-resolved part comes from the delay between the pump and the probe pulses. This technique has already become an important tool to study the non-equilibrium properties including CDW melting [139], Cooper pair recombination [140], band renormalization effects [141, 142], exciton formation [143], electron-electron and electron-phonon interactions [144, 145, 146], and more.

LASCQM at the University of Central Florida has a time-resolved ARPES set up that uses commercial $\mathrm{Yb:KGW}$ amplifier that emits $280$ fs laser pulses of $1025$ nm wavelength (see Figure 2.8). A BBO crystal is used to generate $511$ nm second harmonic pulses and a subsequent dichroic mirror separates these second harmonic pulses with the fundamental $1025$ nm pulses. The fundamental pulse, passed through a delay stage and additional optical geometry, creates the pump line (see red path in the schematic in Figure 2.8). The second harmonic pulse (green path in Figure 2.8) is then passed through a high-harmonic generation capillary filled with Krypton gas. The high-harmonic

pulses and the residual $511\ \mathrm{nm}$ pulses are first reflected by a flat mirror and then by a torroidal mirror, both coated with silicon carbide to facilitate $9\mathrm{th}$ harmonic transmission, before focusing onto the sample. An aluminum filter placed in between these mirrors blocks the residual $511\ \mathrm{nm}$ pulses as well as lower-order harmonics. Therefore, $21.8\ \mathrm{eV}$ $9\mathrm{th}$ harmonic pulse ($7\mathrm{th}$ and $11\mathrm{th}$ harmonics as well, but very weak) creates the probe arm. Please refer to Ref. [136] for details. The set up has been successfully used to study the ultrafast phonon cooling mechanisms in the celebrated NLSM $\mathrm{ZrSiS}$ (see Ref. [146]).

## 2.6 Crystal synthesis and characterization

From performing various transport and spectroscopic measurements on the materials to testing their device application, most important step is to synthesize very high-quality crystals of those materials. Crystal growth, therefore, is vital in multiple disciplines of science and technology. ARPES experiments are usually carried out on single crystals and very high-quality of the crystals is desired as impurities can change the complexion of the electronic structure. Crystal growth is done using different techniques, which involve growth from solution, vapor, and melt [147]. At LASCQM in University of Central Florida, we mainly employ Bridgman technique, which is a melt growth technique, and chemical vapor deposition, which as name suggests is a vapor growth technique. The Bridgman technique is a simple technique that can grow a large range of materials and can be employed in two configurations - horizontal and vertical. Polycrystalline form of the material to be grown as single crystals is heated above the melting point and slowly translated to a cooler temperature below the melting point. In order to have a desired orientation, a seed crystal is used, which initiates the growth of the crystal at the melt-seed interface. Chemical vapor transport, on the other hand, uses as a temperature profile that is maintained at different values at the volatilization side and growth side. The process starts at the volatilization side, where the

starting materials are vaporized, then transported and finally deposited at the growth side as single crystals. An easily vaporizable compound such as Iodine is used as a transport agent.

After growing the crystals, it is very important to characterize them to make sure a correct material is being grown. X-ray diffraction (XRD) is widely used for the structural characterization and energy-dispersive X-ray analysis (EDAX) is commonly used for compositional homogeneity. XRD can be done on powdered sample (powdered XRD) or on single crystals (single crystal XRD). When monochromatic X-rays are incident on the sample, diffraction occurs according to the Bragg's equation [148] $n\lambda = 2d\sin\theta$, where $n$ is a positive integer, $\lambda$ is the wavelength of the incident X-rays, $d$ is the interplanar spacing, and $\theta$ is the diffraction angle. By collecting the intensity of diffracted rays, complete structural analysis can be performed. The intensity peaks in the XRD data come from a unique set of repeating planes in the structure of the sample. While powder diffraction will give more diffraction peaks corresponding to a number of random orientation of crystallites, single-crystal XRD shows discrete diffraction peaks depending upon the orientation of the crystal. In Figure 2.9(a), we present the images of the Bridgman technique-grown $\mathrm{Bi_2Se_3}$ crystals and the result of the powder XRD. Spectroscipic results of tr-ARPES measurements on the crystals are presented in Figures 2.9(b) and 2.9(c).

The synthesis of single crystals may not provide a sample with the highest quality. For example, the single crystals of the highly studied topological insulator $\mathrm{Bi_2Se_3}$ have usually $\mathrm{Se}$-defects and the single crystal becomes an n-type semiconductor rather than a insulator leading to bulk contribution to the transport signatures hampering the efforts to isolate the transport signatures coming from the 2D surface electrons [149]. The thin film growth of quantum materials comes handy as the defects present in the sample can be significantly reduced with thin films giving high-quality crystalline samples for characterization and potential uses in device settings. Also, film growth over can be flexible to manipulate the number of layers thereby giving chance to study the thickness dependent properties of the quantum topological materials [150]. At LASCQM in University of Central

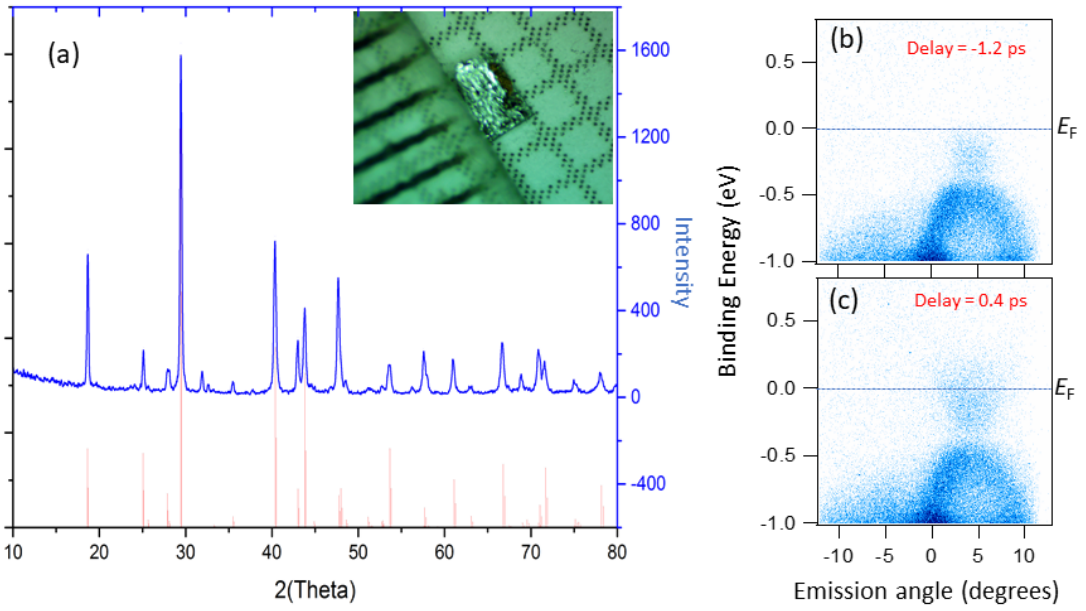


Figure 2.9: Growth and characterization of $Bi_2Se_3$. (a) Results of powdered XRD on $Bi_2Se_3$ samples grown at LASCQM in University of Central Florida and the picture of a sample crystal (inset). (b)-(c) Spectroscopic characterization of the samples using ARPES and pump-probe set ups at LASCQM. Clear photoemission intensity can be seen above the Fermi level when the pump pulse hits the sample $0.4$ ps before the probe pulse.

Florida, we are setting up a molecular beam epitaxy (MBE) chamber to grow thin films of various topological quantum materials and magnetic/non-magnetic 2D materials. MBE has been acknowledged as one of the best growth techniques which provides atomic layer by atomic layer growth of high quality crystalline thin films under ultra-high vacuum conditions minimizing the contamination on the sample [150, 151, 152, 153, 154, 155]. The MBE technique also enables large area growth as well as provides the ability to controllably dope the materials. Figure 2.10(a) presents a schematic of the lab set up with the Scienta Omicron LAB10 MBE system, which is presented in Figure 2.10(b). A schemtaic of multi-source MBE setup is shown in Figure 2.10(c). A MBE chamber consists of elemental sources in Knudsen effusion cells. The Knudsen effusion cells are heated in order to produce molecular beams of the elements. The shutters can be opened or closed

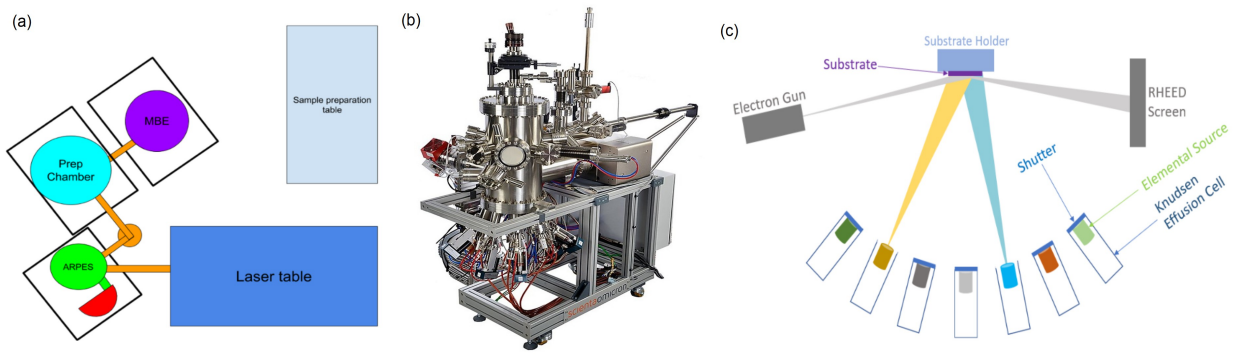


Figure 2.10: MBE at LASCQM in University of Central Florida. (a) Schematic of the lab set up at LASCQM with MBE chamber, preparation chamber and the ARPES chamber. (b) Scienta Omicron LAB10 MBE system to be set up. (c) A schematic of a multiple source MBE system equipped with RHEED arrangement.

to allow or block the molecular beams coming out of the effusion cells to pass through them. On the other side lies a substrate on which the thin films are to be grown. The molecular beams that are passed through the open shutters pinge on the substrate which is heated to a suitable temperature and for crystalline layers. In order for the large area growth to be achieved, the substrate holder is rotated at suitable speeds. As the substrate provides the basis of the high-quality thin films to be grown, the substrate itself should be of high quality. In order to monitor the layer by layer growth of the desired material, the MBE chamber is equipped with a reflection high-energy energy diffraction (RHEED) arrangement [152]. This arrangement consists of an electron gun, from which an electron beam is passes to the growing film at very small angles to the substrate surface so that these electron beams do not cross the path of the molecular beams coming from the effusion cells. On the other side of the electron gun is a fluorescent screen which shows the diffraction pattern formed by the diffracted electrons. After preparing a thin film of required thickness, the sample is then transferred to the preparation chamber and then to the ARPES chamber with the aid of the transfer arms equipped with the chambers. Then, the complete spectroscopic characterization of the thin films is carried out.

# CHAPTER 3: STUDY OF THE EFFECT OF MAGNETIC TRANSITION IN THE ELECTRONIC STRUCTURE OF A HIGHER ORDER TOPOLOGICAL INSULATOR CANDIDATE ANTIFERROMAGNET

The results of this work are published in Sabin Regmi *et al.*, Physical Review B **102**, 165153 (2020).

While the 3D TIs with gapless conducting channels on the surface have been revolutionizing the field of topological quantum materials, the recently discovered HOTIs bring a distinct novelty in this family of materials because of their ability to host conducting channels along the hinges of the crystals. In this work, we report the electronic structure of a candidate HOTI material $EuIn_2As_2$, which is antiferromagnetic and is predicted to host higher order topological states when the magnetic moments are oriented *out of plane*. We directly show the evolution of the bands near the Fermi level with magnetic transition via ARPES measurements. This study brings out $EuIn_2As_2$ as an important material platform that can be a ground to study the interplay between topology and magnetic ordering.

## 3.1 Introduction

In TIs, the bulk-boundary correspondence connects the topological states at the boundary with the bulk of the material. In a 3D TI, the boundary is a 2D surface on which the surface state resides and is a result of the non-trivial topology of the bulk [3, 4, 25, 156]. The surface state, which forms a Dirac cone in energy-momentum space, is prevented from backscattering and localization as long as the TR symmetry remains intact. In the recently discovered TI with higher-order topology, called HOTI [75], this bulk-boundary correspondence does not apply. The topological state in a

HOTI is still a result of the non-trivial topology of the bulk, however, it is not present on the 2D surface, which is gapped. The topological state resides along the hinges of the crystal thereby creating a novel bulk-surface-hinge correspondence [73, 74, 75]. Such topological hinge state may be protected by crystalline symmetries such as reflection, rotational, and inversion symmetries [74, 75, 76, 77, 79].

While HOTI phase has been realized in electronic, phononic, and photonic systems [80, 81, 82], experimental realization in crystalline systems is rather rare and this novel insulating state is mostly limited to theoretical predictions [75, 86, 157, 158, 159, 160]. By using scanning tunneling microscopy, Josephson interferometry and first-principles calculations, higher-order topology has been reported in crystalline $\mathrm{Bismuth}$ [83]. Momentum-resolved spectroscopic investigation of the candidate materials is an important step toward the experimental exploration of this novel state, however, such investigations have been lacking.

Mixing magnetism in a TI opens up a gap at the surface Dirac point in absence of further crystalline symmetries protecting the Dirac crossing [34]. However, such TIs with massive surface Dirac fermion are still interesting because of the possibility of various novel phenomena they can exhibit including QAH and axion insulating states [31, 32, 33, 34]. In the presence of crystalline symmetries in combination with broken TR symmetry, various magnetic topological states including antiferromagnetic TI can be realized [32, 34, 161, 162, 163, 164, 165, 166]. Intrinsic magnetic materials with topologically non-trivial band structures are therefore interesting systems to study, however, limited availability of such materials has held back the experimental realization of magnetic states in such topological quantum systems.

In this work, we have carried out a systematic ARPES characterization of $\mathrm{EuIn_2As_2}$, which is magnetic and is also a candidate material for HOTI phase. Theoretical calculations predict an axion insulating state with parity-based topological invariant $\mathbb{Z}_4 = 2$ when $\mathrm{Eu}^{2+}$ magnetic moments are

oriented both *in plane* and *out of plane*. The ARPES results reveal the band structure evolution across the antiferromagnetic transition, where we observed a splitting of the linear hole-like band near the Fermi level below the transition temperature. Electrical resistivity measurement shows metallic nature with Kondo-type behavior slightly above the transition temperature. Our theoretical and experimental results depict a rich topology in $\mathrm{EuIn_2As_2}$ in both above and below the magnetic transition. $\mathrm{EuIn_2As_2}$ is, therefore, a great platform for the study of intermix of magnetism and topology.

## 3.2 Results

### *3.2.1 Crystal structure and sample characterization*

$\mathrm{EuIn_2As_2}$ belongs to the hexagonal crystal system with space group number $194$ ($\mathrm{P6_3}/mmc$). The crystal structure is shown in figure 3.1(a). The atomic layers of Europium, Indium, and Arsenic occupy the Wyckoff positions $2a(0,0,0)$, $4f(\frac{1}{3},\frac{2}{3},0.17155)$, and $4f(\frac{1}{3},\frac{2}{3},0.60706)$, respectively. The out-of-plane lattice parameter ($c = 17.889$ Å) is much larger than the in-plane lattice parameters ($a = b = 4.207$ Å) [167]. In figure 3.1(b), the 3D bulk BZ and its projection on to the $(001)$ surface are presented with high-symmetry points labeled. The characteristic peaks of the orbitals of $\mathrm{Eu}$, $\mathrm{In}$, and $\mathrm{As}$ in the core-level spectrum (figure 3.1(c)) indicate the good quality of the single-crystals of $\mathrm{EuIn_2As_2}$ used in our experiments. The result of the transport measurement presented in figure 3.1(d) shows that $\mathrm{EuIn_2As_2}$ has metallic conductivity with fairly large resistivity ($630\ \mu\Omega\mathrm{cm}$) at room temperature. A sharp maximum appears at the antiferromagnetic transition temperature $T_N \sim 16$ K. Below $T_N$, the resistivity gradually falls with lowering temperature. This indicates the reduction in scattering of conduction electrons with $\mathrm{Eu^{2+}}$ magnetic moments. Saturation of resistivity can be seen at very low temperatures. The value of residual resistivity around $0.4$ K is about $180\ \mu\Omega cm$. A Kondo-type behavior is observed slight above the transition temper-

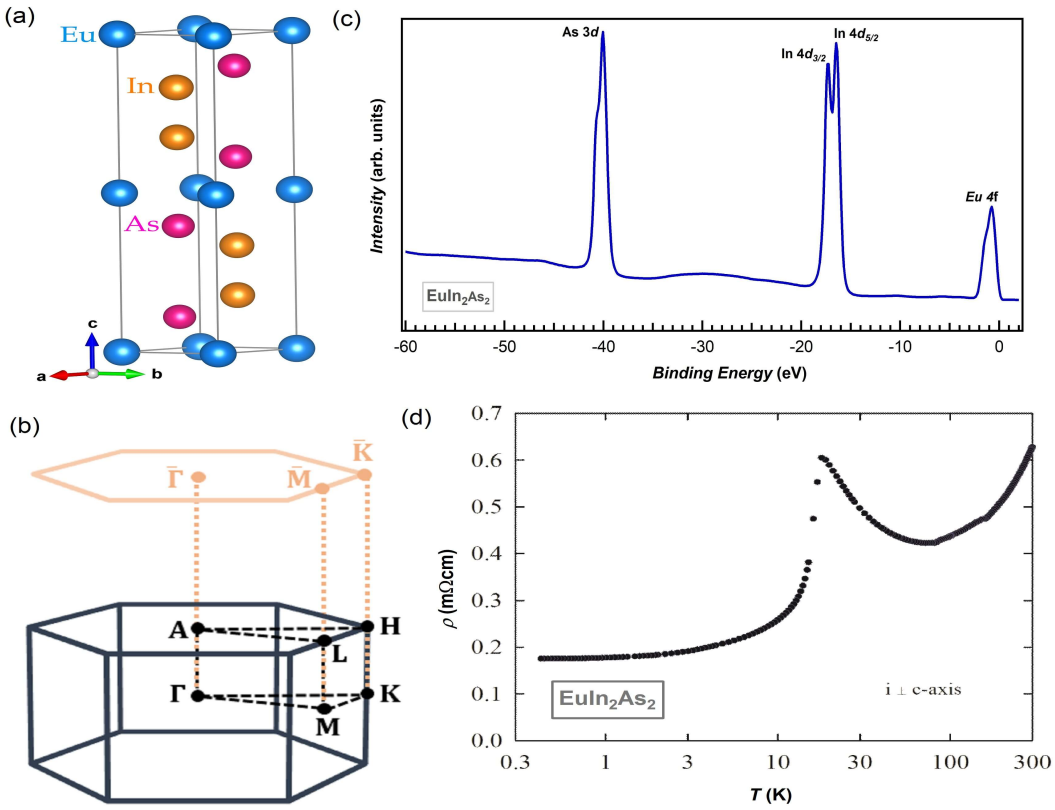


Figure 3.1: Crystal structure and sample characterization. (a) Crystal structure of $EuIn_2As_2$, where blue, yellow, and pink spheres represent Eu, In, and As atoms, respectively. (b) Three-dimensional bulk BZ and projected (001) surface BZ with high-symmetry marked. (c) Core level spectrum indicating the presence of Eu 4*f*, In 4*d*, and As 3*d* orbitals. (d) Electrical resistivity measured as a function of temperature with current perpendicular to the crystallographic c-direction.

ature, where resistance starts to increase with decreasing temperature. This kind of behavior was previously observed and attributed to the spin scattering of the carriers by the localized magnetic moments approaching the antiferromagnetic ordering [167].

### *3.2.2 Bulk band calculations and prediction of higher-order topological phase*

Depending upon the orientation of $\mathrm{Eu}^{2+}$ magnetic moments, the antiferromagnetism in $\mathrm{EuIn_2As_2}$ can have different configurations. Here, we define two configurations, AFM-B and AFM-C, as the antiferromagnetic configuration when the $\mathrm{Eu}^{2+}$ magnetic moments are *in plane* and *out of plane*, respectively. The minimum unit cell required to represent both AFM-B and AFM-C is the same as the minimum unit cell in the non-magnetic phase. The band structure in the antiferromagnetic configurations is not expected to have addition folding. In figure 3.2, we present the calculated bulk bands in the antiferromagnetic phase. The AFM-B and AFM-C phases are almost degenerate, there is only a less than $1\ \mathrm{meV}$ energy difference per unit cell, which agrees with the previously reported results [157]. In the absence of SOC (figure 3.2(a)), an inverted band gap of about 460 meV is opened in between the valence and conduction bands at the $\Gamma$ point. Along $\Gamma - \mathrm{K}$ direction, the bands touch creating a symmetry protected gapless dispersion. Along $\Gamma - \mathrm{M}$, however, a small gap exists in bewteen the bands. A significant gap is introduced when the SOC is taken into account as seen in bulk band structures in 3.2(b) and 3.2(c) for AFM-B and AFM-C, respectively.

From the bulk band calculations, we found that there is a band inverted gap around the $\Gamma$ point in both AFM-B and AFM-C configurations. To determine their topological state, we calculated the parity-based $\mathbb{Z}_4$ topological invariant,

$$\mathbb{Z}_4 = \sum_{i=1}^{8} \sum_{n=1}^{N_{occ}} \frac{1 + \zeta_n(\Gamma_i)}{2} mod 4, \tag{3.1}$$

where $N_{occ}$ represents the number of occupied bands and $\zeta_n(\Gamma_i)$ defines the parity at the TRIM point $\Gamma_i$ for $n^{th}$ band. The calculation resulted in $\mathbb{Z}_4 = 2$ for both the antiferromagnetic configurations. This means, antiferromagnetic $\mathrm{EuIn_2As_2}$ in both AFM-B and AFM-C configurations is an axion insulator. In addition, the calculation of $\mathbb{Z}_2$ topological invariants in the paramagnetic phase yielded ($\nu_0; \nu_1\nu_2\nu_3$) = $(1, 000)$, indicating a TI phase. In the AFM-B configuration, there exist two

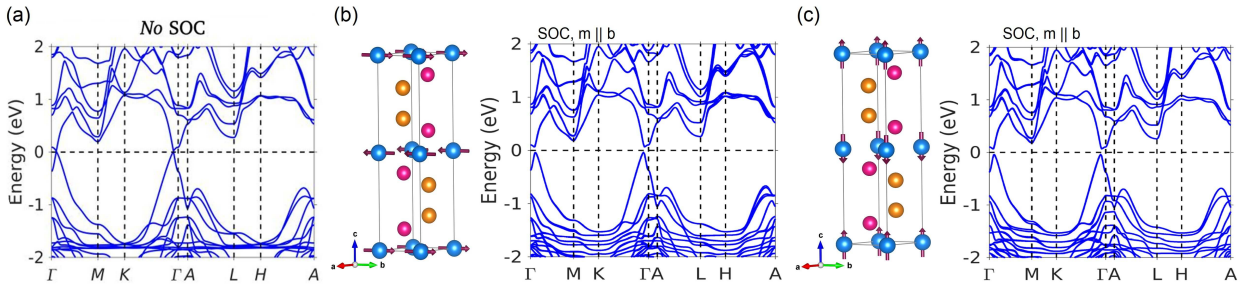


Figure 3.2: Bulk band calculations. (a) Calculated bulk band structure without considering the effect of SOC. (b)-(c) Crystal structure (left panels) and band structures (right panels) in the AFM-B and AFM-C phases, respectively.

mirror planes with a non-zero mirror Chern number - $k_y = 0$ and $k_z = 0$, which is not the case in AFM-C configuration, which does not preserve any mirror plane. The AFM-B configuration, therefore, supports a TCI phase and the AFM-C cofiguration supports a HOTI phase with $\mathbb{Z}_4 = 2$.

### *3.2.3 Observation of band-splitting below antiferromagnetic transition*

After the prediction of the possibility of various topological phases in $\mathrm{EuIn_2As_2}$, we proceed to the results from our ARPES measurements. In figure 3.3, we present the ARPES measured constant energy contours measured with a photon energy of $55\ \mathrm{eV}$ at two different temperatures, $22\ \mathrm{K}$ and $8\ \mathrm{K}$, which correspond to paramagnetic and antiferromagnetic phases, respectively. A circular pocket centered at the $\Gamma$ point can be observed at the Fermi surface (FS) growing in size with binding energy indicating the hole nature of the associated bands. In the antiferromagnetic phase (lower panel in figure 3.3), another circular pocket emerges inside the outer circular pocket. The inner pocket is absent in the data at $22\ \mathrm{K}$. This extra inner pocket in the antiferromagentic can be seen growing with rise in binding energy before merging with the outer pocket at around $300\ \mathrm{meV}$. A new rectangular pocket appears in both paramagnetic and antiferromagnetic phases at a higher binding energies as seen from the constant energy contour taken at a binding energy of $500\ \mathrm{meV}$.

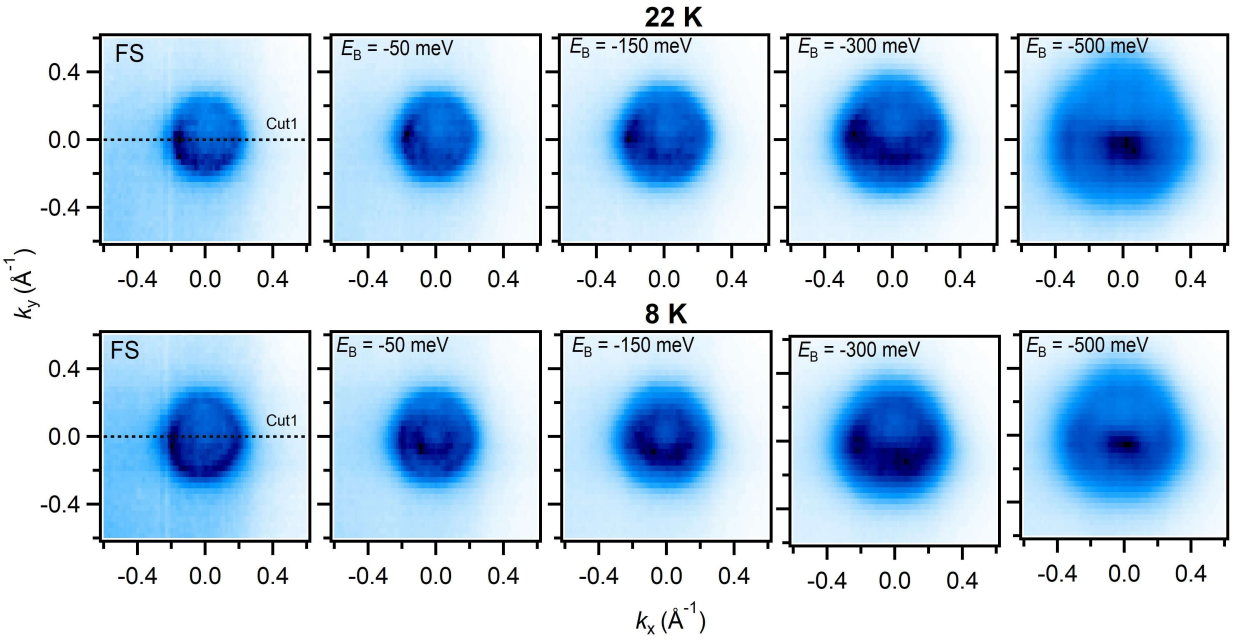


Figure 3.3: ARPES measured constant energy contours at two different temperatures, $22$ K (upper panel) and $8$ K (lower panel). The values of binding energy at which the constant energy contour are taken are noted. Data were collected at the ALS beamline 10.0.1.1 with a photon enrgy of $55$ eV.

In order to better illustrate the appearance of the extra circular pocket in the antiferromagnetic phase, second derivative plots of constant energy contours at a binding energy energy of $50$ meV are presented in figure 3.4(a). The inner circular pocket is clearly visible in the data at $8$ K, but is absent in the data at $22$ K. To understand the underlying electronic band dispersion, we present the dispersion maps along the $\overline{\mathrm{K}} - \overline{\Gamma} - \overline{\mathrm{K}}$ direction in figure 3.4(b) and their second derivative plots in figure 3.4(c). $\overline{\mathrm{K}} - \overline{\Gamma} - \overline{\mathrm{K}}$ corresponds to the $\mathrm{Cut1}$ direction represented by a dashed line in the FS maps in figure 3.3. A linear hole-like band can be clearly observed to be crossing the Fermi level in the paramagnetic phase. In antiferromagnetic phase, there is another hole-like band that appears to cross the Fermi level closer to the $\Gamma$ point. The presence(absence) of the inner band in the antiferromagnetic (paramagnetic) phase is further supported by the two-peak (single-peak) feature in the vicinity of the Fermi level in the momentum distribution curves (MDCs) presented in

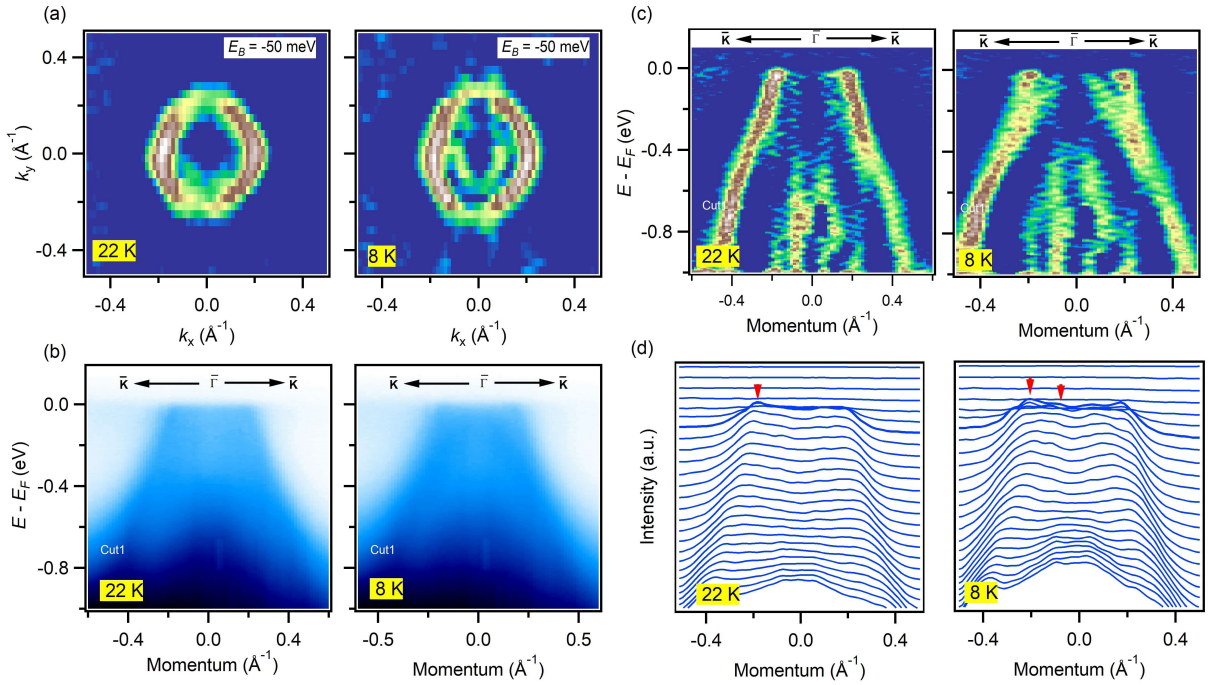


Figure 3.4: Observation of band-splitting in the antiferromagnetic phase. (a) Second derivative of the constant energy contour at a binding energy of $50$ meV in the paramagnetic (left) and antiferromagnetic (right) phases. (b) Dispersion maps taken along the cut1 direction represented by the dashed line in Fig. 3.3(a), i.e. $\overline{\mathrm{K}}-\overline{\Gamma}-\overline{\mathrm{K}}$ direction, at $22$ K (left) and $8$ K (right). (c) Second derivative plots of the dispersion maps in Fig. 3.4 (b). (d) Momentum dispersion curves corresponding to dispersion maps in Fig. 3.4 (b) taken within energy window of $0.5$ eV below the Fermi level. Data were collected at the ALS beamline 10.0.1.1 with a photon energy of $55$ eV.

figure 3.4(d). The outer hole-like band remains robust both above and below the antiferromagnetic ordering, however, the inner band is sensitive to the presence of antiferromagnetic order. This inner band extends upto around $400$ meV below the Fermi level before merging with the outer hole band.

The absence of the inner band is also depicted in our measurements at a different paramagnetic temperature of $46$ K. The results of the measurements are presented in figure 3.5. Similar to the data at $22$ K, a single circular pocket is present around the $\Gamma$ point that grows with increasing binding energy (figure 3.5(a)). The dispersion map along the $\overline{\mathrm{K}}-\overline{\Gamma}-\overline{\mathrm{K}}$ direction has a single linear hole band all the way upto the Fermi level (figure 3.5(b)), which is clear from the second

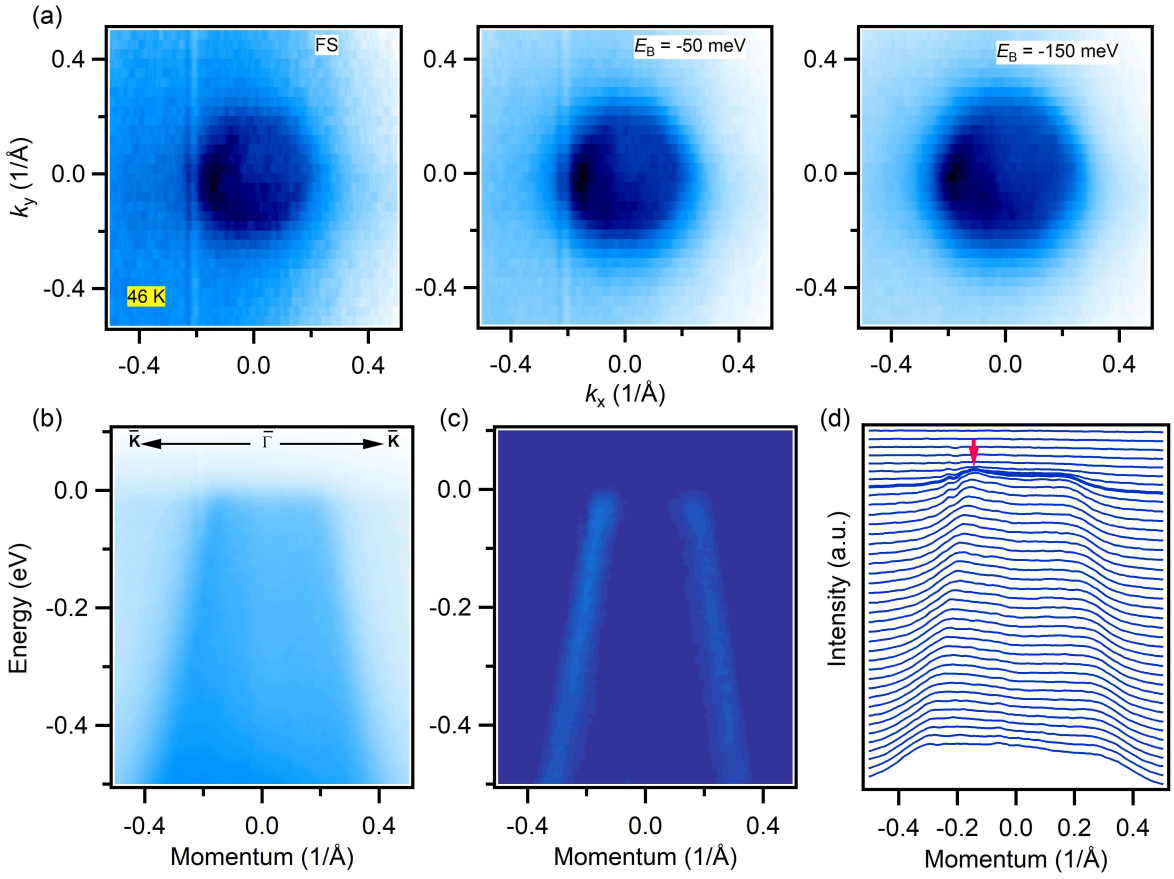


Figure 3.5: ARPES results at $46$ K. (a) Fermi surface (leftmost) and energy contours at the labeled binding energies. (b) Energy versus momentum dispersion along $\overline{\mathrm{K}}-\overline{\Gamma}-\overline{\mathrm{K}}$. (c) Second derivative plot of band dispersion in (b). (d) Momentum distribution curves for band dispersion in (b). Data were collected at the ALS beamline 10.0.1.1 with a photon energy of $55$ eV at a temperature of $46$ K.

derivative plot and MDCs in figures 3.5(c) and 3.5(d), respectively. The linear dispersion of band near the Fermi level indicates a possible Dirac cone above the Fermi level. In order to predict the energy position of the possible Dirac point, we extracted the peak positions in the MDCs of band dispersion near the Fermi level in the paramagnetic phase (represented by the red circles in figure 3.6(a)). From the extrapolated linear fit of the peak positions, we obtained the energy position of the potential Dirac point to be about $320$ meV above the Fermi level (figure 3.6(b)).

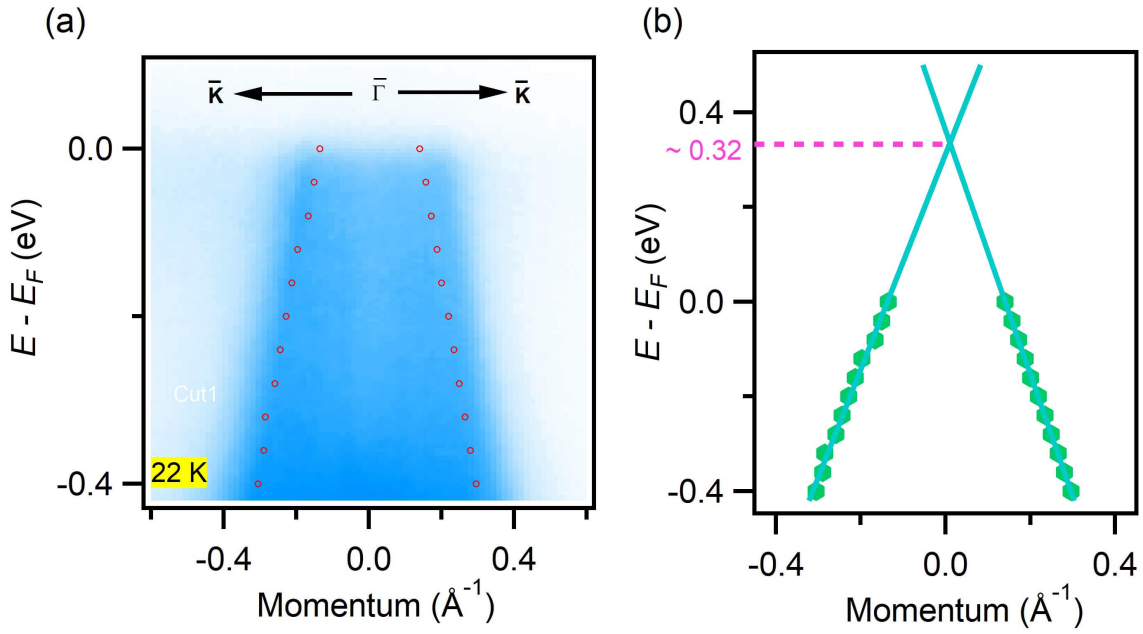


Figure 3.6: Prediction of Dirac point position. (a) Band dispersion along $\overline{\mathrm{K}} - \overline{\Gamma} - \overline{\mathrm{K}}$ direction within $400$ meV below the Fermi level. The red circles denote the peak position in the momentum distribution curves. (b) Fitting of the momentum distribution curves peak positions to determine the possible energy position of the Dirac point above the Fermi level. Data were collected at the ALS beamline 10.0.1.1 with a photon energy of $55$ eV at a temperature of $22$ K.

### *3.2.4 Band splitting in surface state calculations*

In order to support the band splitting near the Fermi level observed in our experimental results, we performed surface state calculations for the As terminated $(001)$ surface with a modified surface potential. The calculated results are shown in figure 3.7. A two-fold degenerate hold band can be seen crossing the Fermi level in the paramagnetic phase as observed in the experimental results at $22$ K and $46$ K. The band forms a non-trivial Dirac cone above the Fermi level. In the antiferromagnetic phase, both AFM-B and AFM-C configurations, the band degeneracy is lifted resulting into two-bands near the Fermi level. Therefore, below the Fermi level, both AFM-B and AFM-C configurations have similar band structures and reproduce the band-splitting near the Fermi level.

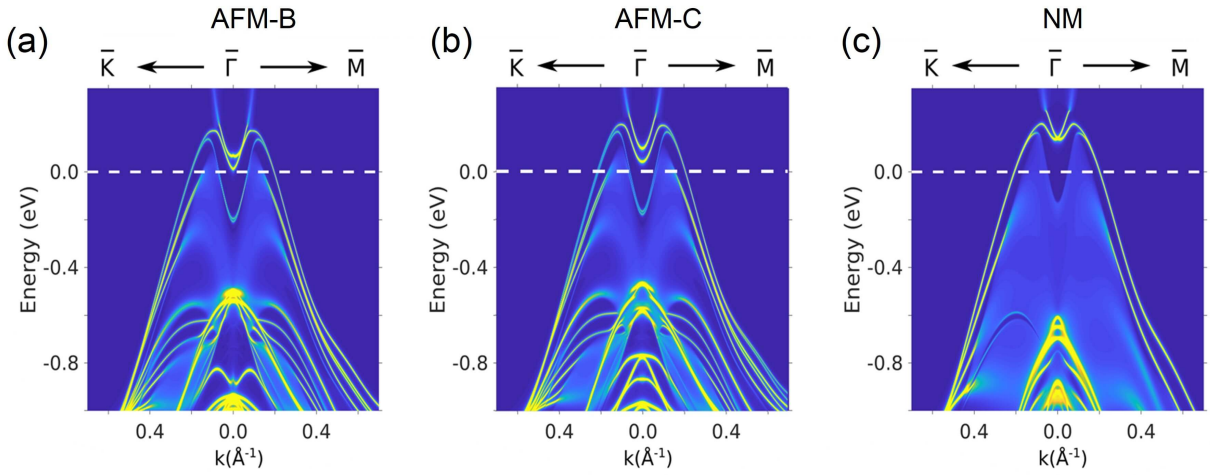


Figure 3.7: Theoretical calculations on the (001) surface. (a)-(c) Calculated band dispersions on the (001) surface for (a) AFM-B, (b) AFM-C, and (c) non-magnetic phases.

Consistent with the prediction of TCI phase in AFM-B configuration, a gapless type-II Dirac state lies above the Fermi level. On the other hand, the surface state is gapped above the Fermi level in the AFM-C configuration, which is in accordance with the prediction of HOTI phase in this antiferromagnetic configuration. Experimental study of the nature of electronic states above the Fermi level is necessary to determine the exact topological phase of antiferromagnetic $EuIn_2As_2$.

### 3.3 Conclusion

To conclude, this study on $EuIn_2As_2$ by employing ARPES with support from theoretical calculations reveals the evolution of electronic structure across the antiferromagnetic transition at $16$ K obtained from transport measurement. While a single doubly-degenerate hole band crosses the Fermi level in the paramagnetic phase, it splits into two-bands near the Fermi level in the antiferromagnetic regime. Near the Fermi level, the hole band has linear dispersion with potential Dirac point at an energy above it, which via linear fit of peak positions in MDC is found to be

around $320\ \mathrm{eV}$. Theoretical calculation of $\mathbb{Z}_2$ topological invariants indicate a potential TI phase and parity-based $\mathbb{Z}_4$ calculation imply an axion insulating state in the antiferromagnetic phase with both AFM-B and AFM-C configurations, which further support TCI phase and HOTI phase, respectively. Surface state calculations support the observation of magnetic band splitting in experimental results and predict a type-II Dirac surface state in AFM-B configuration and a gapped surface state in AFM-C configuration, both above the Fermi level. Therefore, this study reveals a rich topology in $\mathrm{EuIn_2As_2}$ and brings out this compound as an important material system to study the interplay among topology and magnetism. It also lays a way for the further experimental studies on the states above the Fermi level in order to know the exact magnetic and non-magnetic topological states in $\mathrm{EuIn_2As_2}$.

## 3.4 Experimental and computational methods

### *3.4.1 Crystal growth and characterization*

Single crystals of $\mathrm{EuIn_2As_2}$ were grown using the flux technique [168]. The crystal structure of the synthesized crystals was then verified using powder X-ray diffraction measurements utilizing Kuma-Diffraction KM4 four-circle X-ray diffractometer by using $\mathrm{Cu\ K}\alpha$ radiation. To verify the chemical composition of the single crystals, energy-dispersive X-ray analysis was performed by using a FEI scanning electron microscope, which is equipped with an EDAX Genesis XM4 spectrometer.

### *3.4.2 Electrical transport measurements*

Electrical transport measurements were carried on a Quantum Design PPMS platform utilizing four-point ac technique. Electrical contacts were made using the silver epoxy paste. The current

direction was along the $ab$ plane.

### *3.4.3 First-principles calculations*

Theoretical calculations of the band structure were carried out using the density functional theory (DFT) approach [169, 170] with projector-augmented-wave (PAW) pseudopotential [171, 172] in the Vienna ab initio simulation package (VASP) software [173, 174]. Perdew-Burke-Ernzerhof (PBE) type generalized gradient approximation (GGA) approximation was used to account for the exchange-correlation effects [175]. To account for the on-site Coulomb interaction, $\mathrm{U_{eff}} = 5\ \mathrm{eV}$ for Eu $4f$-electrons was added within the GGA + Hubbard U (GGA+U) scheme [176]. First-principles tight-binding Hamiltonian was employed for the calculation of the topological properties, which was generated using the VASP2WANNIER90 interface [177]. Iterative Green's function scheme was employed to get the surface spectrum via WANNIERTOOLS package [178].

### *3.4.4 ARPES measurements*

The high-resolution ARPES measurements were performed using the synchrotron light source available at the Advanced Light Source (ALS), Berkeley at Beamline 10.0.1.1, which is equipped with a high-efficiency R4000 electron analyzer. For the ARPES measurements, the angular and energy resolutions were maintained better than $0.2^{\circ}$ and $20\ \mathrm{meV}$, respectively. Flat samples prepared on copper posts were loaded into the ARPES chamber maintained at ultra-high vacuum better than $10^{-10}$ torr and then cleaved in-situ. Cermaic posts were mounted on top of the samples using the silver epoxy paste to cleave the top surface of the sample thereby exposing a fresh shiny surface for ARPES measurements. Experiments were conducted within $8$ to $50\ \mathrm{K}$ temperature in order to study the electronic structure across the magnetic transition temperature of $\mathrm{EuIn_2As_2}$, which is $\sim\ 16\ \mathrm{K}$.

# CHAPTER 4: OBSERVATION OF GAPLESS NODAL-LINE STATES IN LANTHANIDE BASED SEMIMETALS

Some results of this work have been published in Sabin Regmi *et al.*, Physical Review Materials **6**, L031201 (2022) and some are currently under review (pre-print is available at arXiv:2210.00163).

$\mathrm{ZrSiS}$ and $\mathrm{ZrSiS-type\ 111}$ materials have attracted most research studies out of the NLSMs because of ability to host various topological fermionic states. Lanthanide element ($Ln$) based material systems in this family may bring magnetism and electronic correlations into play due to the $4f$ electrons of the Lanthanide elements. Here, we have carried out studies on samarium- and neodymium-based $\mathrm{ZrSiS-type\ 111}$ systems - $\mathrm{SmSbTe}$ and $\mathrm{NdSbTe}$ - to investigate the electronic structure and possible existence of topological states. Through ARPES measurements, we reveal the presence of multiple gapless Dirac nodal lines present in these system as predicted by first-principles calculations. These studies provide grounds to understand the evolution of the $Ln$-dependent topological electronic structure in the $Ln\mathrm{SbTe}$ family of materials.

## 4.1 Introduction

Nodal-line semimetals have been attracting research interests because of the unique topological band crossing that persists along a line or a loop [7, 44, 45, 46]. After the experimental realization of nodal-line state in $\mathrm{ZrSiS}$, it quickly caught the eye of researchers owing to its ability to host nodal-line fermion and nonsymmorphic symmetry protected topological fermion that arises from the $\mathrm{Si}$-square-net [45, 46], and not to forget the excellent quality and cleavibility of the crystals. Following this realization, studies began to galore on $\mathrm{ZrSiS}$ and its family of $111$ materials with group-IV square net [179, 180, 181, 182, 183, 184, 185, 186, 187, 188, 189, 190]. Unconventional

magnetoresistive properties [191, 192, 193, 194], unconventional mass enhancement around the Dirac nodes [195], field induced topological phase transition [191], flat optical conductivity [196], etc. observed in $\mathrm{ZrSiS}$ or similar $111$ materials highlight the rich exotic properties that the materials in the $\mathrm{ZrSiS}$-type family.

Inclusion of magnetism and correlation effects in $\mathrm{ZrSiS}$-type materials would provide excellent opportunities to explore what novel and exotic properties the interaction of various types of topological fermions with these parameters would lead to. The $Ln$-based systems -$Ln\mathrm{SbTe}$ - provide platforms for such exploration because of potential correlation effects from $4f$ electrons and long range ordering of $Ln$ magnetic moments. In addition, these systems feature square net of $\mathrm{Sb}$ atoms in their crystal structure, which has been less common than the ones with $\mathrm{Si}$ square net. Therefore, the study of electronic properties of these systems is important, however, such reports are limited. The limited studies on the electronic structure hint that the electronic and topological properties of these systems depend on the choice of $Ln$ element. $\mathrm{GdSbTe}$ possesses an antiferromagnetic Dirac state that is protected by the broken TR symmetry in combination with rotoinversion symmetry even in the antiferromagnetic regime in addition to the nodal-line state [197]. $\mathrm{CeSbTe}$ can be a home to several topological states with tuning of ordering of $\mathrm{Ce}$ magnetic moments [198] and non-symmorphic Dirac state is more symmetric in this compound compared to that of $\mathrm{ZrSiS}$ due to the greater strength of SOC [199]. With $Ln = \mathrm{La}$, we are looking at a system that is reported to host gapless nodal-line even with SOC considered [200], on the other hand, $Ln = \mathrm{Ho},\ \mathrm{Dy}$ gives a system that is shown to possess significant gap along all high-symmetry directions induced by SOC [201]. These results show that more measurements of the electronic structure with different $Ln$ elemental choices are necessary to understand how the electronic structure and topology in this $Ln\mathrm{SbTe}$ family of materials evolve with change in $Ln$, which also implies a change in SOC.

In this work, we carry out experimental investigations on the electronic properties in two $Ln\mathrm{SbTe}$ compounds - $\mathrm{SmSbTe}$ and $\mathrm{NdSbTe}$ - by utilizing high-resolution ARPES supported by DFT cal-

culations as well as transport, thermodynamic, and magnetic measurements. Our experimental results show the presence of gapless nodal-lines in these systems along the bulk $\mathrm{X}-\mathrm{R}$ direction. Polarization dependent measurements detect a nodal-line across the $\Gamma-\mathrm{M}$ direction formed by steep bands that are sensitive to light polarization in $\mathrm{NdSbTe}$. Surface states are observed at the corner of the SBZ in both the compounds. The experimental measurements are well backed by the DFT calculations. Overall, this work reveals the topological electronic structure in novel platforms $\mathrm{SmSbTe}$ and $\mathrm{NdSbTe}$, which will provide insight towards understanding of how the electronic properties in $Ln\mathrm{SbTe}$ systems evolve with $Ln$ elemental choice. We would like to note that a study on $\mathrm{SmSbTe}$, which we became aware of during the manuscript preparation phase of this work, also demonstrate the presence of Dirac nodal-lines in this system [202].

## 4.2 Results

The first part of this section presents and discusses the results obtained on $\mathrm{SmSbTe}$ and the second part presents and discusses the results obtained for $\mathrm{NdSbTe}$.

### *4.2.1 Results on* $\mathrm{SmSbTe}$

#### *4.2.1.1 Crystal structure and transport characterization*

$\mathrm{SmSbTe}$ crystallizes in a PbFCl-type crystal structure (nonsymmorphic space group No. 129). A quintuple $\mathrm{Te}-\mathrm{Sm}-\mathrm{Sb}-\mathrm{Sm}-\mathrm{Te}$ layer along crystallographic $c$-direction is constituted by layers of $\mathrm{Sm}-\mathrm{Te}$ and square planes of $\mathrm{Sb}$ arranged in such a way that the $\mathrm{Sb}$ planes are sandwiched in between the $\mathrm{Sm}-\mathrm{Te}$ layers (see figure 4.1(a)). Global $C_{4\nu}$ symmetry is supported by each atomic layers, however, local $C_{4\nu}$ symmetry at the $\mathrm{Sb}$ sites is broken. $\mathrm{Sb}$ square plane acts as a glide plane that respects the $(M_z \mid \frac{1}{2}\frac{1}{2}0)$ symmetry.

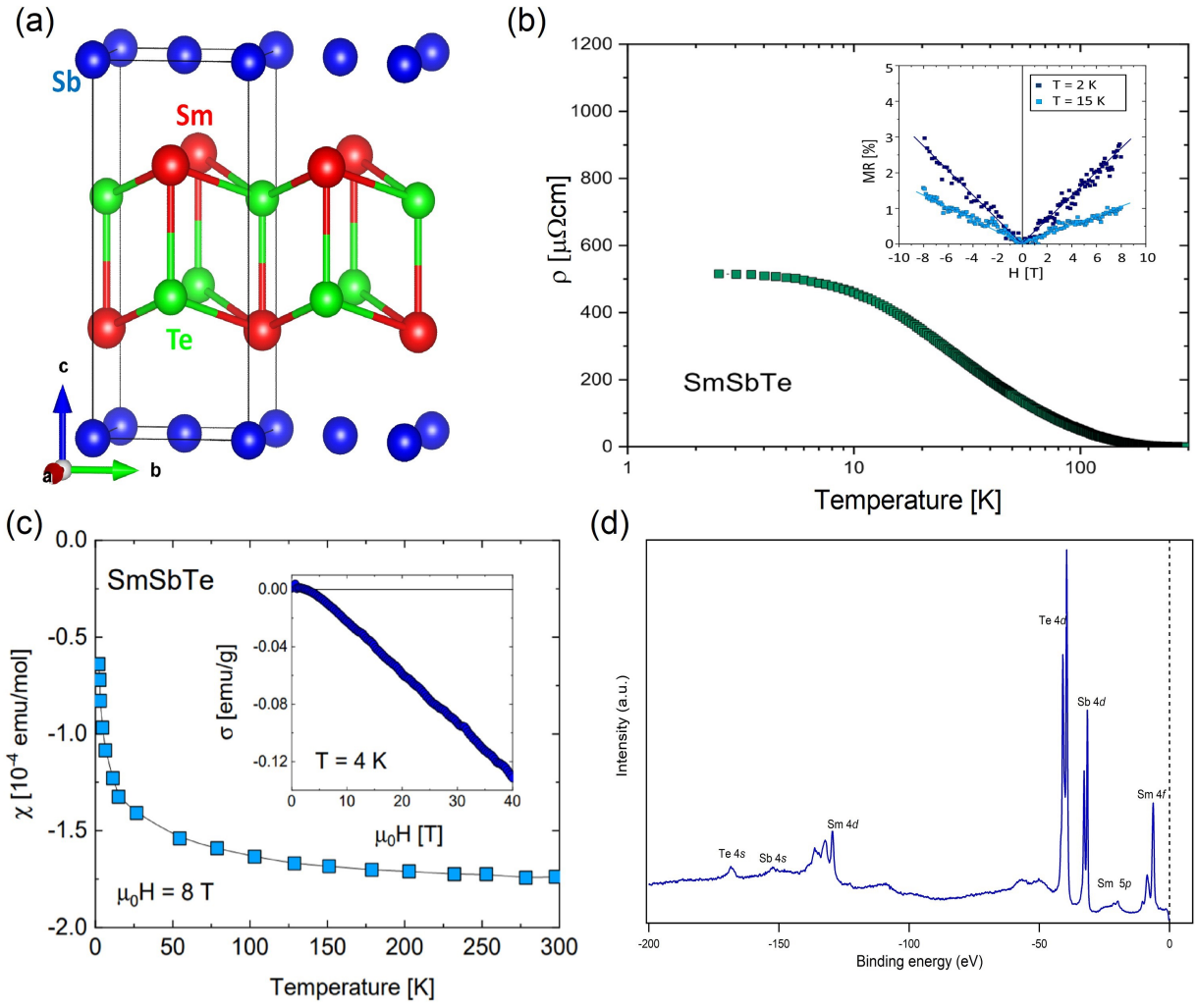


Figure 4.1: Crystal structure and transport measurements. (a) Crystal structure of $\mathrm{SmSbTe}$, where red, blue, and green spheres represent $\mathrm{Sm}$, $\mathrm{Sb}$, and $\mathrm{Te}$ atoms, respectively. (b) Temperature dependence of resistivity. Inset shows field dependence of magnetoresistance. (c) Magnetic susceptibility measured with a field of 8 T as a function of temperature. Inset shows magnetization measured as a function of magnetic field at a temperature of 4 K. (d) Spectroscopic core level spectrum measured on single-crystal of $\mathrm{SmSbTe}$ with a photon source of energy 450 eV.

The electrical transport measurement (figure 4.1(b) show that the electrical resistivity rises with decreasing temperature. Below $\sim 8\ \mathrm{K}$, the resistivity tends to saturate, a feature which has been observed in systems with Dirac surface states when the metallic conduction from the surface state dominates the bulk resistivity [203, 204]. The inset of figure 4.1(b) shows the field dependence

of magnetoresistance ($= \frac{\rho(H)-\rho(0)}{\rho(0)} \times 100\%$), where a linear behavior can be observed indicating possible linear dispersion in the low-temperature electronic band structure. The magnetic measurements are typical of a weak diamagnet with negative magnetic susceptibility that is almost field independent (figure 4.1(c)) and negative slope of magnetization measured as a function of temperature (figure 4.1(c) inset). The core level spectrum (figure 4.1(d)) measured using photon source of 750 eV depicts peaks associated with orbitals of $\mathrm{Sm}$ ($4f$, $5p$, $4s$), $\mathrm{Sb}$ ($4d$, $4s$), and $\mathrm{Te}$ ($4d$, $4s$) indicating a good quality of the single crystals utilized for our measurements.

#### *4.2.1.2 Theoretical prediction of multiple nodal-lines*

With weak van der Waals interactions among the quintuple layers, the $(001)$ is the favorable cleaving plane for $\mathrm{SmSbTe}$. In figure 4.2(a), we present a bulk BZ with high-symmetry points and directions marked on it and its projection onto the 2D (001) surface. Figure 4.2(b) presents bulk band calculations along various high-symmetry directions without and with the consideration of SOC. When SOC is not taken into account, the electronic band structure of $\mathrm{SmSbTe}$ features several nodal-lines along different high-symmetry directions (encircled in blue and red in figure 4.2(b)). These nodal-lines lie along the corresponding red and blue planes shown in schematic in figure 4.2(c). When SOC is taken into account, the nodal-lines encircled in blue gap out. Similar gap opening occurs in recently reported electronic structure measurements in $\mathrm{HoSbTe}$ [201]. Interestingly, the nodal-lines encircled in the red circles remain gapless even when SOC is considered. In addition to the nodal-lines, there exists a band inversion between $\mathrm{Sm}$ $d$ and $\mathrm{Sb}$ $p$ bands along bulk high-symmetry direction $\mathrm{Z} - \mathrm{A}$ pointing to potential non-triviality of the system.

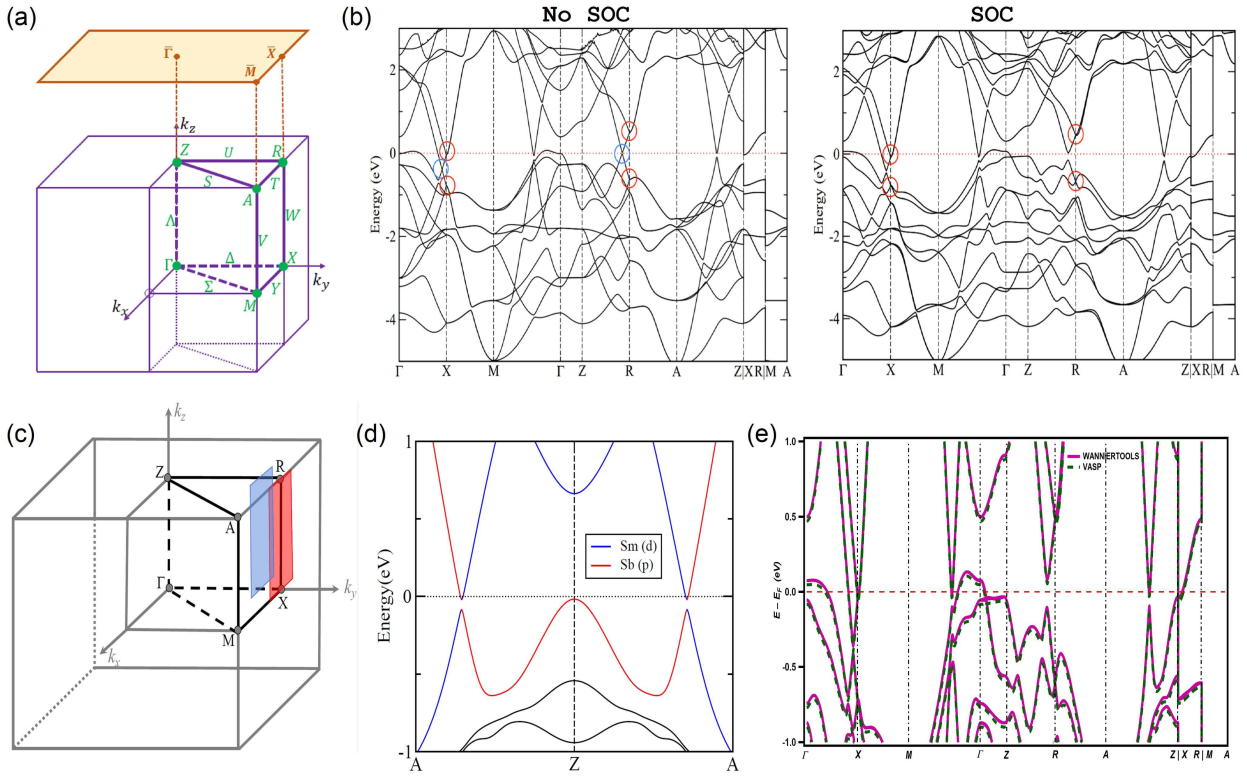


Figure 4.2: Bulk band calculations. (a) 3D and $(001)$ surface projected 2D BZs. High-symmetry points and lines are marked. (b) Bulk band calculations without taking into account the spin-orbit coupling (left) and considering spin-orbit coupling (right). The red and blue circles enclose the crossing points corresponding to various nodal-lines. (c) Bulk BZ and schematic of nodal-line distribution. (d) Band structure along $\mathrm{A}-\mathrm{Z}-\mathrm{A}$ direction. (e) Overlay plot of bulk bands obtained using VASP and WANNIERTOOLS.

#### *4.2.1.3 Fermi surface and evolution of band pockets with binding energy*

In order to investigate the presence of nodal-lines in this system experimentally, we performed ARPES measurements, whose results are presented in figures 4.3 - 4.8. We start with the analysis of the experimental FS and constant energy contours taken at various binding energy as shown in figure 4.3(a). The FS is diamond-shaped, typical of ZrSiS-type systems. Going down the binding energy, a circular pocket begins to appear as seen in constant energy contour at $200$ meV binding

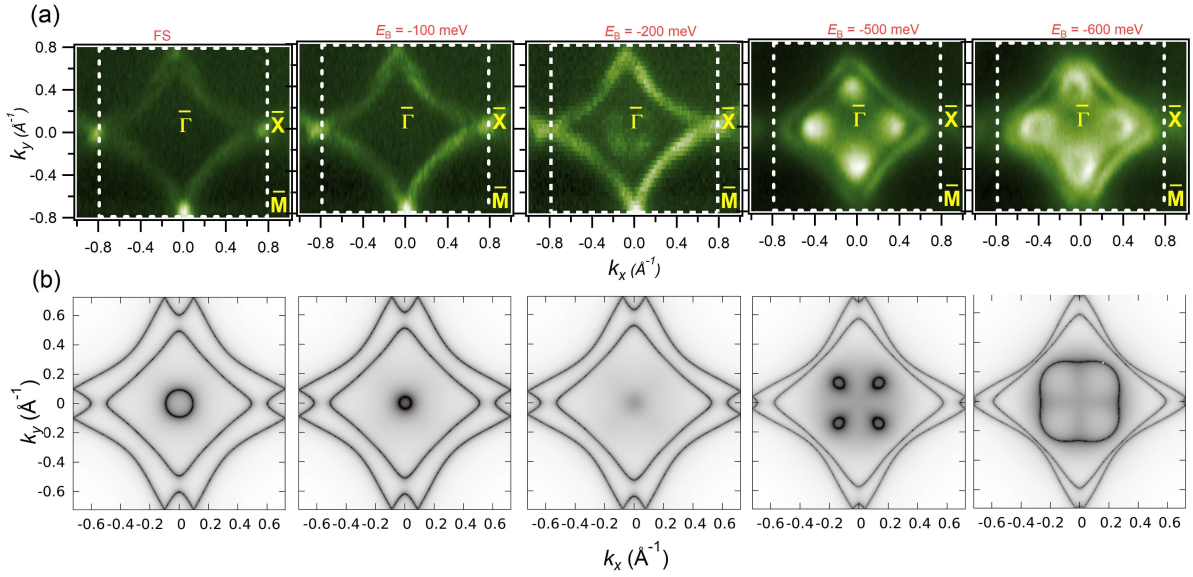


Figure 4.3: Constant energy contours. (a) Fermi surface (leftmost) and constant energy contours at labeled binding energies obtained from the ARPES measurements with a photon energy of 95 eV. (b) Corresponding Fermi surface and energy contours obtained from theoretical calculations.

energy. This pocket shows hole-type nature enlarging with increasing binding energy and finally emerges into an inner diamond pocket at around $500$ meV binding energy. At the corners of this inner diamond, circular pockets emerge and grow with binding energy indicating hole nature. The calculated energy contours at the Fermi level and corresponding binding energies are shown in figure 4.3(b). The diamond pocket at the FS has two-sheet nature in the calculations. This is not obvious in our measurements at the photon energy used for figure 4.3 data ($95$ eV). However, it can be clearly visualized in the FS measured at a lower photon energies. We present data on measurement with a lower photon energy of $35$ eV in figure 4.4. It is clear from the FS map and its second derivative plot (figure 4.4(a)) that the diamond pocket has double sheet nature. A dispersion map along the Cut1 direction represented by white dashed line in figure 4.4(a) is presented in figure 4.4(b). Two bands can clearly be seen crossing the Fermi level supporting the observation of double sheets in the diamond pocket.

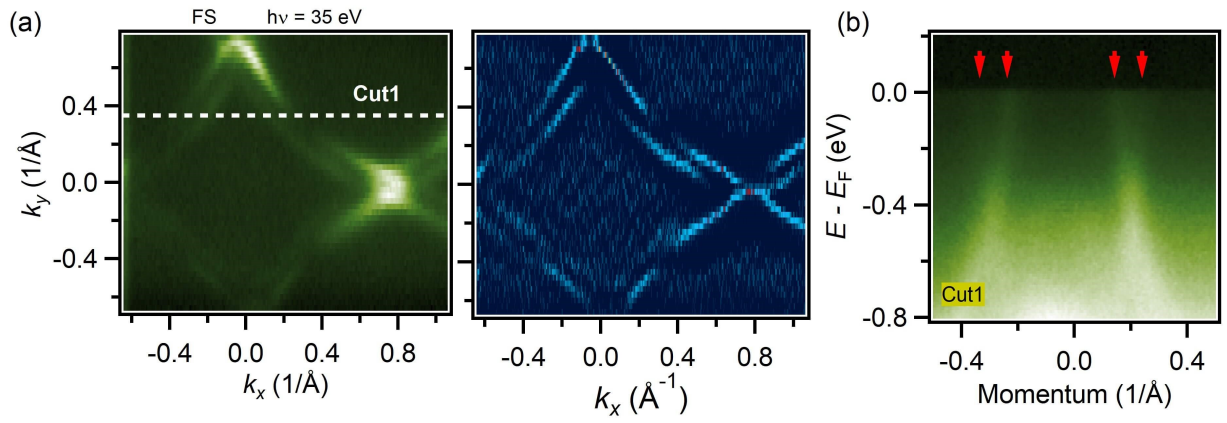


Figure 4.4: Illustration of double sheets in the diamond Fermi pocket. (a) ARPES measured Fermi surface map taken with photon energy of 35 eV (left) and its second derivative (right). (b) Energy-momentum dispersion along the Cut1 direction represented by the dashed line in the Fermi surface in (a).

#### *4.2.1.4 Observation of the surface state*

In figure 4.5, we present the ARPES measured dispersion maps along the $\overline{\mathrm{M}} - \overline{\Gamma} - \overline{\mathrm{M}}$ direction in the SBZ. A Dirac-like dispersion can be observed. The bands associated with the Dirac-like feature do not seem to change their dispersion with varying photon energy indicating the surface nature of this Dirac-like state. Dirac node seems to be around $600\ \mathrm{meV}$ below the Fermi level. Surface state calculation (figure 4.5(h)) matches the experimental band dispersion. However, there is a gap at the $\overline{\mathrm{X}}$ point in the calculation, which can not be well resolved in the experiments. This mismatch might be due to limited resolution of the experimental set up or can also happen due to quantum size effects in slab calculations [45].

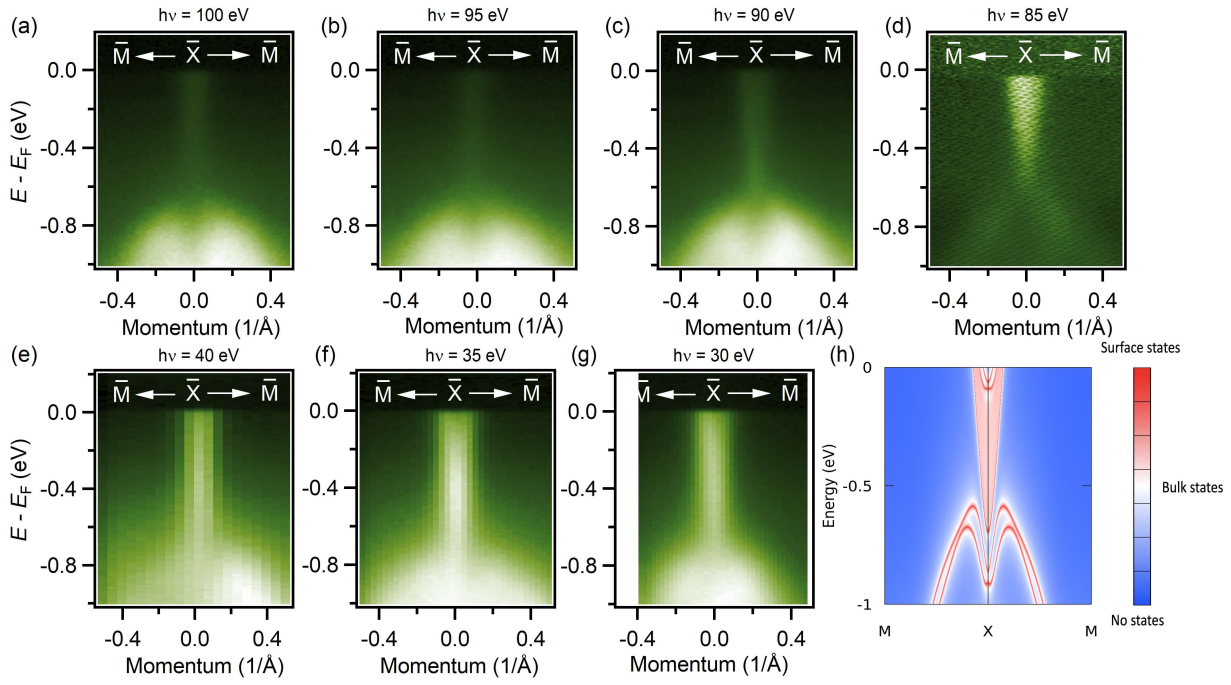


Figure 4.5: Dispersion maps along the $\overline{\mathrm{M}} - \overline{\mathrm{X}} - \overline{\mathrm{M}}$ on the (001) surface of $\mathrm{SmSbTe}$. (a)-(g) Band dispersions along $\overline{\mathrm{M}} - \overline{\mathrm{X}} - \overline{\mathrm{M}}$ taken with different photon energies noted on top of each plots. (h) Theoretical calculation of the surface band structure along $\overline{\mathrm{M}} - \overline{\mathrm{X}} - \overline{\mathrm{M}}$.

#### *4.2.1.5 Experimental observation of Dirac nodes*

Now, we move on to the analysis of dispersion maps along the $\overline{\mathrm{M}} - \overline{\Gamma} - \overline{\mathrm{M}}$ and $\overline{\mathrm{X}} - \overline{\Gamma} - \overline{\mathrm{X}}$ directions to look for the experimental evidence of the nodal-line physics in $\mathrm{SmSbTe}$ system as predicted by the theoretical calculations. First, from photon energy dependent mapping, we observed the $k_z$ dispersion in the direction parallel to $\overline{\mathrm{X}} - \overline{\Gamma} - \overline{\mathrm{X}}$. The results are presented in figure 4.6. By using an inner potential value of $\mathrm{V}_0 = 23\,\mathrm{eV}$, a fairly periodic $k_z$ dispersion is observed. From these measurements, we were able to locate the photon energy values corresponding to $k_z = 0$ and $k_z = \pi$ planes. In figure 4.7, we present the dispersion maps along the $\overline{\mathrm{M}} - \overline{\Gamma} - \overline{\mathrm{M}}$ direction for $k_z = 0$ (figure 4.7(a), bulk $\mathrm{M} - \Gamma - \mathrm{M}$ direction) and $k_z = \pi$ (figure 4.7(b), bulk $\mathrm{A} - \mathrm{Z} - \mathrm{A}$ direction). An almost linearly dispersing band can be observed crossing the Fermi level. This is the

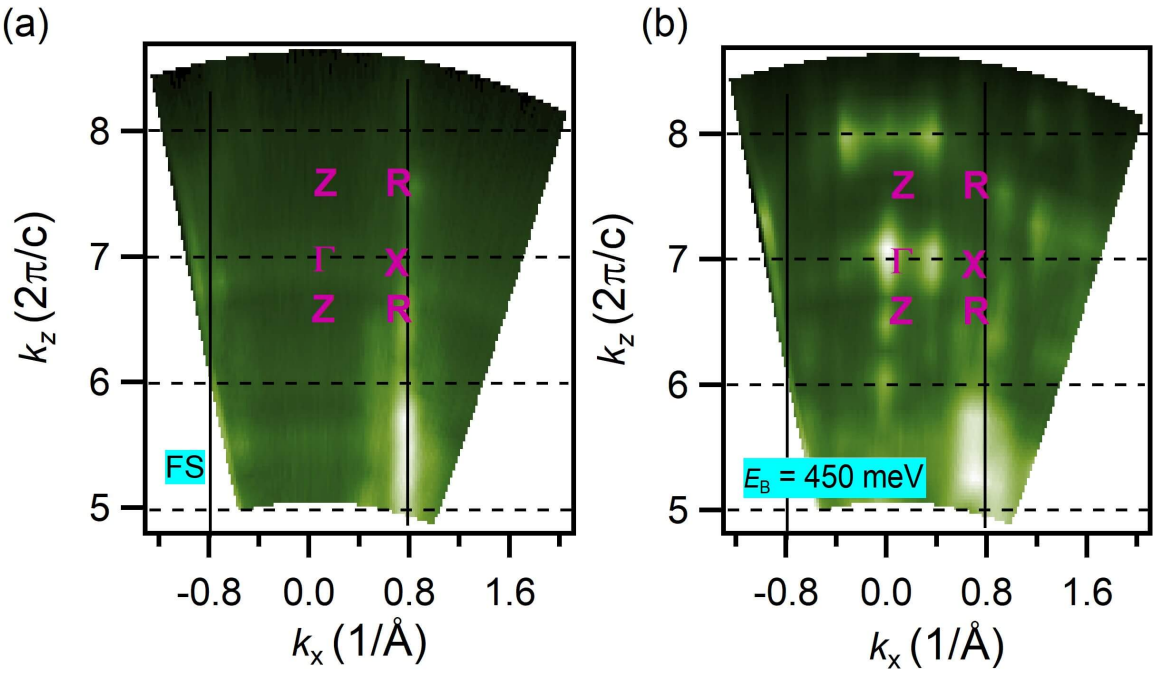


Figure 4.6: $k_x - k_z$ maps. (a) $k_x - k_z$ map taken at the Fermi surface. (b) $k_x - k_z$ map taken at a binding enrgy of 450 meV.

band that gives the diamond shaped Fermi pocket. Theoretical calculation (figure 4.2(b)) predict gapped state along this direction. However, this is not obvious from our measurements. Also, the double sheet nature of the diamond pocket means two bands should be crossing the Fermi level, however this is not resolved in our measurements. This might be due to the limited resolution of the experimental set up.

From the theoretical calculations, Dirac nodes are predicted at the X and R points in the bulk BZ corresponding to the gapless nodal lines that are present even with SOC (figure 4.2(b)). In order to provide experimental evidence of the nodal lines, we analyze the ARPES results along the $\overline{\mathrm{X}} - \overline{\Gamma} - \overline{\mathrm{X}}$ direction for both $k_z = 0$ (figure 4.8(a), bulk direction $\mathrm{X} - \Gamma - \mathrm{X}$) and $k_z = \pi$ (figure 4.8(b), bulk direction $\mathrm{R} - \mathrm{Z} - \mathrm{R}$). The bands near the $\Gamma$ point show different dispersion for different $k_z$ values indicative of the bulk nature of the bands. At the X point, Dirac nodes (shown

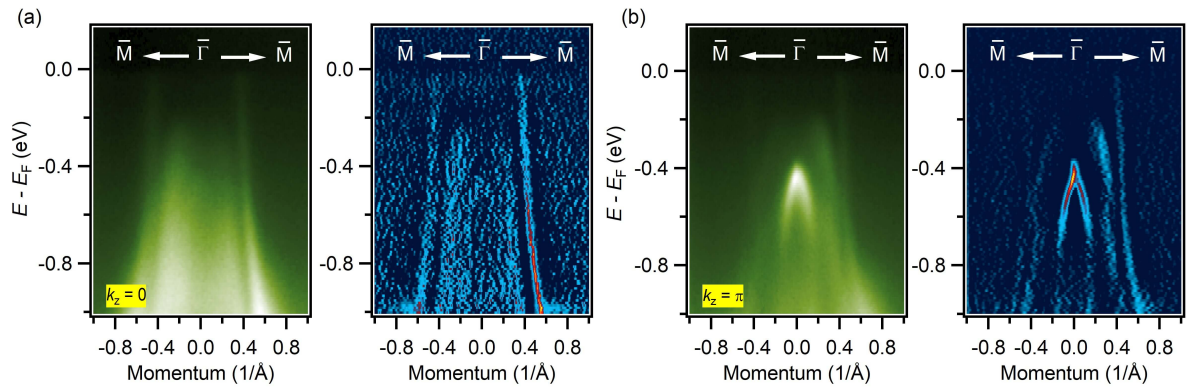


Figure 4.7: Band dispersion along $\overline{\mathrm{M}} - \overline{\Gamma} - \overline{\mathrm{M}}$. (a) ARPES measured band dispersion along $\overline{\mathrm{M}} - \overline{\Gamma} - \overline{\mathrm{M}}$ on the $k_z = 0$ plane (left) and its second derivative plot (right). (b) $\overline{\mathrm{M}} - \overline{\Gamma} - \overline{\mathrm{M}}$ electronic structure measured on the $k_z = \pi$ plane (left) and its second derivative plot (right).

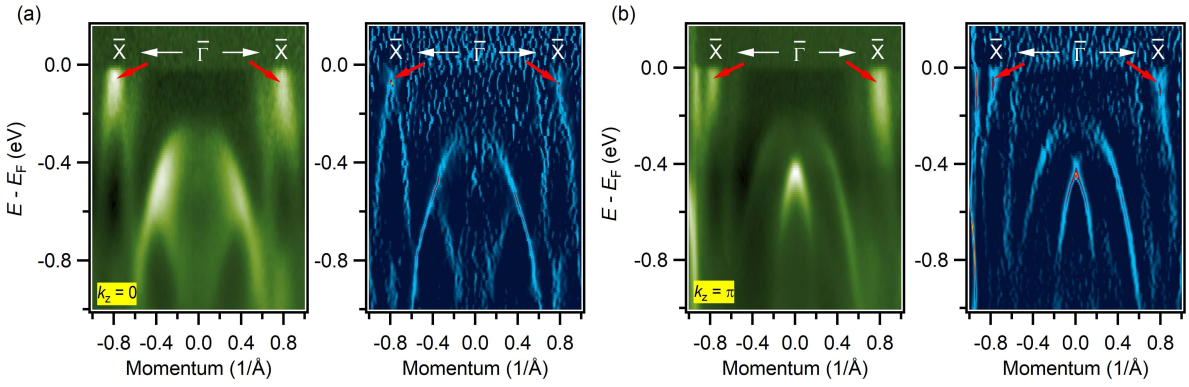


Figure 4.8: Observation of nodal crossing along the $\overline{\mathrm{X}} - \overline{\Gamma} - \overline{\mathrm{X}}$ direction. (a) ARPES measured band dispersion along $\overline{\mathrm{X}} - \overline{\Gamma} - \overline{\mathrm{X}}$ on the $k_z = 0$ plane (left) and its second derivative plot (right). (b) $\overline{\mathrm{X}} - \overline{\Gamma} - \overline{\mathrm{X}}$ electronic structure measured on the $k_z = \pi$ plane (left) and its second derivative plot (right).

by red arrows) can be clearly observed formed by the crossing of two almost linearly dispersing bands. The crossing is located very near the Fermi level. The Dirac nodes exist for both $k_z = 0$ and $k_z = \pi$ planes, which correspond to the theoretically predicted Dirac nodes at the X and R points, providing experimental evidence of the nodal-line.

### *4.2.2 Results on* $\mathrm{NdSbTe}$

#### *4.2.2.1 Crystal structure and bulk characterization*

Similar to $\mathrm{SmSbTe}$, $\mathrm{NdSbTe}$ also crystallizes with tetragonal crystal structure ($P4/mmm,\ \#129$), where $\mathrm{Sb}$ square planes are sandwiched in between $\mathrm{Nd-Te}$ layers (see Figure 4.9(a)). Thermodynamic measurements are presented in Figure 4.9(b) and Figure 4.9(c). Specific heat plotted as a function of temperature ($C(T)$) shows that $\mathrm{NdSbTe}$ has specific heat ($74\ \mathrm{J/mol-K}$) nearly equal to the Dulong-Petit limit ($74.8\ \mathrm{J/mol-K}$). A distinct mean-field-like anomaly corresponding to an antiferromagnetic transition can be observed at around the Neel temperature, $T_{\mathrm{N}} = 2.7\ \mathrm{K}$. The extended tail above the Neel temperature, as depicted in the low-temperature $C/T$ versus $T$ plot in the inset of Figure 4.9(b), can be associated with the short-range exchange interactions. Magnetic property is investigated by means of magnetic susceptibility and magnetization measurements performed with field applied along the crystallographic $c$ axis and the results are shown in Figure 4.9(c). The inverse magnetic susceptibility ($\chi^{-1}(T)$) (measured in applied field of $0.5\ \mathrm{T}$) above $50\ \mathrm{K}$ shows Curie-Weiss behavior with a negative paramagnetic Curie temperature $\theta_{\mathrm{p}} = -17.4(2)\ \mathrm{K}$ (indicative of antiferromagnetic exchange interactions) and an effective magnetic moment, $\mu_{\mathrm{eff}} = 3.57(1)\ \mu_{\mathrm{B}}$. Deviation from the Curie-Weiss behavior is observed below $50\ \mathrm{K}$, possibly because of the crystal field effect. $\chi(T)$ in the upper left inset of Figure 4.9(c) shows a peak at around the Neel temperature $T_{\mathrm{N}} = 2.7\ \mathrm{K}$ indicating a long-range antiferromagnetic ordering. Field dependence of magnetization $\sigma(H)$ measured at a temperature of $1.72\ \mathrm{K}$ is shown in the lower right inset of Figure 4.9(c), which resembles an AFM character. A metamagnetic-like transition can be observed around $2\ \mathrm{T}$, with linear $\sigma(H)$ below this field and a slight convex curvature in $\sigma(H)$ above this field. For $\mu_0 H = 5\ \mathrm{T}$, $\sigma = 14.2(1)\ \mathrm{emu/g}$, a value that corresponds to $1\ \mu_{\mathrm{B}}$ magnetic moment (much smaller than the predicted value for $\mathrm{Nd^{3+}}$ ion, which is $3.27\ \mu_{\mathrm{B}}$). This deviation may be attributed to crystal field effect and single-ion anisotropy. Note that the

results of our thermodynamic measurements are in concert with the previously reports [205, 206].

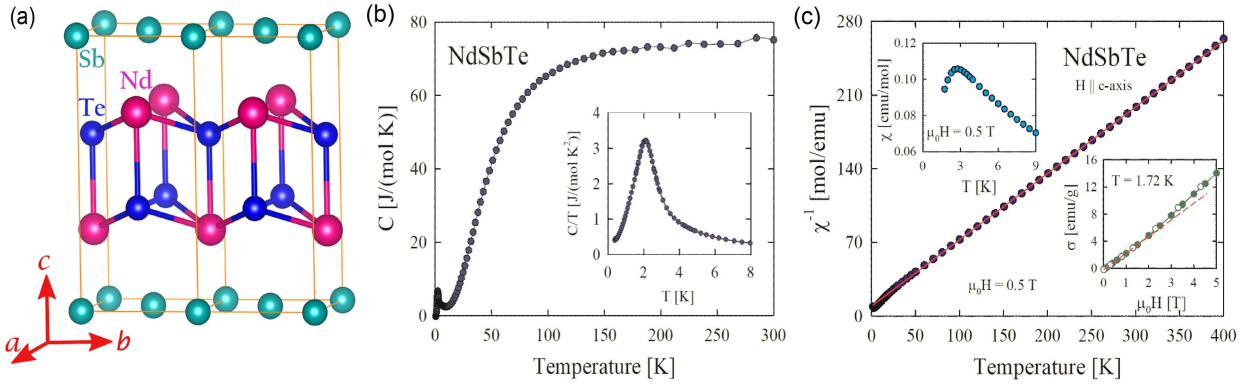


Figure 4.9: Crystal structure and bulk characterization of $\mathrm{NdSbTe}$. (a) Crystal structure of $\mathrm{NdSbTe}$, where cyan, teal, and blue spheres represent $\mathrm{Nd}$, $\mathrm{Sb}$, and $\mathrm{Te}$ atoms, respectively. (b) Temperature dependence of specific heat. Inset shows the low temperature specific heat to temperature ration. (c) Inverse magnetic susceptibility measured with a field of $0.5$ T as a function of temperature. Inset on the top left shows low temperature magnetic susceptibility. Inset on the bottom right shows magnetization measured as a function of magnetic field at a temperature of $1.72$ K. Solid and open symbols represent the data taken with increasing and decreasing field strength, respectively. The dashed line is to show the linear nature of magnetization as a function of field below the metamagnetic transition.

#### *4.2.2.2 Bulk band calculations and prediction of nodal-lines*

The results of DFT-based band structure calculations are presented in Figure 4.10. The optimized lattice parameters used for the calculations, $a = b = 4.371$ Å and $c = 9.457$ Å, are in close agreement with the reported values [207]. The $\mathrm{Nd}$, $\mathrm{Sb}$, and $\mathrm{Te}$ atoms occupy the Wyckoff positions $2c$ $(1/4,1/4,0.2769)$, $2a$ $(3/4,1/4,0)$, and $2c$ $(1/4,1/4,0.6279)$, respectively. Figure 4.10(a) represents a 3D bulk BZ and a $(001)$ surface projected 2D BZ, where high-symmetry points are marked on each of them. The bulk band structure exhibits Dirac nodal-lines along the $\mathrm{X}-\mathrm{R}$ and $\mathrm{M}-\mathrm{A}$ directions because of the $P4/mmm$ symmetry. When the SOC effect is neglected, two distinct gapless nodal-lines lie along the $\mathrm{X}-\mathrm{R}$ and another one away from the $\mathrm{X}-\mathrm{R}$ direction formed by the

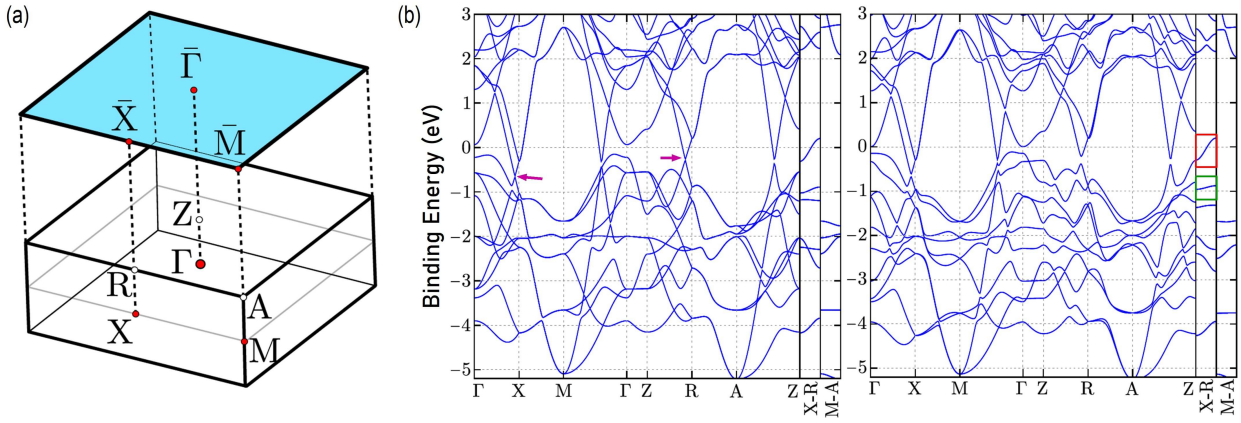


Figure 4.10: Bulk band calculations. (a) 3D and $(001)$ surface projected 2D BZs. High-symmetry points marked. (b) Bulk band calculations without taking into account the SOC (left) and considering SOC (right).

Dirac crossings shown by the arrows (see Figure 4.10(b) left panel) within $\pm 1$ eV binding energy window. As seen in Figure 4.10(b) right panel, the nodal-line lying away from the $\mathrm{X} - \mathrm{R}$ direction gaps out with the inclusion of SOC, however, the ones along the $\mathrm{X} - \mathrm{R}$ direction remain gapless (enclosed in red and green boxes). The nodal-line enclosed in red box disperses from below the Fermi level at the $\mathrm{X}$ point to above the Fermi level at the $\mathrm{R}$ point. The other nodal-line enclosed in green box, however, seems almost non-dispersive along the $\mathrm{X} - \mathrm{R}$ direction. The band structure along the $\Gamma - \mathrm{M}$ direction, however, seems to be gapped.

#### *4.2.2.3 Experimental and theoretical Fermi surfaces and constant energy contours*

Typical of $\mathrm{ZrSiS}$-type materials, the FS of $\mathrm{NdSbTe}$ features a diamond-shaped pocket centered at the center of the SBZ (see Figure 4.11(a)). The diamond has two sheets as predicted in the theoretical FS, however, the outer sheet is strongly suppressed in intensity compared to the inner one. These sheets seem to merge towards each other creating a single sheet diamond at around $-300$ meV binding energy. A central pocket begins to appear at this binding energy which evolves

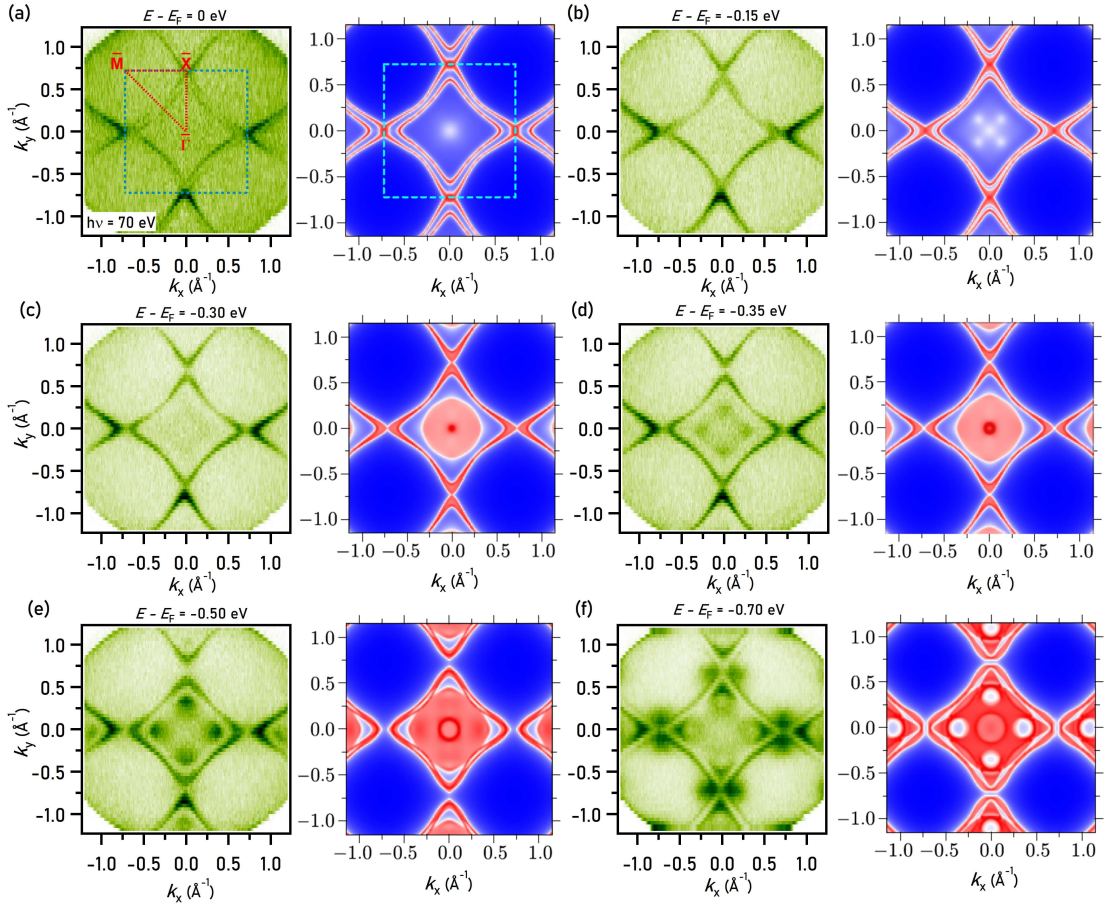


Figure 4.11: Experimental and computed constant energy contours. (a) Experimental FS measured with photon energy of $70$ eV (left) and theoretical FS (right). (b)-(f) Experimental (left panels) and theoretical (right) constant energy contours taken at different binding energies as noted on top of each experimental panels.

into a distinct diamond shape at around $-350$ meV binding energy with extra pockets at its corners. More features apperar in the energy contours at higher binding energies. The calculated results overall show good resemblance with the experimental ones. A intense circular pocket emerges at higher binding energies in the calculations, however, seem to be absent in the experimental data, which is taken with a photon energy of $70$ eV. Polarization dependent measurements performed with photon energy of $60$ eV (Figure 4.12) show that this pocket is actually sensitive to linear vertical (LV) polarization, hence explaining its absence in the experimental data with linear

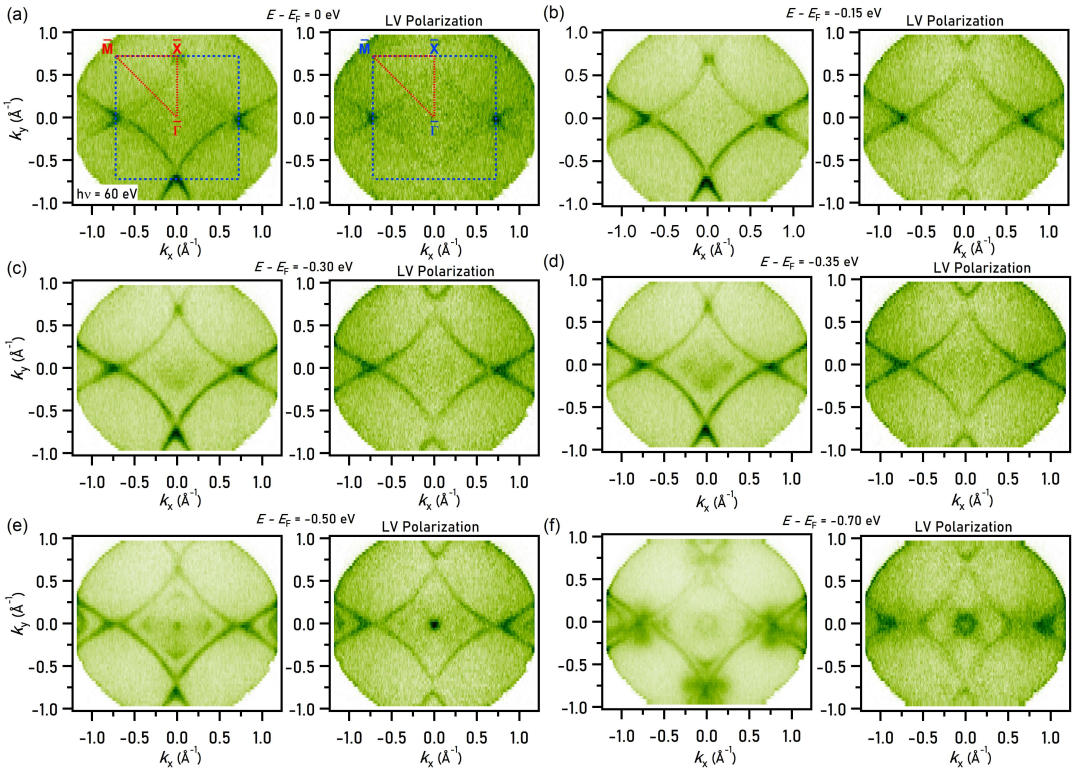


Figure 4.12: Polarization dependent constant energy contours. (a) Experimental FS measured with linear horizontal (left) and linear vertical (right) polarized photon beam of energy $60$ eV. (b)-(f) Constant energy contours at various binding energies measured with linear horizontal (left panels) and linear vertical (right panels) light.

horizontal (LH) polarization in Figures 4.11 and 4.12. The polarization dependent data also shows that the outer sheet in the FS diamond is also sensitive to the LV polarization and is, therefore, strongly suppressed in intensity in experimental data with LH polarization. In addition, the pockets that appear at high binding energies ($-700$ meV) around the $\overline{\mathrm{X}}$ point show sensitivity to LH polarization.

*4.2.2.4 Multiple gapless-nodal lines*

Next, we turn our attention towards exploring the experimental evidence for the presence of nodal-lines as predicted from the theoretical bulk band structure calculations. First, we analyze the dispersion maps along $\overline{\mathrm{M}} - \overline{\Gamma} - \overline{\mathrm{M}}$. With $60\ \mathrm{eV}$ LH polarized photon source, a single band seems to be crossing the Fermi level. This band is very steep with band velocity measured within binding energy window of $0\ \mathrm{mev}, -360\ \mathrm{meV}$ around $11.43 \pm 0.89\ \mathrm{eV\AA}$. This value is very large compared to the band velocity reported for $\overline{\Gamma} - \overline{\mathrm{M}}$ bands in $\mathrm{ZrSiS}$ [208]. Note that the value of band velocity is extracted from the linear fitting of the peak positions in the momentum distribution curves (see Figure 4.13(a)). Knowing the sensitivity of the diamond sheets to polarization of light, we took a dispersion map along the $\overline{\mathrm{M}} - \overline{\Gamma} - \overline{\mathrm{M}}$ direction with $60\ \mathrm{eV}$ LV polarized light. The result is presented in Figure 4.13(b). We again observe a single steep band crossing the Fermi level, however, this band seems to diverge slightly away from the $\overline{\Gamma}$ point, which is different from the band observed for LH polarization that seems to be converging slightly towards $\overline{\Gamma}$. To understand the actual experimental dispersion along $\overline{\mathrm{M}} - \overline{\Gamma} - \overline{\mathrm{M}}$, we added the matrices for LH and LV polarization together. The result is the presence of a linear crossing between two bands around $-300\ \mathrm{meV}$ binding energy as shown in Figure 4.13(c). The crossing is clearly depicted in the second derivative plot in Figure 4.13(d). This is suggestive of a gapless nodal-line across the $\overline{\Gamma} - \overline{\mathrm{M}}$, although the bulk band calculation predicts a gapped state. The band spectrum along this direction calculated for $(001)$ surface seems to reproduce our observation of almost gapless bandcrossing feature (Figure 4.13(e)). A point to note here is that the calculated spectrum in Figure 4.13(e) is projected for all $k_z$ values. The $k_z$ dependent bulk band calculation (Figure 4.13(f)) shows that for a single value of $k_z$, the band structure is gapped along this direction. This suggests that the observation of gapless nodal-line across the $\overline{\Gamma} - \overline{\mathrm{M}}$ direction is likely due to poor $k_z$ resolution in VUV ARPES.

Next, we analyze the band structure along $\overline{\mathrm{X}} - \overline{\Gamma} - \overline{\mathrm{X}}$ at different photon energies to explore the

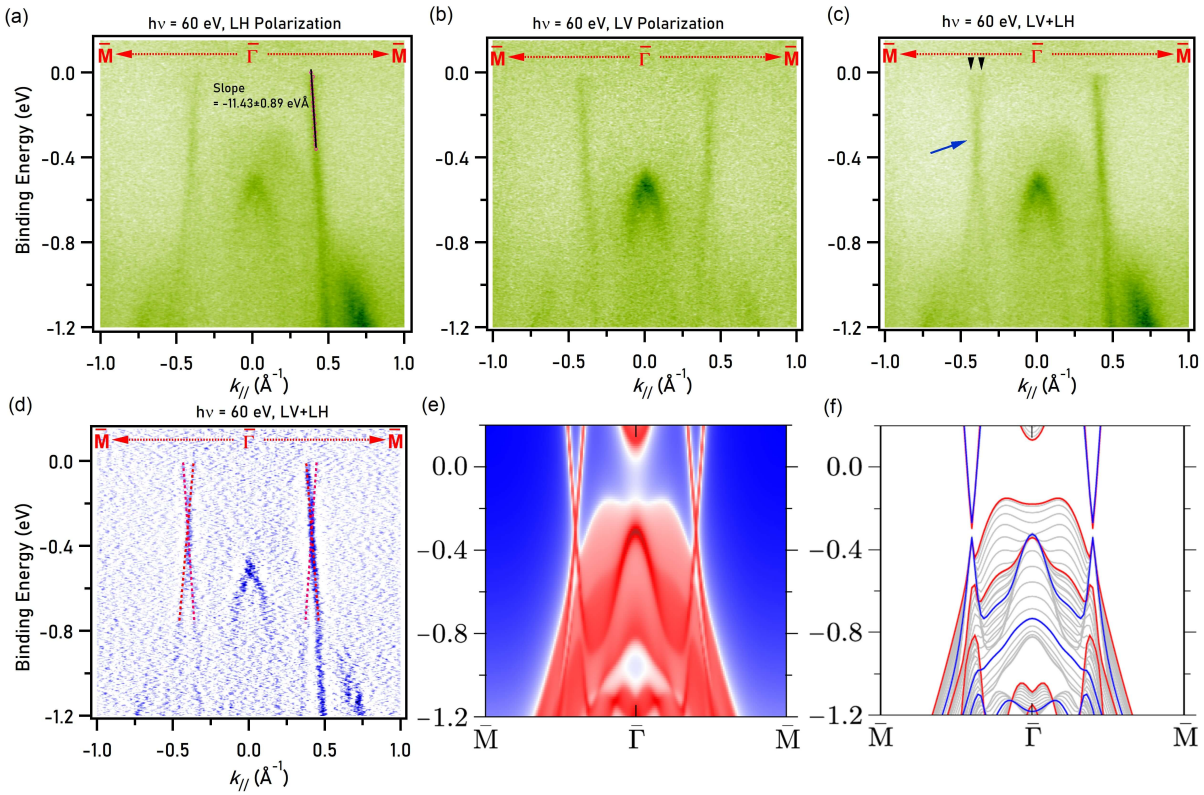


Figure 4.13: Band structure along the $\overline{\mathrm{M}}-\overline{\Gamma}-\overline{\mathrm{M}}$ direction. (a) Experimental band structure along $\overline{\mathrm{M}}-\overline{\Gamma}-\overline{\mathrm{M}}$ measured with linear horizontal polarized light with energy $60$ eV. (b) Band structure along $\overline{\mathrm{M}}-\overline{\Gamma}-\overline{\mathrm{M}}$ measured with linear horizontal polarized light with energy $60$ eV. (c) $\overline{\mathrm{M}}-\overline{\Gamma}-\overline{\mathrm{M}}$ dispersion map with the matrices in (a) and (b) added together. (d)Second derivative plot of (c). (e) Calculated surface projected band structure along $\overline{\mathrm{M}}-\overline{\Gamma}-\overline{\mathrm{M}}$. (f) $k_z$ dependent calculated bulk bands along $\overline{\mathrm{M}}-\overline{\Gamma}-\overline{\mathrm{M}}$.

possible presence of predicted nodal-lines along the $\mathrm{X}-\mathrm{R}$ direction. Figure 4.14(a) shows an experimental dispersion map along this direction measured using a photon energy of $90$ eV. A linearly dispersing hole band seem to crossing the Fermi level potentially forming a Dirac crossing slight away from the Fermi level (green dashed line). Around $760$ meV below the Fermi level, a linear band crossing seems to occur between an electron band extending down from above the Fermi level and a W-shaped band. In Figure 4.14(b), we present photon energy dependent dispersion maps along $\overline{\mathrm{X}}-\overline{\Gamma}-\overline{\mathrm{X}}$ from $70$ EV ($k_z \sim \pi$) to $56$ eV ($k_z \sim 0$). The linear band crosses

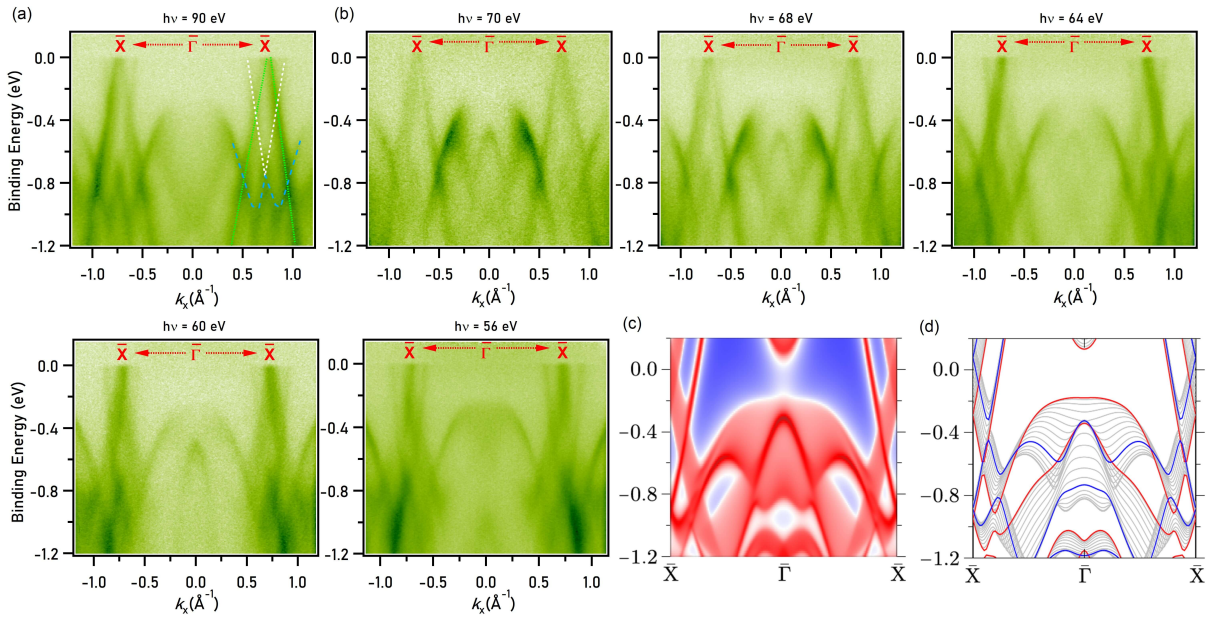


Figure 4.14: Band structure along the $\overline{\mathrm{X}} - \overline{\Gamma} - \overline{\mathrm{X}}$ direction. (a) Experimental band structure along $\overline{\mathrm{X}}-\overline{\Gamma}-\overline{\mathrm{X}}$ measured with photon energy of $90$ eV. (b) Band structure along $\overline{\mathrm{X}}-\overline{\Gamma}-\overline{\mathrm{X}}$ measured with different photon energies as noted on top of each plot. (c) Calculated surface projected $\overline{\mathrm{X}} - \overline{\Gamma} - \overline{\mathrm{X}}$ band structure. (f) $k_z$ dependent calculated bulk bands along $\overline{\mathrm{X}} - \overline{\Gamma} - \overline{\mathrm{X}}$.

the Fermi level with likely Dirac crossing above the Fermi level at $70$ eV. The crossing seems to get pushed down lower and below the Fermi level in reducing the photon energy down to $56$ eV. This is consistent with the dispersive gapless nodal-line around the Fermi level along $\mathrm{X} - \mathrm{R}$ in calculated bulk band structure. The band crossing around $-760$ meV binding energy seems to have very little dispersion in the energy axis, consistent with the almost dispersionless nodal-line along $\mathrm{X}-\mathrm{R}$ in calculated bulk band structure. The surface spectrum calculated along this direction (Figure 4.14(c)) well reproduces the experimental observations. The $k_z$ dependent calculated bulk band structure in Figure 4.14(d) supports the disversive and almost dispersionless nature of the nodal-lines in the vicinity of Fermi level and around $-800$ meV binding energy, respectively.

*4.2.2.5 Observation of the surface state*

In Figure 4.15, we present the dispersion maps along the $\overline{\mathrm{M}} - \overline{\mathrm{X}} - \overline{\mathrm{M}}$ direction. A gapped Dirac-like state is observed in the experimental measurements at the $\overline{\mathrm{X}}$ point of the SBZ. Photon-energy dependent measurements show that this state is insensitive to photon energy variation indicative of its surface origination. The comparison of the LH and LV polarized $60\ \mathrm{eV}$ experimental data presented in Figures 4.15(d) and Figure 4.15(e), respectively indicate the sensitivity of the surface bands to LH polarization. The experimental results and their comparison with the calculated surface spectrum (Figure 4.15(f)) show that this surface state co-exists with bulk bands.

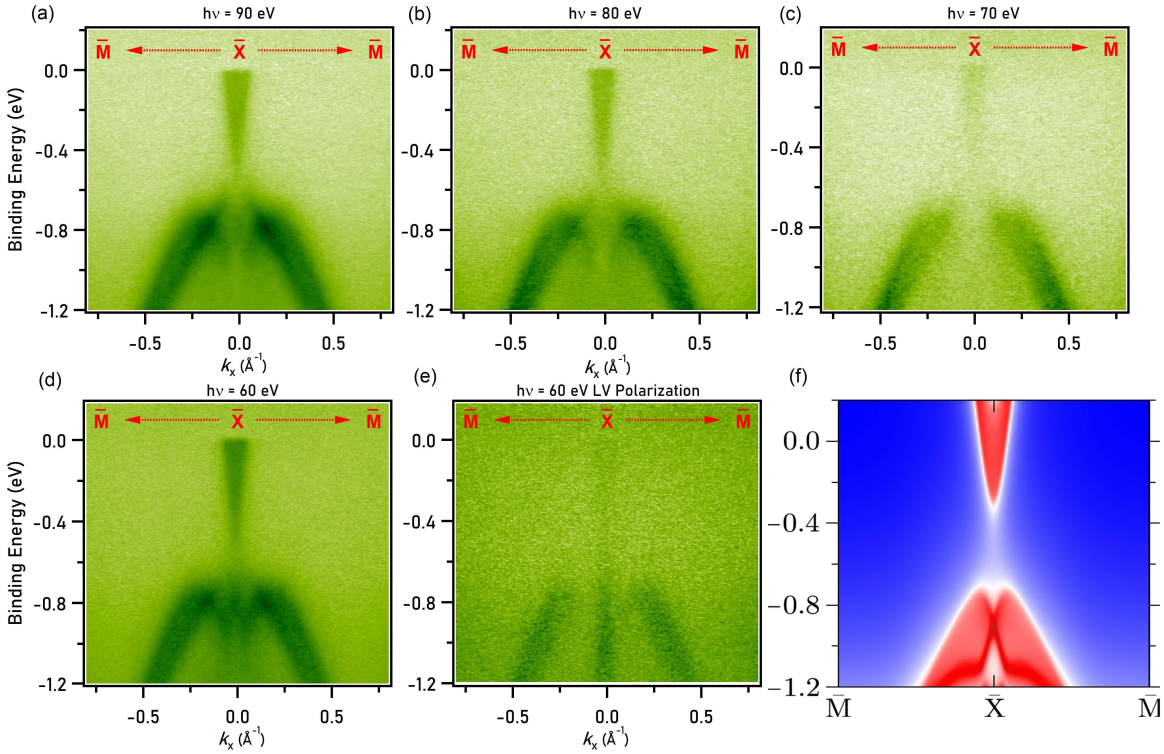


Figure 4.15: Band structure along the $\overline{\mathrm{M}} - \overline{\mathrm{X}} - \overline{\mathrm{M}}$ direction. (a)-(d) Experimental band structure along $\overline{\mathrm{M}} - \overline{\mathrm{X}} - \overline{\mathrm{M}}$ measured with different photon energies as noted on top of each plot. (e) Band structure along $\overline{\mathrm{M}} - \overline{\mathrm{X}} - \overline{\mathrm{M}}$ measured with linear vertical polarized photon beam with energy $60\ \mathrm{eV}$. (f) Calculated surface projected $\overline{\mathrm{M}} - \overline{\mathrm{X}} - \overline{\mathrm{M}}$ band structure.

## 4.3 Conclusion

To conclude, via ARPES measurements supported by first-principles calculations, we carried out a detailed study of the $\mathrm{SmSbTe}$ and $\mathrm{NdSbTe}$ electronic structure. Typical of $\mathrm{ZrSiS}-\mathrm{type}$ materials, these systems also feature diamond-shaped Fermi surface. Surface states are observed at the $\overline{\mathrm{X}}$ point of the SBZ. In the absence of SOC, calculations predict multiple nodal-lines in these systems, some of which gap out with inclusion of SOC and some remain gapless (along $\mathrm{X}-\mathrm{R}$ direction). In line with the predictions from calculations, we observed Dirac nodes very near to the Fermi level at the bulk $\mathrm{X}$ and $\mathrm{R}$ points that correspond to the gapless nodal line in $\mathrm{SmSbTe}$. We also observed two gapless nodal lines in $\mathrm{NdSbTe}$ along the bulk $\mathrm{X}-\mathrm{R}$ direction as well as one across the $\Gamma-\mathrm{M}$ directions formed by high velocity bands that are sensitive to polarization of incident light. This study on $Ln$-based $\mathrm{ZrSiS}-\mathrm{type}$ materials provides platforms to further explore the electronic structure evolution within the $Ln\mathrm{SbTe}$ family.

## 4.4 Experimental and computational methods

### *4.4.1 Crystal growth and characterization*

*SmSbTe:* High-quality single crystals of $\mathrm{SmSbTe}$ were grown by using the flux method [168]. The chemical composition and crystal structure of the samples were characterized by using energy-dispersive X-ray spectroscopy and powder X-ray diffraction measurements, respectively. For energy-dispersive X-ray spectroscopic measurements, FEI scanning electron microscope equipped with an EDAX Genesis XM4 spectrometer was utilized. $\mathrm{Cu\ K}\alpha$ radiation was used for the powder X-ray diffraction measurements, and the measurements were carried out on a Kuma-Diffraction KM4 four-circle X-ray diffractometer with CCD camera was utilized.

*NdSbTe:* First the polycrystals were obtained by heating $1:1:1$ ratio of purity $\mathrm{Nd}$, $\mathrm{Sb}$, and $\mathrm{Te}$ sealed inside a evacuated quartz tube upto $1000\ ^{\circ}\mathrm{C}$, keeping at the same temperature for $7\ \mathrm{days}$, and then allowed to cool quickly to ambient temperature. The single crystals of $\mathrm{NdSbTe}$ were, then, synthesized from these polycrystals using the chemical vapor transport method. The chemical composition and crystal structure were characterized by energy-dispersive X-ray analysis carried out by using a FEI scanning electron microscope equipped with an EDAX Genesis XM4 spectrometer and Oxford Diffraction X'calibur four-circle single-crystal X-ray diffractometer equipped with a CCD Atlas detector, respectively.

### *4.4.2 Electric, magnetic transport, and thermodynamic measurements*

*Electric and magnetic transport measurements on SmSbTe:* Quantum Design DynaCool-14 System was used for the resistivity, magnetoresistance, and magnetic susceptibility measurements. The measurements were performed with magnetic field up to $14\ \mathrm{T}$ and within temperature range of $2-300\ \mathrm{K}$. Standard four-probe resistivity measurements were carried out on single-crystals of $\mathrm{SmSbTe}$ by attaching four platinum wires using silver paste. Pickup-coil technique at the National High Magnetic Field Laboratory, Los Alamos was used for the magnetization measurements, which were carried out in pulsed magnetic fields upto $40\ \mathrm{T}$.

*Measurements of thermodynamic properties of NdSbTe:* The heat capacity of $\mathrm{NdSbTe}$ bulk crystals were measured in a Quantum Design PPMS-9 platform with a $^{3}\mathrm{He}$ refrigerator by employing relaxation technique and $\mathrm{two}-\tau$ model. Measurements were carried out within the temperature range of $0.37\ \mathrm{K}-300\ \mathrm{K}$. Magnetic susceptibility and magnetization measurements were carried out within a temperature range of $1.72\ \mathrm{K}-400\ \mathrm{K}$ by employing a Quantum Design MPMS-5 superconducting quantum interference device (SQUID) magnetometer. Magnetic fields upto $5\ \mathrm{T}$ was applied during the measurements.

### *4.4.3 First-principles calculations*

*SmSbTe:* DFT [169, 170]-based calculations were done using VASP [173, 174] with PAW pseudopotential [171, 172] and GGA approximation of PBE type to account for exchange-correlation potential [175]. Calculations did not take into account any magnetic ordering. $\mathrm{Sm}\ 4f$ electrons were treated as core electrons. Hubbard potential $U = 2$ was chosen (to best match the experimental data) for $\mathrm{Sm}\ 5d$ orbitals within the GGA+U approach [176]. The surface state calculations on the $\mathrm{Te}$ terminated $(001)$ surface were done based on Green's function method [209]. DFT calculation results were used as input to construct the tight-binding Hamiltonians from maximally localized Wannier functions [177] using WAANIER90 [210]. The WANNIERTOOLS package [178] was utilized to calculate the surface band structures using Wannier interpolation. Fermi level was shifted by $600\ \mathrm{meV}$ to account for the highly doped nature of the crystals.

*NdSbTe:* DFT [169, 170]-based calculations for $\mathrm{NdSbTe}$ were implemented in VASP [173, 174], while using PAW potential [171] and GGA approximation of PBE-type [175]. The lattice constant and atomic positions were optimized using $15 \times 15 \times 7\ \mathrm{k} - \mathrm{grid}$ in the Monkhorst-Pack scheme [211]. Antiferromagnetic ordering was assumed during the optimization. Within the DFT+U scheme by Liechtenstein *et al.* [212], the $\mathrm{Nd}\ 4f$ states were treated treated with core states using $U = 4\ \mathrm{eV}$ and $J = 0.5\ \mathrm{eV}$. We also carried out band structure calculation within QUANTUM ESPRESSO [213, 214, 215] with PSLIBRARY [216]. DFT calculation results were used as input to construct the tight-binding Hamiltonians from maximally localized Wannier functions [177, 217, 218] using WAANIER90 software [210]. The WANNIERTOOLS package [178] was utilized to investigate surface Green's function for a semi-infinite system [209] by using the so constructed 22-model tight-binding model.

### *4.4.4 ARPES measurements*

ARPES measurements were performed using the synchrotron light source available at the SIS-HRPES end station of the Swiss Light Source. The angular and energy resolutions were set better than $0.2^{\circ}$ and $20\ \mathrm{meV}$, respectively for the ARPES measurements. Flat samples prepared on copper posts, with ceramic post mounted on top using silver epoxy, were loaded into the ARPES chamber maintained at ultra-high vacuum better than $10^{-10}$ torr and then cleaved in-situ. Experiments were conducted at a temperature of $20\ \mathrm{K}$.

# CHAPTER 5: SPECTROSCOPIC EVIDENCE OF FLAT BANDS IN A VAN DER WAALS SEMICONDUCTOR WITH BREATHING KAGOME LATTICE

The results of this work are accepted for publication in Communications Materials (preprint available at *arXiv:2203.10547*)

Quantum materials with kagome lattices have recently been under a great deal of research interest as they can be hosts to several parameters on interest such as geometrical frustation, topology, electronic correlation, and magnetic ordering. In this work, we investigate the electronic band structure in a van der Waals semiconductor with a breathing kagome lattice in the family $\mathrm{Nb}_3X_8$ ($X=$ halogen element), which is different than the usual lattice with six equivalent triangles and features alternate triangles of different sizes. By means of ARPES and collaborative first-principles computations, we provide evidence of the presence of flat and weakly dispersing bands. We also study the sensitivity of these bands to the polarization of incident beam and provide a theoretical evidence of them coming from the breathing kagome plane of $\mathrm{Nb}$ atoms through orbital-resolved calculations. Overall, this work gives an understanding of flat band structure in breathing kagome system, which is easily exfoliable and possesses a moderate semiconducting band gap.

## 5.1 Introduction

The attraction of researchers towards the quantum materials possessing kagome lattice has been increasing in recent times as these quantum materials can provide fertile grounds to study the interaction among parameters such as geometry, correlation, topology, and even magnetic ordering

in most cases [90, 97, 219, 220, 221, 222, 223, 224, 225, 226, 227, 228, 229, 230, 231, 232, 233]. A kagome lattice is comprised of six triangles that share the corner, and the bases of the triangles form a hexagon within which the electronic states are localized. Because of this geometry enforced localization of the electronic states, the electronic structure of the kagome systems may feature flat bands [90, 91, 92, 93, 94], which bring electronic correlations into play. In addition, a Dirac crossing is expected at the corner of the BZ [90, 91, 92, 93, 94, 95], which brings topology into play. Introduction of SOC and magnetic order can gap out this Dirac crossing introducing Chern quantum phases [96, 97, 234, 235]. Different from the usual kagome geometry of six equivalent triangles, some kagome systems possess a different geometry - called the breathing kagome geometry - where triangles of two different sizes alternate each other. The difference in bond lengths in alternate triangles may give rise to local dipole moment and hence a ferroelectric order [236]. With the geometrical perturbation from usual to the breathing kagome lattice, the topological flat bands may remain robust, however, the Dirac crossing at the corner of the BZ may be gapped opening up a possibility of higher-order topology [98, 100, 101].

The flat bands and/or Dirac fermions have been shown to exist in the electronic structure of kagome materials such as $\mathrm{Fe_3Sn_2}$ [90, 96, 237], $\mathrm{CoSn}$ [91, 92], $\mathrm{FeSn}$ [93], $R(\mathrm{Mn/V})_6\mathrm{Sn}_6$ ($R = \mathrm{rare-earth\ elements}$) [94, 97, 238, 239, 240] by utilizing the state-of-the-art ARPES technique. These materials are metallic with most of them having the usual kagome lattice, although Ref. [237] considers breathing kagome lattice in $\mathrm{Fe_3Sn_2}$ suggesting a potential magnetic WSM phase. $\mathrm{Nb_3}X_8$ ($X$= halogen)-type materials not only provide the platforms to explore the electronic structure in breathing kagome materials, but also are semiconducting with a moderate band gap that are meachanically exfoliable to ultra-thin limit [241, 242, 243, 244, 245]. In addition, the predicted ferromagnetism in the monolayer limit [242, 246, 247] makes them even more attractive as platforms to study the potential interaction of geometry, correlation, and magnetic ordering in a single family of materials. However, experimental probe of the electronic structure in these

materials has been lacking.

In this work, we have carried out an ARPES study of the electronic structure in the van der Waal breathing kagome semiconductor $\mathrm{Nb_3I_8}$, which is supported by DFT computations. The semiconducting nature of the material is reflected in the experimental electronic structure, which shows flat and weakly dispersing bands lying around $500\ \mathrm{meV}$ and below $1\ \mathrm{eV}$ binding energies. Results of the DFT computations qualitatively reproduce the experimental electronic structure and show that the flat and weakly dispersing bands are arising from the breathing kagome plane of $\mathrm{Nb}$ atoms. Moreover, the polarization dependent ARPES data show that these bands are sensitive to the polarization of the incident photon beam. This work puts forward an easily exfoliable semiconducting material platform with predicted magnetic monolayer to investigate the interplay among electronic correlation effects, magnetism, and geometry in bulk as well as ultra-thin limit. Note that we came to know about a similar work on a similar system $\mathrm{Nb_3Cl_8}$ [248] during the manuscript preparation phase of this work.

## 5.2 Results

### *5.2.1 Crystal structure and kagome geometry in* $\mathrm{Nb_3I_8}$

Figure 5.1(a) shows the layered crystal structure of $\mathrm{Nb_3I_8}$, in which a unit cell consists of six layers with weak interlayer van der Waal bond along the crystallographic $c$ axis and strong intralayer covalent bond. The structure is trigonal in the rhombohedral space group $\mathrm{R\bar{3}m}$ and the lattice constants are: $a = b = 7.60$ Å and $c = 41.715$ Å [241]. Two sheets of $\mathrm{I}$ atoms sandwich the $\mathrm{Nb}$ atomic planes, each sheets with two inequivalent layers of iodine atoms. The top view of the crystal structure presented in Figure 5.1(b), from which it can be seen that the $\mathrm{Nb}$ atoms are arranged in a breathing kagome geometry (also see Figure 5.1(c), where the $\mathrm{Nb}$ atomic layer is

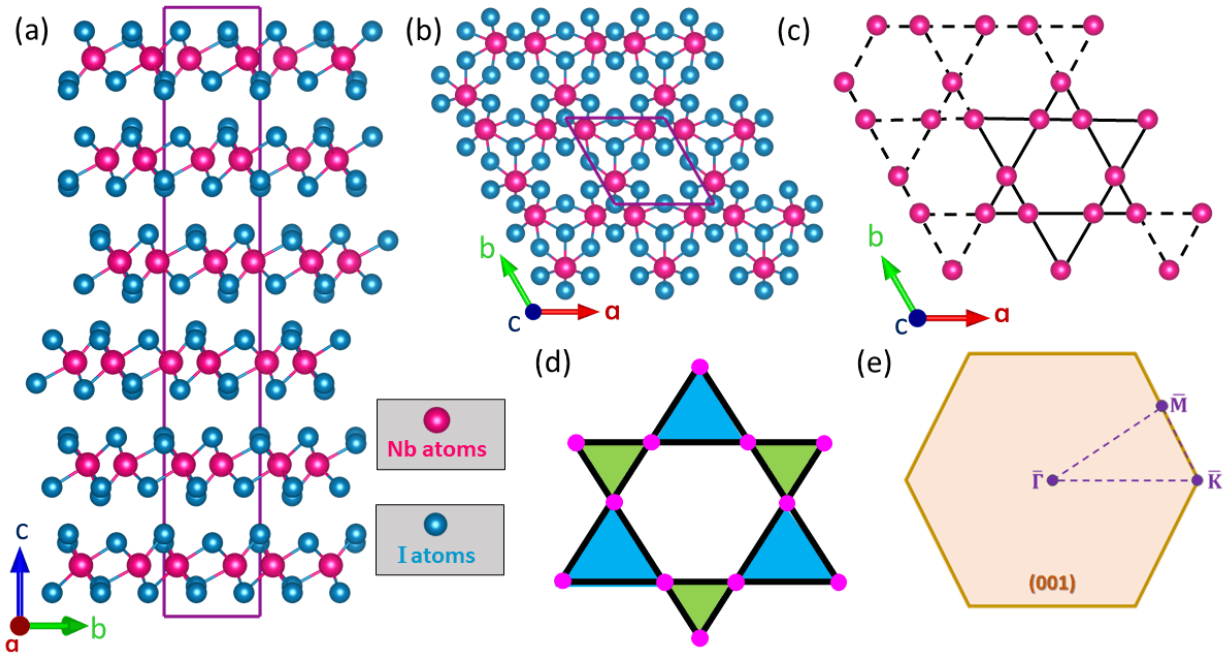


Figure 5.1: Crystal structure of $Nb_3I_8$. (a) Crystal structure (side view) of $Nb_3I_8$, where cyan and teal colored balls represent Niobium and Iodine atoms, respectively. (b) Top view of the crystal structure. (c) Breathing kagome plane of the Niobium atoms. (d) Schematic of the breathing kagome geometry. (e) (001) surface projected hexagonal BZ.

isolated). The schematic of a breathing kagome geometry with alternate triangles of two different sizes is presented in Figure 5.1(d). Because of a very weak van der Waal bond along the $c$ direction, the crystals of $Nb_3I_8$ easily cleave along $(001)$ and hence a $(001)$ surface projected hexagonal BZ is presented in Figure 5.1(e).

The high-quality crystals of $Nb_3I_8$ used in this work have been synthesized using chemical vapor transport (CVT) method (see method section for details). The structural and compositional characterizations of the $Nb_3I_8$ crystals are shown in Figure 5.2. The single crystal XRD shows sharp $(00l)$ peaks indicative of $ab$-plane orientation of the crystal surface (see Figure 5.2(a)). Compositional characterization performed using scanning electron microscopy (SEM) and energy dispersive X-ray spectroscopy (EDS) shows an elemental ratio $Nb : I = 2.96 \pm 0.14 : 8.00$, where the

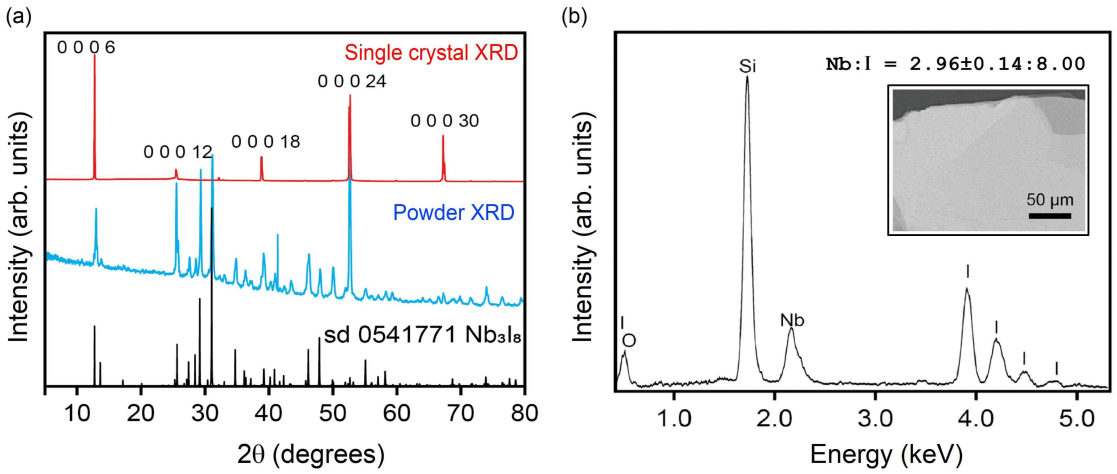


Figure 5.2: Sample Characterization. (a) Powder X-ray diffraction (blue) and single crystal X-ray diffraction (red) results on $Nb_3I_8$. (b) Energy dispersive X-ray spectroscopy result. Inset shows a $Nb_3I_8$ flake exfoliated on $SiO_2/Si$ substrate.

error propagation was obtained through multiple measurements. A representative EDS result is presented in Figure 5.2(b) and the elemental analysis is presented in Table 5.1.

Table 5.1: EDS analysis of $Nb_3I_8$.

| Element | Series | Wt% | Wt% Sigma | Atomic% |
|---|---|---|---|---|
| Si | K Series | 29.86 | 1.26 | 54.20 |
| I | L Series | 55.53 | 1.64 | 22.31 |
| O | K Series | 4.78 | 0.8 | 15.24 |
| Nb | L Series | 15.02 | 0.56 | 8.24 |

### *5.2.2 Flat and weakly dispersing bands in the ARPES spectrum*

Next, we turn to the analysis of the ARPES measurements on single crystals of $Nb_3I_8$. Energy contours at the Fermi level and at various binding energies as noted on top of each plot are presented in Figure 5.3. Consistent with the semiconducting nature of $Nb_3I_8$, no photoemission signal

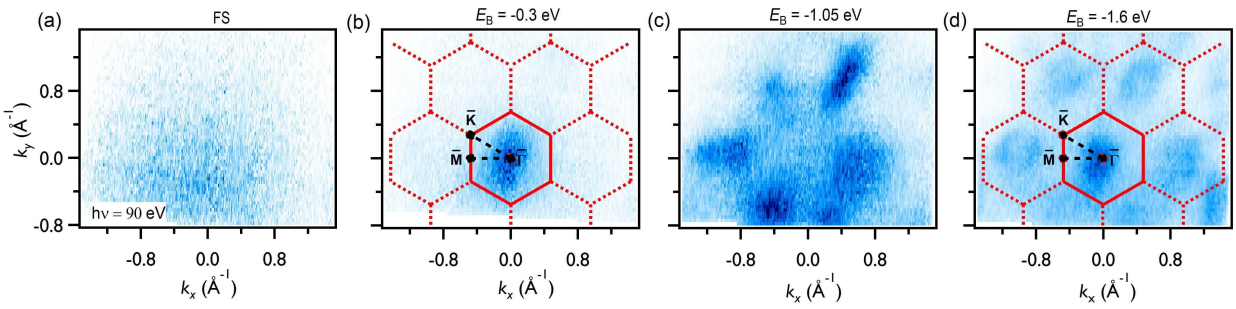


Figure 5.3: Fermi surface and constant energy contours measured by ARPES. (a) Fermi surface measured with photon energy of 90 eV. (b)-(d) Constant energy contours taken at the binding energies noted on top of each plots.

is observed at the Fermi level but the signal can be observed around $-300$ meV binding energy. At this binding energy, the photoemission signal is suppressed out of a single BZ. A well defined hexagonal symmetry can be observed in the energy contour plot at $-1.6$ eV binding energy.

Because of the breathing kagome geometry of Nb atoms in $Nb_3I_8$, its electronic band structure is expected to feature flat bands. Such flat bands arising from breathing kagome geometry may be intrinsically robust [98]. In order to look for the presence of such bands, we analyze the dispersion maps along the $\overline{\mathrm{M}}-\overline{\Gamma}-\overline{\mathrm{M}}$ and $\overline{\mathrm{K}}-\overline{\Gamma}-\overline{\mathrm{K}}-\overline{\mathrm{M}}-\overline{\mathrm{K}}$ directions in Figure 5.4. Dispersion map along $\overline{\mathrm{M}}-\overline{\Gamma}-\overline{\mathrm{M}}$ measured with photon energy of $90$ eV shows the presence of multiple flat weakly dispersing bands (Figure 5.4(a)). A set of a flat (labeled B) and a weakly dispersing (labeled A) are observed at around $-500$ meV binding energy. The presence of two bands around this binding energy is confirmed by the second derivative plot (Figure 5.4(b)). Energy distribution curve (EDC) (fitted using voigt function) integrated within an momentum window of $(-0.4$ Å$^{-1} - 0$ Å$^{-1})$ in Figure 5.4(a) is presented in Figure 5.4(c), and EDC integrated within $(-0.5$ Å$^{-1} - 0$ Å$^{-1})$ in Figure 5.4(b) is presented in Figure 5.4(d). Both EDCs confirm the presence of two bands around $-500$ meV binding energy. A similar band structure is obtained for a different photon energy of $110$ eV (see Figure 5.4(e)). Experimental band structure along the $\overline{\mathrm{K}}-\overline{\Gamma}-\overline{\mathrm{K}}-\overline{\mathrm{M}}-\overline{\mathrm{K}}$ direction

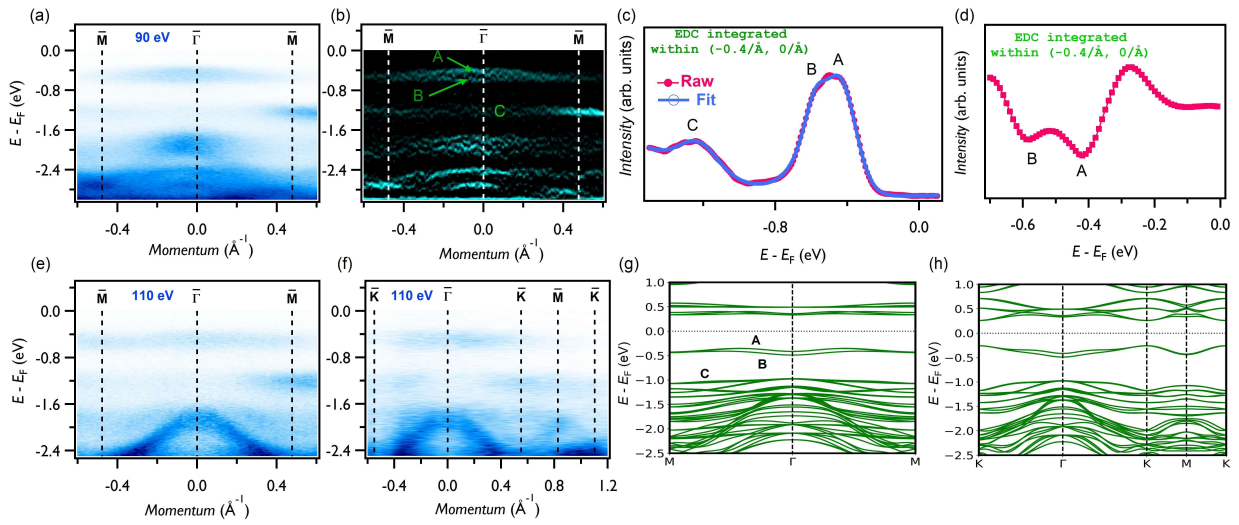


Figure 5.4: Flat bands in the electronic structure of $Nb_3I_8$. (a) Experimental energy versus momentum dispersion along the $\overline{\mathrm{M}} - \overline{\Gamma} - \overline{\mathrm{M}}$ direction measured with photon source of energy 90 eV. (b) Second derivative plot of (a). (c) Energy distribution curve integrated within $(-0.4\ \text{Å}^{-1}, 0\ \text{Å}^{-1})$ in (a) and its voigt fit. (d) Energy distribution curve integrated within $(-0.4\ \text{Å}^{-1}, 0\ \text{Å}^{-1})$ of second derivative plot in (b). (e)-(f) Electronic dispersion along $\overline{\mathrm{M}} - \overline{\Gamma} - \overline{\mathrm{M}}$ and $\overline{\mathrm{K}} - \overline{\Gamma} - \overline{\mathrm{K}} - \overline{\mathrm{M}} - \overline{\mathrm{K}}$, respectively measured using photon energy of 110 eV. (g)-(h) Band structure calculations along $\mathrm{M} - \Gamma - \mathrm{M}$ and $\mathrm{K} - \Gamma - \mathrm{K} - \mathrm{M} - \mathrm{K}$, respectively.

is presented in Figure 5.4(f), where flat and weakly dispersing bands are present. The bulk band calculations along the $\mathrm{M} - \Gamma - \mathrm{M}$ and $\mathrm{K} - \Gamma - \mathrm{K} - \mathrm{M} - \mathrm{K}$ are presented in Figures 5.4(g) and 5.4(h), respectively. The calculated results qualitatively support the experimental observation of the band structures. Specially in the calculation along $\mathrm{M} - \Gamma - \mathrm{M}$, a set of almost flat bands (A and B) can be seen. These bands remain very weakly dispersing going down to monolayer limit as well (see Figure 5.5). Another band set C can also be seen aroung $1\ \mathrm{eV}$ below the midgap. Going more below these bands, a continuum of bands can be seen, which is well reflected by the ARPES spectrum at higher binding energies. The similarity of the band structure, especially of the flat and weakly dispersing bands, in bulk and monolayer (Figure 5.5) indicates that the choce of $k_z$ is not so significant in the experimental measurements and the calculations presented in Figures 5.4 and Figure 5.5 can be compared with the experimental band structure.

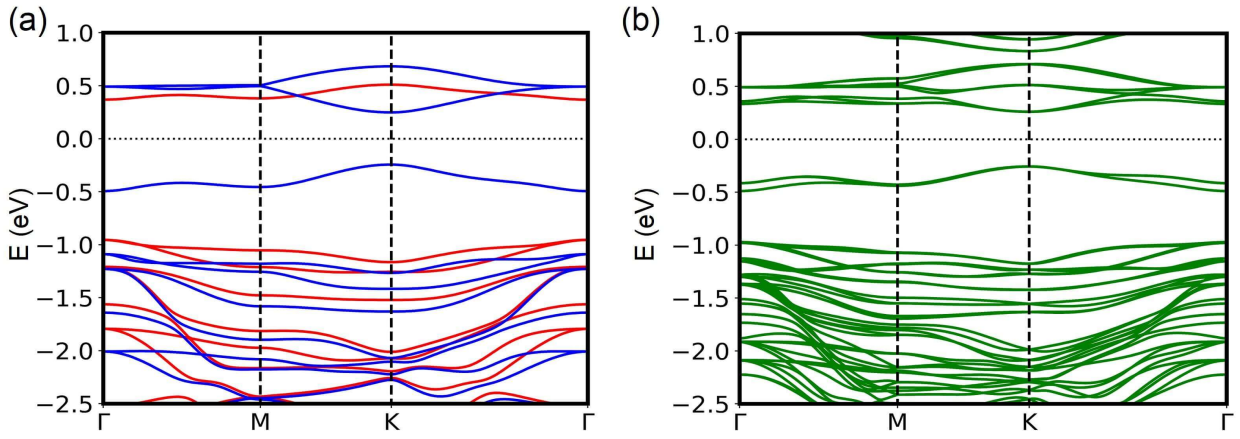


Figure 5.5: Comparison of bulk and monolayer $Nb_3I_8$ band calculations. (a) DFT band structure for monolayer $Nb_3I_8$. (b) Calculated band structure for bulk $Nb_3I_8$.

### *5.2.3 Polarization sensitivity of the flat and weakly dispersing bands*

In Figure 5.6, experimental dispersion maps along $\overline{\mathrm{M}} - \overline{\Gamma} - \overline{\mathrm{M}}$ measured with different photon energies and different light polarizations (LH and LV) are presented. The flat and weakly dispersion bands do not seem to be sensitive to photon energy indicating their 2D nature. On the other hand, the dispersive bands at higher binding energies seem to be dependent on photon energy indicative of their 3D nature. Similarly, the bands A and B are sensitive to LH polarization and the bandset C is sensitive to LV polarization, where both bands of the bandset C are visible (especially observable in $120$ eV and $36$ eV).

A schematic of the ARPES experimental geometry is shown in Figure 5.7(a). The angle between the photon beam and the analyzer lens axis is $65°$ for normal emission condition. That means, the light beam grazes the sample at $25°$. When the sample tilt is $0°$, LV polarization is purely s-polarization. However, LH polarization has components of both s- and p-polarization: $e_{\mathrm{s}} = \sin(\theta + 25°)$ and $e_{\mathrm{p}} = \cos(\theta + 25°)$. Note that our experimental data were taken at $\theta = -4°$. The EDC (fitted with voigt function) for LH polarized $120$ eV photon beam shows strong intensity

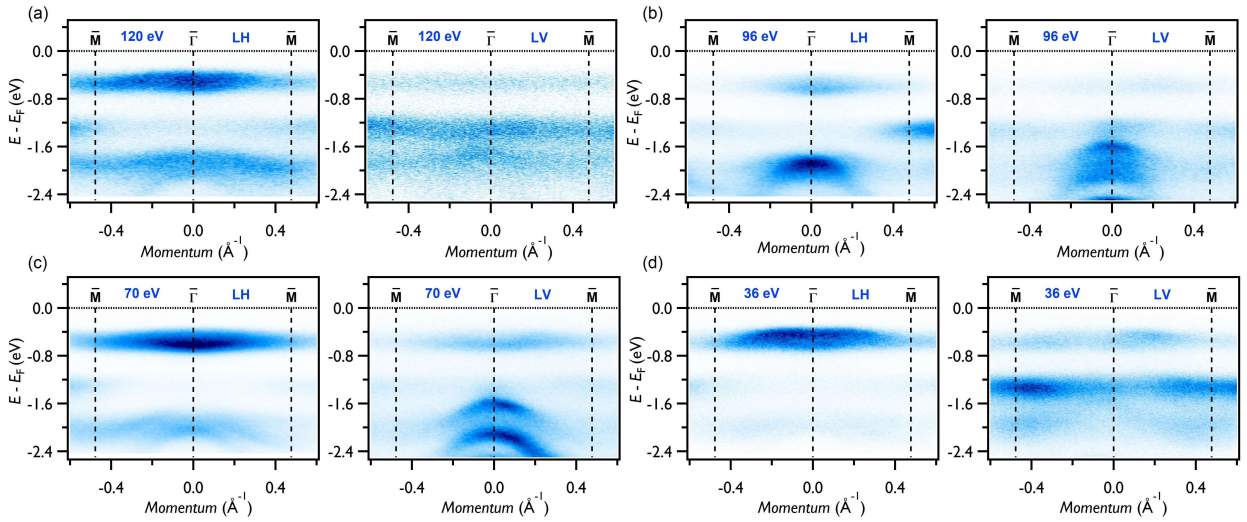


Figure 5.6: Polarization and photon energy dependent ARPES measurements. (a)-(d) Band dispersion along $\mathrm{M}-\Gamma-\mathrm{M}$ measured with linear horizontal polarized (left panels) and linear vertical polarized (right panels) light with various photon energies as noted on each plots.

around the position of bands A and B (Figure 5.7(b)), consistent with the sensitivity of these bands to LH polarization. On the other hand, the intensity in EDC for LV polarized $120\ \mathrm{eV}$ photon beam is stronger around the position of bandset C (Figure 5.7(c)), consistent with the sensitivity of the bandset C to LV polarized light. Contribution of the $\mathrm{Nb}\ d$ and $\mathrm{I}\ p$ in the calculated band structure is presented in Figure 5.7(d). The flat and weakly bands A, B, and C have strong contribution from $\mathrm{Nb}\ d$. As the $\mathrm{Nb}$ atoms lie only in the breathing kagome plane, this indicates that the flat and weakly dispersing bands observed in our measurements are originated from the breathing kagome plane of $\mathrm{Nb}$ atoms. Contributions from the individual $\mathrm{Nb}\ d$ orbitals are presented in Figure 5.8. It can be seen that the set of bands A and B is strongly contributed by $d_{z^2}$ orbitals and the bandset C has major contribution from $d_{xy}$ orbitals but has significant contribution from other $d$-orbitals as well.

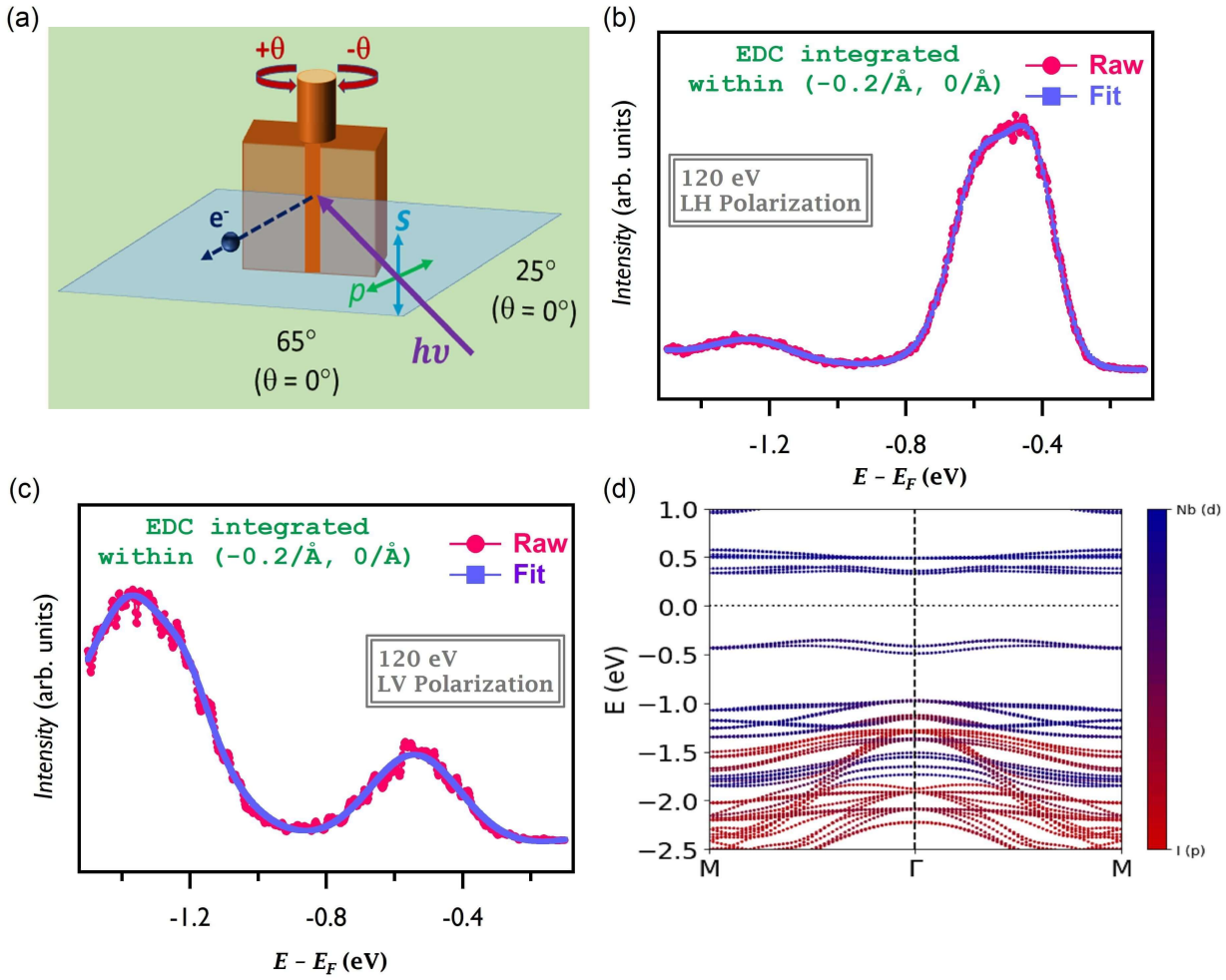


Figure 5.7: Experimental geometry and polarization dependence of flat bands. (a) Experimental geometry for the ARPES measurements. (b)-(c) Integrated energy distribution curves within $(-0.2\ \text{Å}^{-1}, 0\ \text{Å}^{-1})$ momentum window taken for $\overline{\text{M}} - \overline{\Gamma} - \overline{\text{M}}$ data in Figure 5.5(a). (d) Orbital-resolved calculation along the $\text{M} - \Gamma - \text{M}$ direction.

## 5.3 Conclusion

To conclude, this study on $Nb_3I_8$ unveils the spectroscopic evidence of flat and weakly dispersing bands in its electronic structure by utilizing ARPES and supportive DFT calculations. Polarization dependent measurements reveal the sensitivity of these flat and weakly dispersing bands to differ-

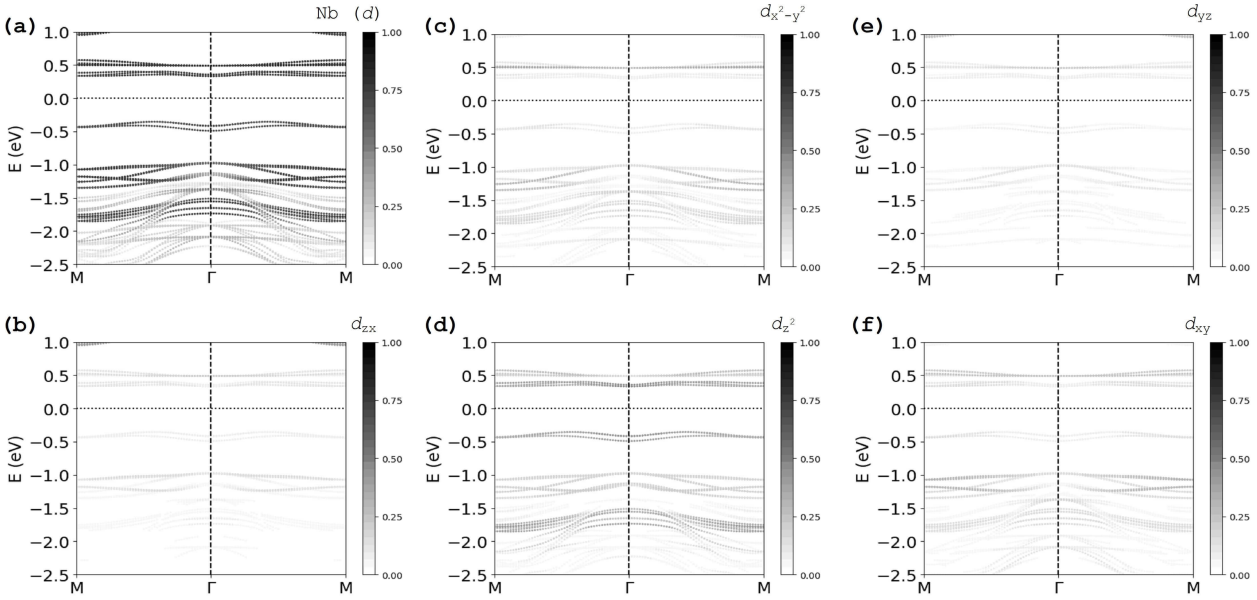


Figure 5.8: Contribution of individual $\mathrm{Nb}$ $d$ orbitals. (a) Total contribution of $\mathrm{Nb}$ $d$ orbitals in the electronic structure along $\mathrm{M}-\Gamma-\mathrm{M}$. (b)-(f) Individual contribution of $d_{zx}$, $d_{x^2-y^2}$, $d_{z^2}$, $d_{yz}$, and $d_{xy}$ orbitals, respectively in the $\mathrm{M}-\Gamma-\mathrm{M}$ band structure.

ent light polarizations. Photon energy dependent measurements show that these bands have 2D nature and also show that the dispersive bands are present at higher binding energies that are 3D in nature. These observations are possible as the sample is 3D bulk sample although the material itself is a van der Waal 2D material. This material is easily exfoliable down to ultra-thin limit (see Figure 5.9 for exfoliation images). The moderate semiconducting band gap is as desired for optoelectronic applications. As it is predicted to host magnetic order in the monolayer limit, our study puts forward an easily exfoliable semiconducting breathing kagome material as a platform to explore the interaction of geometry, correlations, and magnetism in a 2D material and also to explore its electronic applications.

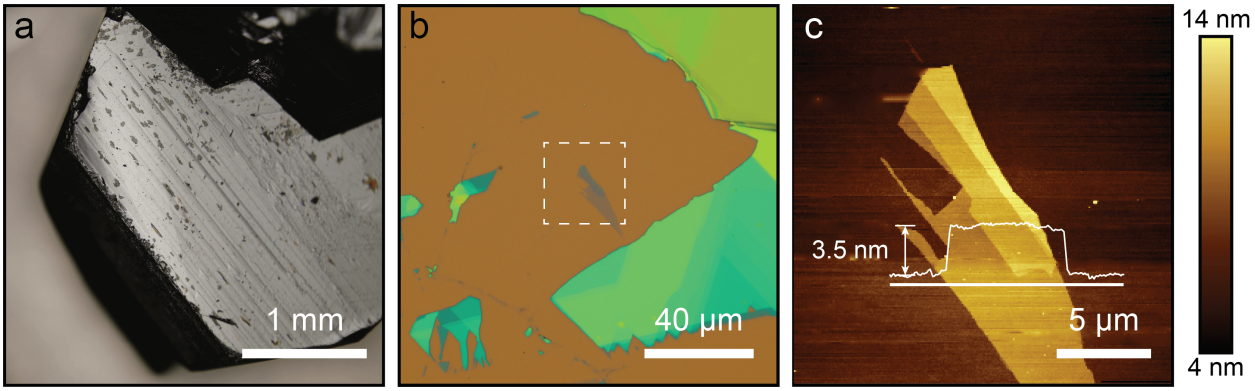


Figure 5.9: Mechanical exfoliation of $Nb_3I_8$. (a) Optical image of a $Nb_3I_8$ crystal. (b)-(c) Optical and atomic force spectroscopy images, respectively of mechanically exfoliated $Nb_3I_8$.

## 5.4 Experimental and computational methods

### *5.4.1 Crystal growth and characterization*

Single crystals of $Nb_3I_8$ were grown by using the chemical vapor transport technique. Iodine was used as a transport agent. High purity $Nb$ powder ($0.2303\ g$) and $I$ ($0.8021\ g$) were sealed in a quartz tube under $< 20\ mtorr$ vacuum conditions. The quartz tube was then loaded inside of a two-zone furnace and ramped for $20\ hours$ to get up to $652\ ^\circ C$ on the precursor side and $650\ ^\circ C$ on the growth side. After letting the growth process for about $70\ hours$, the tube was naturally cool to room temperature to obtain high-quality crystals of $Nb_3I_8$. The structural characterization was done using X-ray diffraction and compositional analysis was done SEM and EDS.

### *5.4.2 Density functional theory calculations*

Theoretical calculations of the band structure were carried out using the density functional theory (DFT) approach [169, 170] by using $ONCVPSP$ (Optimized Norm-conserving Vanderbilt Pseu-

dopotential) [249, 250] implemented in the $\mathrm{QUANTUM\ ESPRESSO}$ package [213, 214, 215]. PBE-type functional was used to account for the exchange-correlation effects [175] and van der Waals correction was included withing the $\mathrm{D2}$ formalism [251]. To account for the on-site coulomb interaction, a Hubbard potential of $2\ \mathrm{eV}$ was used for $\mathrm{Nb}\ d$ orbitals [242]. A sextuple layered unit cell was used for bulk calculations (with lattice parameters $a = b = 7.6000$ Å and $c = 41.7150$ Å [241]) in the stable AFM state (interlayer AFM with alternate spins on alternate layers was used). Only a single layer was used for monolayer calculations in the stable FM state ($c = 52.5000$ Å). Mid-gap level was set as zero-binding energy level for comparison with experimental results.

### *5.4.3 ARPES measurements*

The high-resolution ARPES measurements were performed using the synchrotron light source available at the ALS Beamline 4.0.3.2, which is equipped with a high-efficiency R8000 electron analyzer. Flat samples prepared on copper posts were loaded into the ARPES chamber maintained at ultra-high vacuum better than $10^{-10}$ torr and then cleaved in-situ. Cermaic posts were mounted on top of the samples using the silver epoxy paste to cleave the top surface of the sample thereby exposing a fresh shiny surface for ARPES measurements. Experiments were conducted at a high temperature of $260\ \mathrm{K}$ in order to dodge the charging effects using LH and LV polarized photon beams within energy range of $30 - 120\ \mathrm{eV}$.

# CHAPTER 6: OBSERVATION OF DIRECTION DEPENDENT CHARGE DENSITY GAP IN A VAN DER WAAL ANTIFERROMAGNET

The results of this work are currently under review.

As platforms that exhibit CDW and magnetic orderings, rare-earth-based $R\mathrm{Te}_3$ ($R$ = rare-earth elements) have been enticing significant research interests in recent times. In this work, we study the Fermi surface and electronic band dispersion in an antiferromagnetic $R\mathrm{Te}_3$ system - $\mathrm{GdTe}_3$ by means of high-resolution ARPES measurements. We directly reveal CDW induced partial gap at the Fermi surface and demonstrate the direction dependence of the gap in the momentum space. This work brings out a platform to investigate on the dynamics of CDW and magnetism in this van der Waal 2D material.

## 6.1 Introduction

CDW, a phenomena associated with FS instabilities [102, 103, 104], has remained an important topic of study over the decades because of its relevance in understanding of several properties of solids such as electron-phonon interaction and structural transitions as well as its occurrence with other co-existing or competing exotic phenomena such as superconductivity and magnetism [105, 106, 107, 108, 109, 110, 111, 112, 113, 114, 115]. In general, CDW is associated with mechanisms such as FS nesting, electron-phonon coupling, and exciton condensation [121]. The FS nesting is perfect in 1D and can be visualized in terms of Peierl's distortion [116, 117]. At higher dimensions, however, the nesting is absent or becomes imperfect [120]. This leads to metallic FSs despite the CDW transition in higher dimensions [118, 119].

Rare-earth ($R$)-based van der Waals materials in the family $R\mathrm{Te}_3$ have captured significant research

interest because of the presence of a high-temperature CDW ordering and in addition, a lower temperature magnetic ordering [252, 253, 254, 255]. The members with heavier $R$ also possess a second CDW order at low temperatures [252, 253]. The FS and CDW induced gap in these materials have been investigated by using the ARPES technique in recent times [118, 256, 257, 258, 259, 260, 261, 262, 263]. The CDW induced gap depends on momentum direction and its maximum varies with $R$ [257]. A member of this family - $\mathrm{GdTe_3}$ - has steep bands with high velocity crossing the Fermi level [262] and a very high electronic mobility [264]. In addition to the CDW and magnetic orderings, $\mathrm{GdTe_3}$ has properties that entice more researches on its electronic properties such as pressure induced superconductivity [265], and easy mechanical exfoliation to ultra-thin limit [264, 266] allows to study the layer dependence of the CDW ordering.

In this work, via ARPES measurements, we reveal the FS and underlying electronic structure in $\mathrm{GdTe_3}$. Thermodynamic measurements reveal the presence of high-temperature CDW ordering ($\sim 380\ \mathrm{K}$) and a lower-temperature antiferromagnetic transition ($\sim 12\ \mathrm{K}$). ARPES data reveals a two-fold symmetric partially gapped FS. The electronic structure analysis shows that the gap below the Fermi level induced by CDW is maximum along the $\overline{\Gamma} - \overline{\mathrm{Y}}$ direction and shrinks going away from this direction towards $\overline{\Gamma} - \overline{\mathrm{M}}$. Overall, this work reports an anisotropic directional dependent CDW gap and opens an avenue towards further investigation of CDW dynamics in this antiferromagnetic layered material.

## 6.2 Results

### *6.2.1 Crystal structure and bulk characterization*

$\mathrm{GdTe_3}$ belongs to the orthorhombic crystalline family in the space group $Cmcm\#63$. As shown in Figure 6.1(a), $\mathrm{Te} - \mathrm{Te}$ bilayers sandwich the $\mathrm{Gd} - \mathrm{Te}$ slabs. Note that we adopt the representation

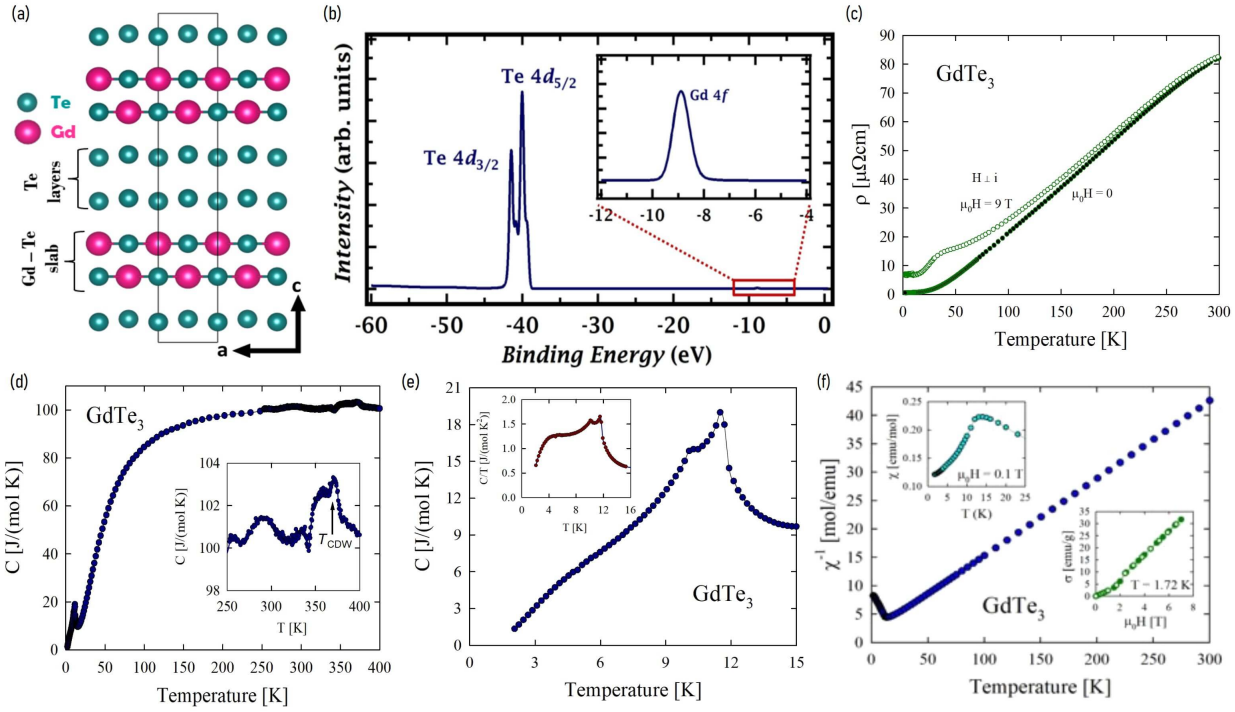


Figure 6.1: Crystal structure and characterization. (a) Crystal structure of $GdTe_3$. (b) Spectroscopic core level spectrum. (c) Resistivity as a function of temperature at zero field (black) and at an applied field of $9$ T. (d) Result of the heat capacity measurements upto $400$ K. Inset is zoomed in view near the CDW transition temperature. (e) Heat capacity at low temperatures. Inset shows heat capacity to temperature ratio plotted against temperature. (f) Inverse of magnetic susceptibility as a function of temperature. Upper left inset: Magnetic susceptibility at lower temperatures measured with an applied field strength of $0.1$ T. Lower right inset: Field variation of magnetization at a temperature of $1.72$ K.

of in plane $ab$ and out-of-plane $c$ axis notation. $Te$ layers are connected through the weak van der Waals bonding along $c$-direction, therefore, the crystals of $GdTe_3$ easily cleave along the $(001)$ direction.

A spectroscopic core level spectrum for a representative $GdTe_3$ single crystal used in the measurements is presented in Figure 6.1(b), which depicts peaks associated with the Gd 4f and Te $4d$ orbitals. The resistivity measurements (results presented in Figure 6.1(c)) indicate the metallic nature of the sample and show a high RRR value indicative of high quality of the crystals. Heat

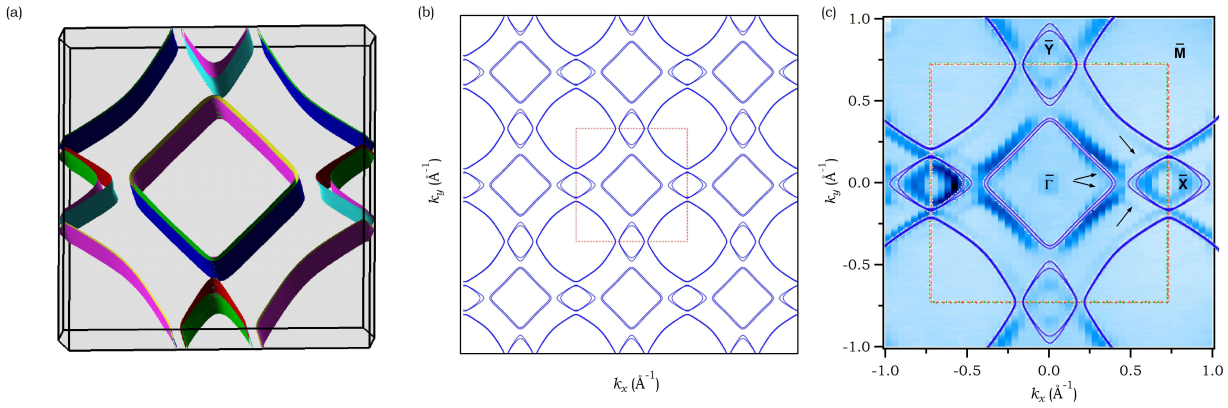


Figure 6.2: Comparison between theoretical and experimental FSs. (a) Calculated 3D FS. (b) Calculated 2D FS (analogous to top view of (a). (c) Experimental FS at a photon energy of $90$ eV integrated within $-300$ meV and overlaid experimental FS.

capacity measurements carried upto $400$ K shows a CDW transition at around $380$ K (see Figure 6.1(d) and inset) and a peak around $12$ $K$ corresponding to the antiferromagnetic ordering. In order to focus on this peak, we present, in Figure 6.1(e), the heat capacity at lower temperatures. A distinct peak exists at the transition temperature $T_{\mathrm{N}} \sim 12$ K followed by a subsequent peak at $\sim 10$ K. The results of the magnetic property measurements are presented in Figure 6.1(f). The inverse magnetic susceptibility ($\chi^{-1}(T)$) (measured in applied field of $0.1$ T) shows Curie-Weiss behavior at higher temperatures. As shown in the upper left inset of Figure 6.1(f), a maximum is seen in the $\chi(T)$ graph at the transition temperature. The magnetization variation with field measured at $T = 1.72$ K (Figure 6.1(f) lower right inset) shows no hysteresis, in line with the antiferromagnetic ground state.

### *6.2.2 Observation of partially gapped FS*

Figure 6.2(a) shows 3D Fermi surface obtained from DFT calculations. The FS has two contributions - one from the 2D $\mathrm{Te} - \mathrm{Te}$ layer, which gives diamond shaped pockets made by main bands

composed of $p_x$ and $p_y$ orbitals of $\mathrm{Te}$ atoms in the $\mathrm{Te}-\mathrm{Te}$ layer. The second contribution is from the 3D unit cell, which has $\sqrt{2}$ times larger in-plane lattice constants. This gives rise to a folded band structure as shown in Figure 6.2(b), where the avoided crossings between the bands create extra small diamond pockets at the $\mathrm{X}$ and $\mathrm{Y}$ points. In Figure 6.2(c), we present ARPES measured FS (integrated within $-300\ \mathrm{meV}$) and overlaid calculated FS. We can observe a diamond shaped pocket centered at the $\overline{\Gamma}$ points made by the main bands. In addition, some less intense bands can be seen creating a outer diamond but with avoided crossings. These less intense bands are the shadow bands created by the folding as mentioned earlier. The avoided crossings among the main and shadow bands create small diamond shaped pockets at the $\overline{\mathrm{X}}$ and $\overline{\mathrm{Y}}$ points. Note that the BZ presented in Figure 6.2(c) is the 2D $(001)$ SBZ projected from the 3D BZ. A deeper inspection leads to the observation of more less intense bands (shown by arrows) other than the folded shadow bands. These bands are as a result of the FS reconstruction caused by the CDW ordering.

Figure 6.3 presents the ARPES measured Fermi surface and constant energy contours at photon energies of $90\ \mathrm{eV}$ (a-d) and $68\ \mathrm{eV}$ (e-h). The FS is two-fold symmetric, where strong photoemission signal indicating main band pockets around the $\overline{\mathrm{X}}$ exists, however, away from the $\overline{\mathrm{X}}$ points towards $\overline{\Gamma}-\overline{\mathrm{M}}$ and $\overline{\Gamma}-\overline{\mathrm{Y}}$, no such strong signal exists indicating the presence of gap along these directions at the Fermi level. Moving down in binding energy, the strong photoemission signal begins to move towards $\overline{\Gamma}-\overline{\mathrm{M}}$ line. At around $-130\ \mathrm{meV}$ binding energy (for photon energy of $90\ \mathrm{eV}$; around $-140\ \mathrm{meV}$ for $68\ \mathrm{eV}$ photon energy), $\overline{\Gamma}-\overline{\mathrm{M}}$ direction is no longer gapped. However, at this binding energy, no photoemission signal exists away from $\overline{\Gamma}-\overline{\mathrm{M}}$ towards $\overline{\Gamma}-\overline{\mathrm{Y}}$. Photoemission signal along the $\overline{\Gamma}-\overline{\mathrm{Y}}$ direction begins to appear at a binding energy of around $290\ \mathrm{meV}$ (for $90\ \mathrm{eV}$ photon energy; around $300\ \mathrm{meV}$ for $68\ \mathrm{eV}$ photon energy). These results show the partially gapped nature of the FS, thereby agreeing with the metallic nature of $\mathrm{GdTe_3}$ even with CDW transition.

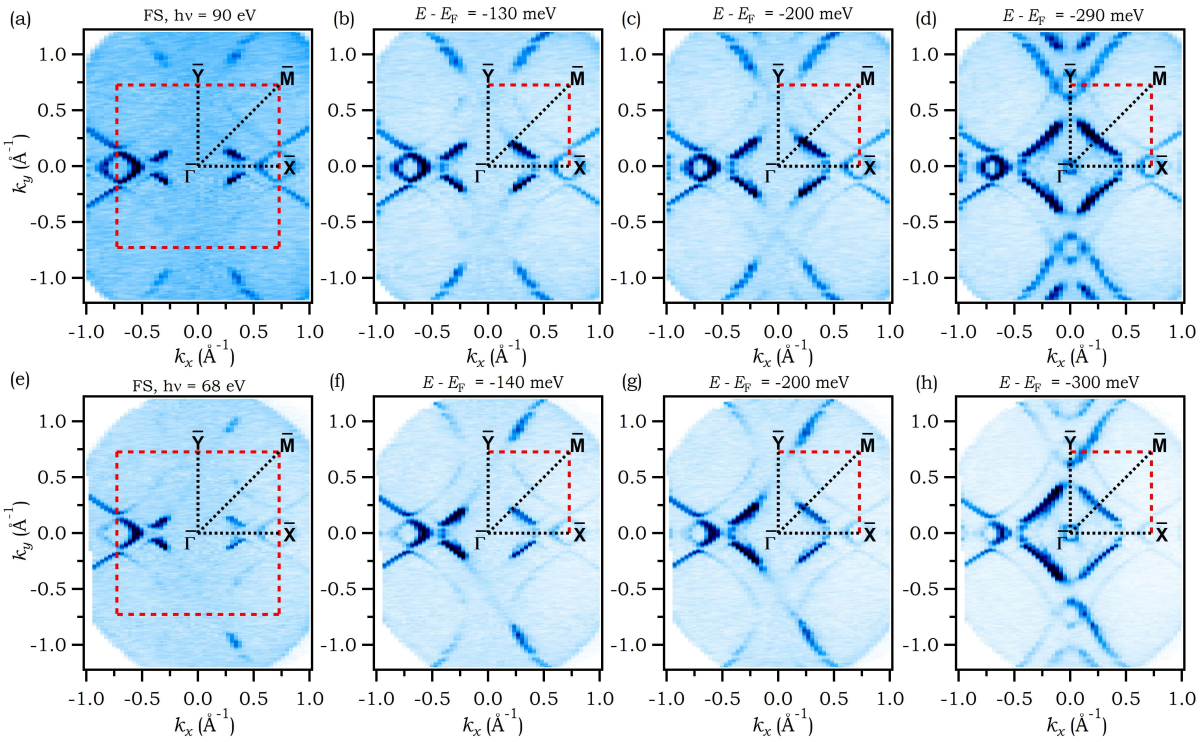


Figure 6.3: Partially gapped metallic FS and evolution with binding energy. (a)-(d) FS and constant energy contours at binding energies, marked on top of each plot, measured with a photon energy of $90$ eV. (e)-(h) FS and energy contours at binding energies, marked on top of each plot, measured with a photon energy of $68$ eV.

### *6.2.3 Directional dependence of the CDW gap*

After obtaining the information about the slow filling of the main band intensity on going towards the $\overline{\Gamma}-\overline{\mathrm{Y}}$ line from the $\overline{\Gamma}-\overline{\mathrm{X}}$ line, we studied the dispersion maps along the $\overline{\Gamma}-\overline{\mathrm{M}}$ and $\overline{\Gamma}-\overline{\mathrm{Y}}$ directions and in between. The results are presented in Figures 6.4 and 6.5. $\overline{\mathrm{M}}-\overline{\Gamma}-\overline{\mathrm{M}}$ dispersion map measured with photon energy of $90$ eV is presented in Figure 6.4(a). The main bands are restricted to well below the Fermi level indicating the CDW induced gap at the Fermi level. To quantify the gap, we took an integrated EDC and its Fermi fit (Figure 6.4(b)). The extracted value of the CDW gap below the Fermi level along the $\overline{\mathrm{M}}-\overline{\Gamma}-\overline{\mathrm{M}}$ direction is about $130$ meV, consistent

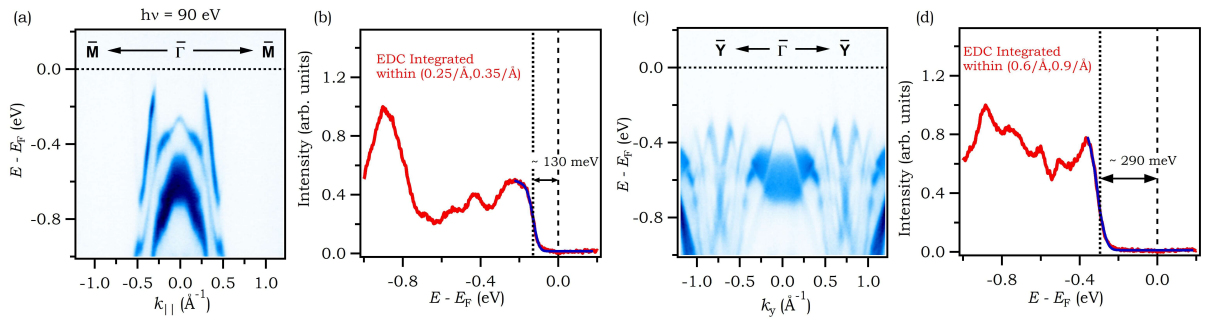


Figure 6.4: Dispersion maps measured with photon energy of $90$ eV. (a) Dispersion map along the $\overline{\mathrm{M}} - \overline{\Gamma} - \overline{\mathrm{M}}$ direction. (b) Integrated EDC within momentum window of $(0.25$ Å$^{-1}, 0.35$ Å$^{-1})$ in (a). (c) Dispersion map along the $\overline{\mathrm{Y}} - \overline{\Gamma} - \overline{\mathrm{Y}}$ direction. (d) Integrated EDC within momentum window of $(0.6$ Å$^{-1}, 0.9$ Å$^{-1})$ in (c).

with the observation in Figures 6.3(a-b). $\overline{\mathrm{Y}} - \overline{\Gamma} - \overline{\mathrm{Y}}$ dispersion map measured with photon energy of $90$ eV is presented in Figure 6.4(c) and an integrated EDC corresponding to this dispersion map is presented in Figure 6.5(d). From the Fermi fit of the leading edge in the EDC, the value of the gap below the Fermi level along this direction is about $290$ meV, which is consistent with the observation in Figures 6.4(a-d).

In Figure 6.5, the results of the measurements with a photon energy of $68$ eV are presented. The dispersion maps along the $\overline{\mathrm{M}}-\overline{\Gamma}-\overline{\mathrm{M}}$ and $\overline{\mathrm{Y}}-\overline{\Gamma}-\overline{\mathrm{Y}}$ and their second derivative plots show a similar behavior of gap, with the gap size below the Fermi level about $140$ meV along $\overline{\Gamma} - \overline{\mathrm{M}}$ and about $300$ meV along $\overline{\Gamma} - \overline{\mathrm{Y}}$. This is in agreement with the observations in Figures 6.4(e-h). In order to quantify the evolution of the CDW gap in between $\overline{\Gamma} - \overline{\mathrm{M}}$ and $\overline{\Gamma} - \overline{\mathrm{Y}}$, we took dispersion maps along different cuts represented by different colored dashed-lines in Figure 6.5(e). The lines are labeled with an angle with is the counterclockwise angle made by the line with the $\overline{\Gamma}-\overline{\mathrm{Y}}$ direction. The leading edges in the EDCs of the dispersion maps along those lines are shown in Figure 6.5(f). We can see that on going away from $\overline{\Gamma} - \overline{\mathrm{M}}$ $(45°)$ towards $\overline{\Gamma} - \overline{\mathrm{Y}}$ $(0°)$, the leading edge shifts away from the Fermi level. The gap value is plotted against the counterclockwise angle from the $\overline{\Gamma} - \overline{\mathrm{Y}}$

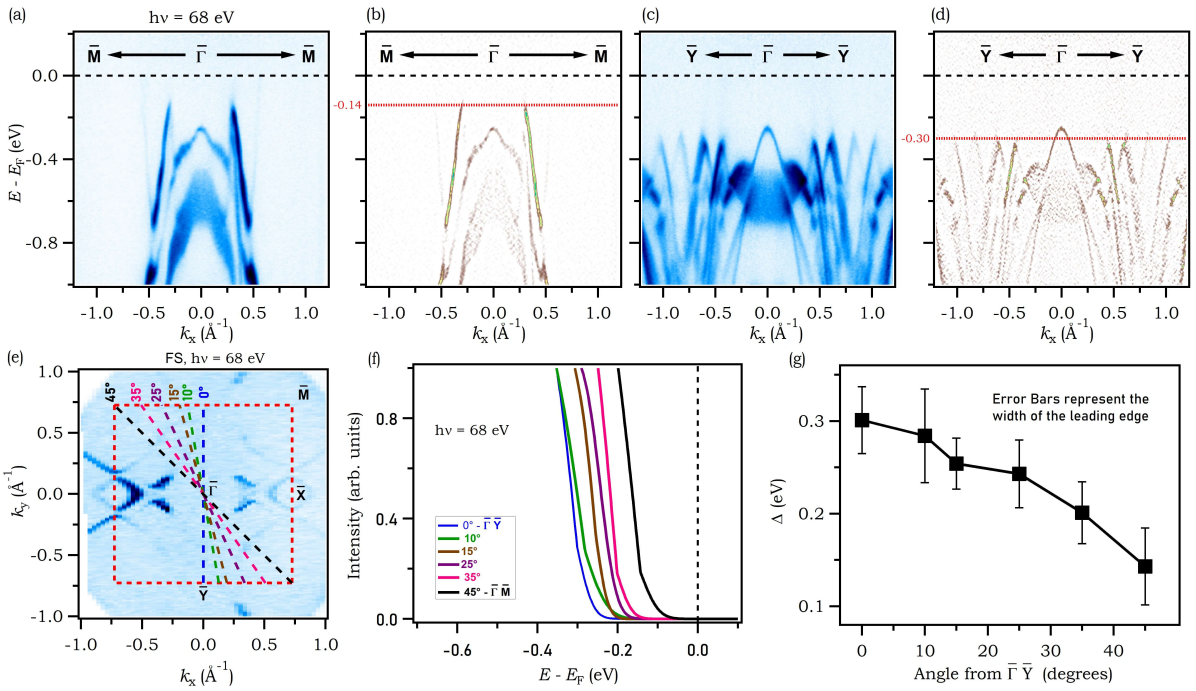


Figure 6.5: Dispersion maps at $68$ eV photon energy and directional evolution of the gap. (a)-(b) $\overline{\mathrm{M}} - \overline{\Gamma} - \overline{\mathrm{M}}$ dispersion map and its second derivative, respectively. (c)-(d) $\overline{\mathrm{Y}} - \overline{\Gamma} - \overline{\mathrm{Y}}$ dispersion map and its second derivative, respectively. (e) $68$ eV FS map with different colored dashed lines representing cuts at different angles from $\overline{\Gamma} - \overline{\mathrm{Y}}$. (f) Leading edges in the EDCs for cuts along the cut directions shown in (e). (g) Gap below the Fermi level ($\Delta$) plotted against counterclockwise angles from $\overline{\Gamma} - \overline{\mathrm{Y}}$.

direction is presented in Figure 6.5*g*. The gap can be observed gradually increasing going towards $\overline{\Gamma} - \overline{\mathrm{M}}$ from $\overline{\Gamma} - \overline{\mathrm{Y}}$. Similar nature of the gap has been observed in previously reported study on $R\mathrm{Te}_3$ [257].

## 6.3 Conclusions

To conclude, we carried out an ARPES study on a layered van der Waal antiferromagnet $\mathrm{GdTe}_3$, also supported by transport and thermodynamic measurements. Resistivity measurements show a metallic nature despite of the CDW transition. The CDW transition is around $380$ K as observed

from the heat capacity measurements. Heat capacity and magnetic measurements also depict an antiferromagnetic transition at a lower temperature of about $12\ \mathrm{K}$. ARPES measurements reveal a partially gapped FS leading to metallic nature despite of the CDW ordering, consistent with the transport results. The CDW gap depends on the momentum direction and its value is highest along $\overline{\Gamma} - \overline{\mathrm{Y}}$ and gradually reduces going towards the $\overline{\Gamma} - \overline{\mathrm{M}}$ direction. Overall, this work reports the ARPES characterization of FS and CDW induced gap in a layered antiferromagnet, opening up avenues towards exploring the interplay among the parameters such as thickness, magnetic order, and CDW order in 2D materials.

## 6.4 Methods

### *6.4.1 Crystal synthesis and characterization*

The chemical composition and crystal structure of the flux technique-grown $\mathrm{GdTe_3}$ high-quality single crystals were characterized by energy-dispersive X-ray analysis carried out by using a FEI scanning electron microscope equipped with an EDAX Genesis XM4 spectrometer and Oxford Diffraction X'calibur four-circle single-crystal X-ray diffractometer equipped with a CCD Atlas detector, respectively.

### *6.4.2 ARPES measurements*

The high-resolution ARPES measurements were performed using the synchrotron light source available at the SSRL endstation 5-2 in SLAC National Accelerator Laboratory, which is equipped with a high-efficiency DA30 electron analyzer. For the ARPES measurements, the angular and energy resolutions were maintained better than $0.2^{\circ}$ and $20\ \mathrm{meV}$, respectively. Flat samples prepared on copper posts were loaded into the ARPES chamber maintained at ultra-high vacuum better than

$10^{-10}$ torr and then cleaved in-situ. Cermaic posts were mounted on top of the samples using the silver epoxy paste to cleave the top surface of the sample thereby exposing a fresh shiny surface for ARPES measurements. Experiments were conducted at $8\ \mathrm{K}$.

# OTHER PROJECT: INVESTIGATION OF ELECTRONIC STRUCTURE IN A ROTATIONAL TOPOLOGICAL CRYSTALLINE INSULATOR CANDIDATE DIPNICTIDE

The results of this project are currently under review.

The recent research interest in transition metal dipnictides (TMDs) roots from their large magnetoresistance (MR) and their ability to feature topological states in their electronic structure. In this work, we use ARPES and collaborative DFT calculations to investigate the electronic structure and topology in a TMD $\mathrm{TaAs_2}$ and unveil the metallic closed and open pockets at the FS and linearly dispersive, though trivial and bulk originated, bands on its natural cleaving surface. This study reveals topologically dark nature of the natural cleaving surface and the presence of open FS features opens up a way to investigate on the role of open-orbit fermiology in the large MR property of this material.

## Introduction

Presence of spin-polarized Dirac surface states, although insulating in the bulk, and their suitability in low power electronics brought TIs [3, 4, 25, 156] into the core of research investigations in condensed matter physics and material science community. In 3D, four $\mathbb{Z}_2$ invariants $(\nu_0; \nu_1\nu_2\nu_3)$ define strong and weak nature of the TI state [23] (see Chapter 1 section 1.4 for more details). Weak TIs feature Dirac surface states on distinct surfaces that preserve translation symmetry and other surfaces are topologically dark, meaning those surfaces do not preserve any Dirac states [35]. In some materials, crystalline symmetries play a vital role in topological protection of the surface states, and class of such materials is called topological crystalline insulator [36, 37, 38]. In this

class of materials, the Dirac crossing may occur away from the TRIM points at some generic points in the momentum space [37, 38, 267, 268, 269, 270, 271].

TMDs have been studied largely for their large MR [272, 273, 274, 275, 276, 277, 278, 279, 280, 281, 282, 283, 284, 285, 286] and topology [271, 285, 286, 287, 288, 289, 290, 291, 292, 293]. Some dipnictides, including $TaAs_2$, in this material family are predicted to exhibit weak non-trivial electronic structure [277, 271, 287, 288]. Along with non-saturating large MR [288] and weak TI state [271, 287, 288], $TaAs_2$ features a type-II Dirac state because of rotational symmetry preservation on the $(010)$ surface [271]. This highlights the importance of electronic properties measurements in this TMD material. Despite almost electron-hole compensated nature as indicated by the presence of equal volume of hole pockets and electron pockets in previous theoretical study [280] and by comparing magnetotransport results with two-band model [274, 275], finite imbalance between electron-hole densities reported in some other studies [288, 294] may be suggestive of contribution of some other factors as well in the large MR property.

In this work, we have investigated the electronic properties in $TaAs_2$ by utilizing ARPES and collaborative DFT computations, transport, and magneto-transport measurements. Magneto-transport results show large unsaturating MR. One point to note is that this material cleaves along preferred $(\bar{2}01)$ plane, which is different from the rotational symmetry protecting $(010)$ surface. On the $(\bar{2}01)$ surface, our experimental data detects metallic Fermi surface and several linear crossing-like features, which are found to be trivial bulk features by comparing with DFT calculations. The presence of open FS features in the FS may indicate towards potential contribution of open-orbit fermiology in the high MR property. This work gives insight into the electronic structure of $TaAs_2$ and opens up avenue for further electronic properties exploration.

## Results

*Crystal structure, bulk characterization, and bulk band calculations*

Figure 6.6(a) represents the monoclinic crystal structure (in space group $C2/m;\ \#12$) of $\mathrm{TaAs_2}$. Figure 6.6(b) shows a core-level spectrum measured with a photon beam of energy $100\ \mathrm{eV}$. Peaks related to the $3d$ orbitals of $\mathrm{As}$ as well as the $4f$ and $5p$ orbitals of $\mathrm{Ta}$ are observed. Resistivity (Figure 6.6(c)) increases with rise in temperature, depicting a metallic/semimetallic nature of the bulk crystals. Magneto-transport (Figure 6.6(d)) results show that the rise in resistivity with field is extremely large and unsaturating, reaching upto $\sim 4400\%$ at an applied field of $9\ \mathrm{T}$.

A 3D bulk BZ is presented in Figure 6.7(a), where the high-symmetry points are marked. Bulks bands calculated without and with the consideration of SOC are presented in Figures 6.7(b) and 6.7(c), respectively. Several bands are crossing the Fermi level, in line with the metallic/semimetallic nature of $\mathrm{TaAs_2}$. These bands are mainly comprised of $\mathrm{Ta}\ d$ and $\mathrm{As}\ p$ orbitals [271]. When the SOC is neglected, band crossings corresponding to the nodal-lines, along $\Gamma - \mathrm{Y}$ and $\mathrm{A} - \mathrm{M}$, can be observed. However, these crossings are gapped out by SOC thereby creating band inversion at the $\mathrm{A}$ and $\mathrm{Y}$ points. The topological analysis reported in Ref. [271] shows $\mathbb{Z}_2$ topological indices ($\nu_0; \nu_1\nu_2\nu_3$) = $(0; 111)$ indicative of weakly non-trivial TI state and a non-zero value of rotational invariant $n_2^{[010]}$ indicative of two-fold $C_{2[010]}$ rotational symmetry protected non-trivial state, which will exist on the $(010)$ surface.

*Observation of trivial states on the topologically dark ($\bar{2}01$) surface*

In order to identify the cleaving surface orientation, we performed Laue diffraction experiments and the results are presented in Figure 6.8. The comparison of experimentally observed Laue pat-

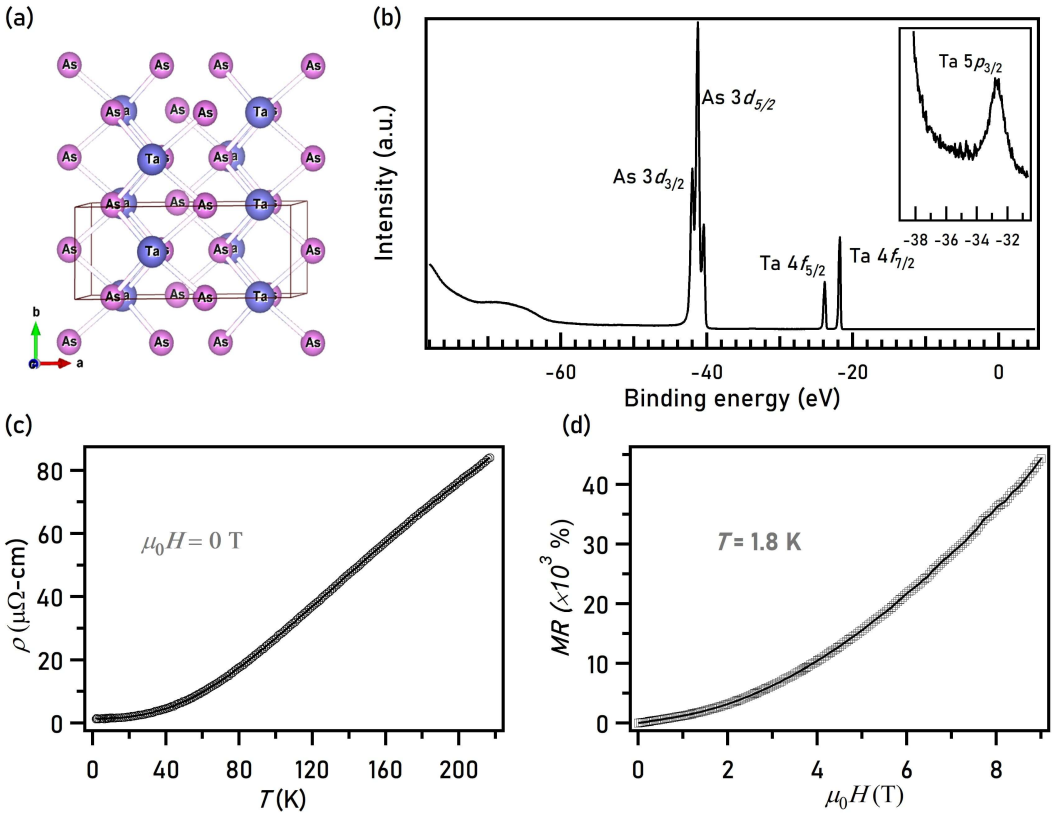


Figure 6.6: Crystal structure and bulk characterization. (a) Crystal structure of $TaAs_2$. (b) Core level spectrum measured with $100$ eV photon source. (c) Temperature variation of zero-field resistivity. (d) Magnetoresistance measured upto $9$ T field at a temperature of $1.8$ K.

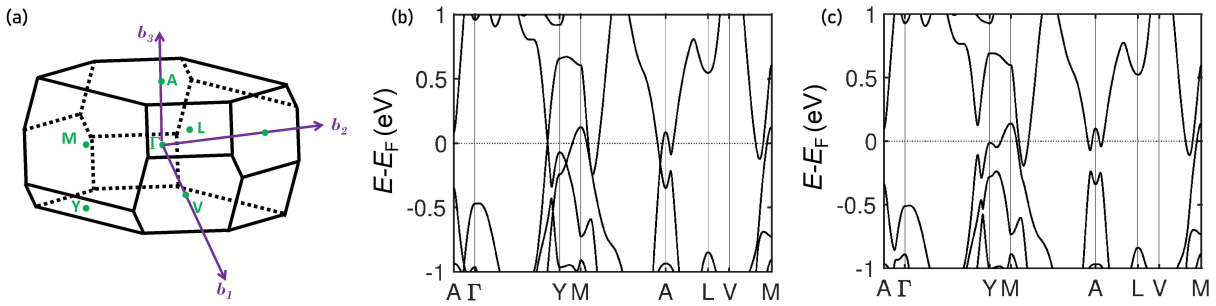


Figure 6.7: Band structure calculations. (a) Bulk BZ showing the high-symmetry points. (b)-(c) Bulk bands calculated along various higy-symmetry directions without and with the consideration of SOC, respectively.

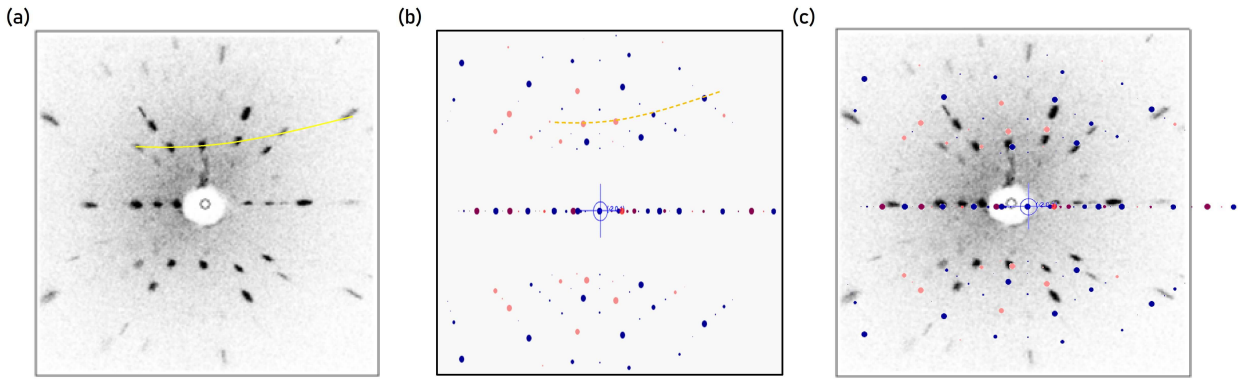


Figure 6.8: Results of Laue analysis. (a) Laue diffraction pattern. (b) QLaue simulation on the $(\bar{2}01)$ surface. (c) QLaue simulation pattern overlaid over the experimental Laue pattern.

tern with QLaue simulation on $(\bar{2}01)$ surface confirms the $(\bar{2}01)$ orientation of the cleaved surface. Note that this surface is different than the $C_{2[010]}$ rotational symmetry preserving $(010)$ surface. Next, we present the results of the ARPES measurements performed to unveil the electronic band dispersion on the cleaved surface in Figures 6.9, 6.10, and 6.11. Experimental FSs (Figures 6.9(a) and 6.9(c)) show multiple pockets confirming that $TaAs_2$ is metallic. Some of the FS pockets are closed and some remain unclosed and extend along the $k_2$ direction (pointed by red arrow in Figure 6.9(c)). Presence of open FS features have been reported in other members of TMD family as well [279, 295]. A elliptical pocket is observed at the center of the BZ and two pairs of circular pockets are observed on either side of the center. The elliptical pocket is enlarged in the constant energy contour plot at $-50$ meV binding energy indicative of the associated hole-like bands. On the other hand, the circularly pockets are slightly reduced in size, indicative of the associated electron bands. The calculated FS and $-50$ meV energy contours, presented in Figure 6.9(b), show reasonable resemblance to the experimental observation of elliptical and circular pockets. In Figure 6.9(c), we focus on one of the identical circular pockets (enclosed in dashed rectangle). First, at the $-65$ meV binding energy, the pocked is reduced to almost a point-like feature. At higher binding energies of $-120$ meV and $-150$ meV, the point-like feature again enlarges into a circular one.

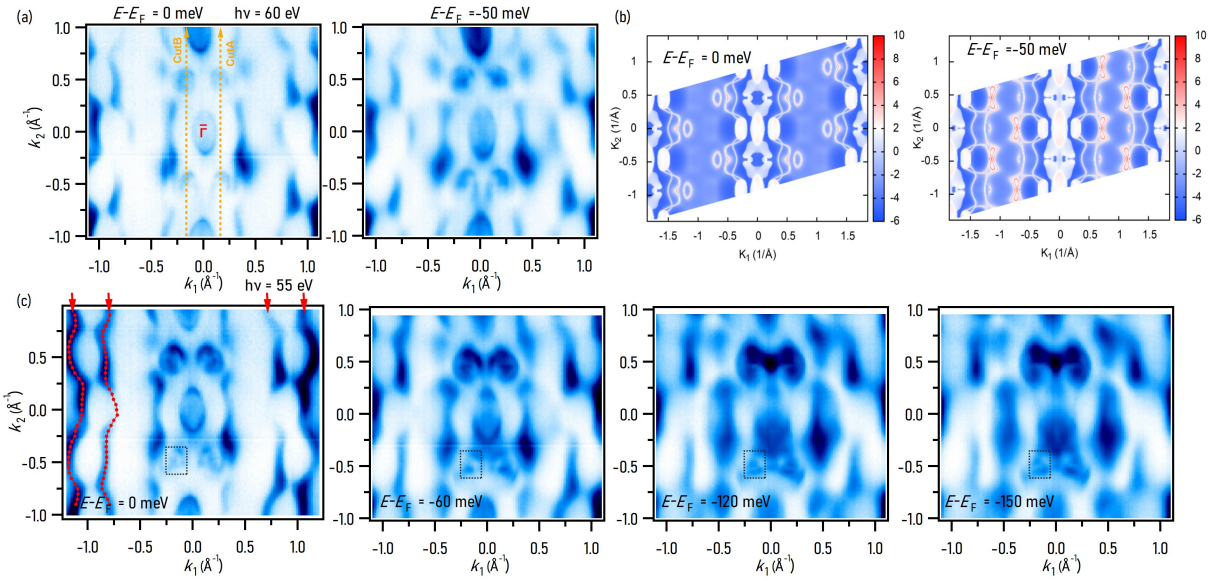


Figure 6.9: FS and constant energy contours. (a) ARPES measured FS (left) and an energy contour at $-50$ meV binding energy (right) using a photon energy of $60$ eV. (b)Calculated FS (left) and $-50$ meV constant energy contour (right). (c) Experimental FS (leftmost) and constant energy contours at noted binding energies measured using a photon energy of $55$ eV. The red markers on the FS trace the open FS features extending along $k_2$ direction.

This observation is consistent with a possible band crossing. In order to look for such crossing, we took cuts along two different directions labeled CutA and CutB in Figure 6.9(a). The resulting dispersion maps are shown in Figure 6.10. In the dispersion map along the CutA direction, two linear crossing-like features can be detected (pointed by arrow in Figure 6.10(a)). The DFT surface simulation along this direction also produces a reasonably agreeing bands. The bands producing the linear crossing-type feature seem to have bulk origin and are trivial in nature. A zoomed in dispesion map along the CutB direction shows similar crossing feature, well reproduced by DFT surface spectrum.

In Figure 6.11, we present more dispersion maps along the Cut1 $\rightarrow$ Cut5 directions as represented in the FS in Figure 6.11(a). From the dispersion map along Cut1, we can see a hole band crossing the Fermi level around the center of BZ and an electron pocket hanging below the Fermi level

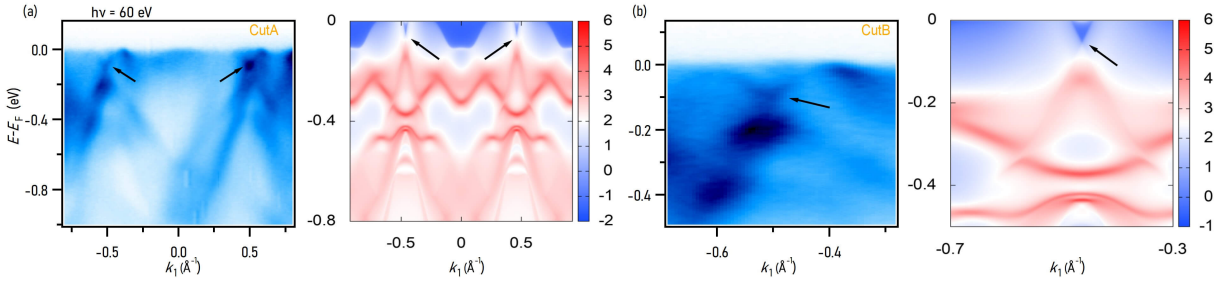


Figure 6.10: Linear crossing-like features at generic momentum directions. (a) Dispersion map along CutA direction as represented by orange dashed line in Figure 6.9(a) and calculated surface spectrum along this direction. (b) Dispersion map and calculated surface spectrum along CutB direction as represented in Figure 6.9(a).

away from the center on either sides. On moving away from the $\mathrm{Cut1}$ direction towards $\mathrm{Cut2}$, a linear crossing feature appears at the $k_1 = 0$ (represented by red dashed lines). The linear feature disappears in $\mathrm{Cut3}$ dispersion map and a gap appears at the position of the crossing point. $\mathrm{Cut4}$ and $\mathrm{Cut5}$ represent identical directions to $\mathrm{Cut3}$ and $\mathrm{Cut2}$, respectively in the next BZ. The linear crossing feature is confirmed by the dispersion map along $\mathrm{Cut5}$ as well. Figure 6.11(c) represents a $\mathrm{Cut1}$ direction dispersion map at a different photon energy of $55$ eV. Overall the band structure is similar to that observed along $\mathrm{Cut1}$ with $60$ eV photon energy in Figure 6.11(b). DFT calculation of the surface spectrum shows reasonable agreement with the experimental dispersion map (Figure 6.11(d)). The comparison indicates that the bands observed in the experimental maps seem to be coming from the bulk. Therefore, no Dirac-like surface states are observed on the $(\bar{2}01)$ surface. This is expected as the $(\bar{2}01)$ surface does not preserve the $C_2$ symmetry that is predicted to protect a Dirac surface state on the $(010)$ surface leading to a topological crystalline insulator state in $\mathrm{TaAs_2}$. This indicates $(\bar{2}01)$ surface of $\mathrm{TaAs_2}$ is topologically dark.

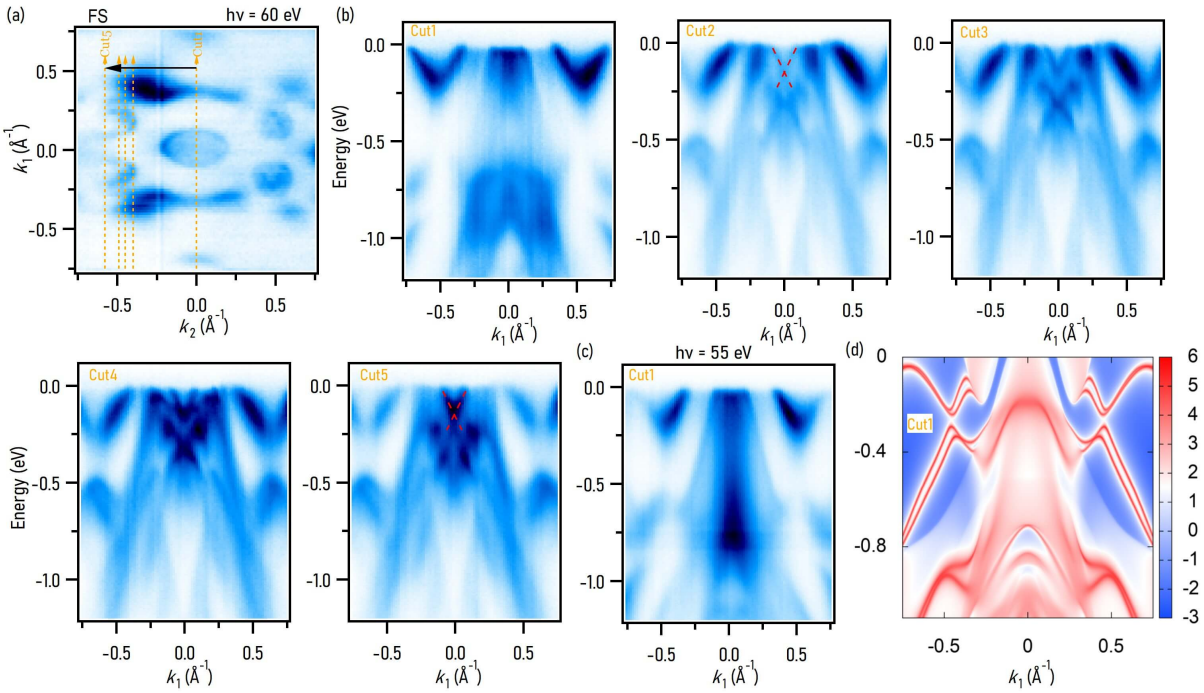


Figure 6.11: Cuts along different directions. (a) FS at $60$ eV photon energy showing different cut directions, Cut1 $\rightarrow$ Cut5. (b) Cuts along the directions shown in the FS in (a). (c) Cut1 dispersion map measured with $55$ eV photon energy. (d) Calculated surface spectrum along Cut1 direction.

## Conclusions

To conclude, by means of ARPES measurements and supported by DFT computations, transport, and magneto-transport measurements, we investigated electronic properties of a rotational topological crystalline insulator candidate $TaAs_2$. Since the rotational symmetry is preserved by the $(010)$, Dirac surface states are expected to be protected only on this surface. $TaAs_2$ crystals cleave with the preferred $(\bar{2}01)$ plane, which does not respect the rotational symmetry. As expected, our experimental results show metallic FS and multiple linear crossing features, which are coming from the trivial bulk bands, demonstrating $(\bar{2}01)$ to be topologically dark. Our magneto-transport results show very large and unsaturating MR. The presence of unclosed FS features observed in

our experimental FS may indicate towards possible role of open-orbit fermiology on such large MR property, which has been reported in isostructural TMDs $MoAs_2$ [279] and $NbAs_2$ [295].

## Experimental and computational methods

### *Sample growth and characterization*

Single crystals of $TaAs_2$ were synthesized by using $1:2$ molar ratio of elemental $Ta$ and high-purity $As$ placed in two different alumina crucibles and grown in a temperature gradient of $900\ ^\circ C$ at the source and $850\ ^\circ C$ at the sink for $7\ days$. Iodine (concentration of $2\ mg - cm^{-3}$) was used as a growth agent. The chemical composition and crystal structure of the samples were characterized by using energy-dispersive X-ray spectroscopy and powder X-ray diffraction measurements, respectively. For energy-dispersive X-ray spectroscopic measurements, FEI scanning electron microscope equipped with an EDAX Genesis XM4 spectrometer was utilized. $Mo\ K\alpha$ radiation was used for the powder X-ray diffraction measurements, and the measurements were carried out on a Kuma-Diffraction KM4 four-circle X-ray diffractometer with a CCD camera was utilized.

### *Transport and magneto-transport measurements*

Resistivity and magnetoresistance measurements were carried out in a Quantum Design PPMS system using four-probe contact method (excitation current of $3\ mA$; frequency $57.9\ Hz$) with $Au$ contacts placed on the sample using silver epoxy. Resistivity measurements were done within the temperature range of $2\ K - 250\ K$ and the magnetoresistance measurements were done at a temperature of $1.8\ K$ in magnetic field of strength up to $9\ T$.

*First-principles calculations*

DFT [169, 170]-based first-principles calculations were implemented in VASP software [173, 174] making use of PAW potential [171, 172] and GGA approximation of PBE-type [175]. $\Gamma$-centered $12 \times 12 \times 8\, k-mesh$ was employed for BZ integration and an energy cut-off of $350\ \mathrm{eV}$ was used for plane-wave basis set.

*ARPES measurements*

ARPES measurements were performed using the synchrotron light source available at the ALS BL 10.0.1.1 in Berkeley National Laboratory. The angular and energy resolutions were set better than $0.2^{\circ}$ and $20\ \mathrm{meV}$, respectively for the ARPES measurements. Flat samples prepared on copper posts, with ceramic post mounted on top using silver epoxy, were loaded into the ARPES chamber maintained at ultra-high vacuum better than $10^{-10}$ torr and then cleaved in-situ. Experiments were conducted at a temperature of $18\ \mathrm{K}$.

# APPENDIX A: LIST OF PUBLICATIONS AND PREPRINTS

1. **Sabin Regmi**, Robert Smith, Anup Pradhan Sakhya, Milo X. Sprague, Mazharul Islam Mondal, Iftakhar Bin Elius, Nathan Valadez, Andrzej Ptok, Dariusz Kaczorowski, and Madhab Neupane, Observation of gapless nodal-line states in $\mathrm{NdSbTe}$, Under review, preprint at arXiv:2210.00163.

2. **Sabin Regmi**, Tharindu Warnakulasooriya Fernando, Yuzhou Zhao, Anup Pradhan Sakhya, Gyanendra Dhakal, Iftakhar Bin Elius, Hector Vazquez, Jonathan D Denlinger, Jihui Yang, Jiun-Haw Chu, Xiaodong Xu, Ting Cao, and Madhab Neupane, Spectroscopic evidence of flat bands in breathing kagome semiconductor $\mathrm{Nb_3I_8}$, accepted for publication in Communications Materials (2022), preprint at arXiv:2203.10547.

3. **Sabin Regmi**, Gyanendra Dhakal, Fairoja Cheenicode Kabeer, Neil Harrison, Firoza Kabir, Anup Pradhan Sakhya, Krzysztof Gofryk, Dariusz Kaczorowski, Peter M. Oppeneer, and Madhab Neupane, Observation of multiple nodal lines in $\mathrm{SmSbTe}$, Physical Reviews Materials **6**, L031201 (2022).

4. **Sabin Regmi**, M. Mofazzel Hosen, Barun Ghosh, Bahadur Singh, Gyanendra Dhakal, Christopher Sims, Baokai Wang, Firoza Kabir, Klauss Dimitri, Yangyang Liu, Amit Agarwal, Hsin Lin, Dariusz Kaczorowski, Arun Bansil, and Madhab Neupane, Temperature-dependent electronic structure in a higher-order topological insulator candidate $\mathrm{EuIn_2As_2}$, Physical Reviews B **102**, 165153 (2020).

5. Yangyang Liu, Gyanendra Dhakal, Anup Pradhan Sakhya, John E. Beetar, Firoza Kabir, **Sabin Regmi**, Dariusz Kaczorowski, Michael Chini, Benjamin M Fregoso, and Madhab Neupane, Ultrafast relaxation of acoustic and optical phonons in a topological nodal-line semimetal $\mathrm{ZrSiS}$, Communications Physics **5**, 203 (2022).

6. Gyanendra Dhakal, Firoza Kabir, Ashis K. Nandy, Alex Aperis, Anup Pradhan Sakhya, Subhadip Pradhan, Klauss Dimitri, Christopher Sims, **Sabin Regmi**, M. Mofazzel Hosen,

Yangyang Liu, Luis Persaud, Dariusz Kaczorowski, Peter M. Oppeneer, and Madhab Neupane, Observation of anisotropic Dirac cones in the topological material $Ti_2Te_2P$, Phys. Rev. B **106**, 125124 (2022).

7. Firoza Kabir, Randall Filippone, Gyanendra Dhakal, Y Lee, Narayan Poudel, Jacob Casey, Anup Pradhan Sakhya, **Sabin Regmi**, Robert Smith, Pietro Manfrinetti, Liqin Ke, Krzysztof Gofryk, Madhab Neupane, and Arjun K. Pathak, Unusual magnetic and transport properties in $HoMn_6Sn_6$ kagome magnet, Physical Review Materials **6**, 064404 (2022).

8. Anup Pradhan Sakhya, Baokai Wang, Firoza Kabir, Cheng-Yi Huang, M Mofazzel Hosen, Bahadur Singh, **Sabin Regmi**, Gyanendra Dhakal, Klauss Dimitri, Milo Sprague, Robert Smith, Eric D. Bauer, Filip Ronning, Arun Bansil, and Madhab Neupane, Complex electronic structure evolution of $NdSb$ across the magnetic transition, accepted for publication in Physical Review B (2022), preprint at arXiv:2203.05879.

9. Anup Pradhan Sakhya, Cheng-Yi Huang, Gyanendra Dhakal, Xue-Jian Gao, **Sabin Regmi**, Xiaohan Yao, Robert Smith, Milo Sprague, Bahadur Singh, Hsin Lin, Su-Yang Xu, Fazel Tafti, Arun Bansil, and Madhab Neupane, Observation of Fermi arcs and Weyl nodes in a non-centrosymmetric magnetic Weyl semimetal, under review, preprint at arXiv:2203.05440.

10. Firoza Kabir, M. Mofazzel Hosen, Xiaxin Ding, Christopher Lane, Gyanendra Dhakal, Yangyang Liu, Klauss Dimitri, Christopher Sims, **Sabin Regmi**, Anup Pradhan Sakhya, Luis Persaud, John E. Beetar, Yong Liu, Michael Chini, Arjun K. Pathak, Jian-Xin Zhu, Krzysztof Gofryk, and Madhab Neupane, Effect of Dilute Magnetism in a Topological Insulator, Frontiers in Materials **8**, 706658 (2021).

11. Gyanendra Dhakal, M. Mofazzel Hosen, Wei-Chi Chiu, Bahadur Singh, Cheng-Yi Huang, Klauss Dimitri, Baokai Wang, Firoza Kabir, Christopher Sims, **Sabin Regmi**, William Neff, Jonathan Denlinger, Hsin Lin, Dariusz Kaczorowski, Arun Bansil, and Madhab Neupane,

Cleaving plane-dependent electronic structures of transition metal diarsenides, Physical Reviews Research , 023170 (2021).

12. Gyanendra Dhakal, Fairoja Cheenicode Kabeer, Arjun K. Pathak, Firoza Kabir, Narayan Poudel, Randall Filippone, Jacob Casey, Anup Pradhan Sakhya, **Sabin Regmi**, Christopher Sims, Klauss Dimitri, Pietro Manfrinetti, Krzysztof Gofryk, Peter M. Oppeneer, and Madhab Neupane, Anisotropically large anomalous and topological Hall effect in a kagome magnet, Physical Reviews B **104**, L161115 (2021).

13. Christopher Sims, M. Mofazzel Hosen, Hugo Aramberri, Cheng-Yi Huang, Gyanendra Dhakal, Klauss Dimitri, Firoza Kabir, **Sabin Regmi**, Xiaoting Zhou, Tay-Rong Chang, Hsin Lin, Dariusz Kaczorowski, Nicholas Kioussis, and Madhab Neupane, Termination-dependent topological surface states in nodal-loop semimetal $HfP_2$, Physical Reviews Materials **4**, 054201 (2020).

14. Yangyang Liu, John E. Beetar, Md Mofazzel Hosen, Gyanendra Dhakal, Christopher Sims, Firoza Kabir, Marc B. Etienne, Klauss Dimitri, **Sabin Regmi**, Yong Liu, Arjun K. Pathak, Dariusz Kaczorowski, Madhab Neupane, and Michael Chini, Extreme ultraviolet time- and angle-resolved photoemission setup with 21.5 meV resolution using high-order harmonic generation from a turn-key Yb:KGW amplifier, Review of Scientific Instruments **91**, 013102 (2020).

15. M. Mofazzel Hosen, Gyanendra Dhakal, Baokai Wang, Narayan Poudel, Bahadur Singh, Klauss Dimitri, Firoza Kabir, Christopher Sims, **Sabin Regmi**, William Neff, Anan Bari Sarkar, Amit Agarwal, Daniel Murray, Franziska Weickert, Krzysztof Gofryk, Orest Pavlosiuk, Piotr Wiśniewski, Dariusz Kaczorowski, Arun Bansil, and Madhab Neupane, Observation of gapped state in rare-earth monopnictide $HoSb$, Scientific Reports **10**, 12961 (2020).

16. M. Mofazzel Hosen, Gyanendra Dhakal, Baokai Wang, Narayan Poudel, Klauss Dimitri,

Firoza Kabir, Christopher Sims, **Sabin Regmi**, Krzysztof Gofryk, Dariusz Kaczorowski, Arun Bansil, and Madhab Neupane, Experimental observation of drumhead surface states in $SrAs_3$, Scientific Reports **10**, 2776 (2020).

17. Firoza Kabir, M Mofazzel Hosen, Fairoja Cheenicode Kabeer, Alex Aperis, Xiaxin Ding, Gyanendra Dhakal, Klauss Dimitri, Christopher Sims, **Sabin Regmi**, Luis Persaud, Krzysztof Gofryk, Peter M. Oppeneer, Dariusz Kaczorowski, and Madhab Neupane, Observation of multiple Dirac states in a magnetic topological material $EuMg_2Bi_2$, preprint at arXiv:1912.08645.

18. Gyanendra Dhakal, M Mofazzel Hosen, Ayana Ghosh, Christopher Lane, Karolina Górnicka, Michal J Winiarski, Klauss Dimitri, Firoza Kabir, Christopher Sims, **Sabin Regmi**, William Neff, Luis Persaud, Yangyang Liu, Dariusz Kaczorowski, Jian-Xin Zhu, Tomasz Klimczuk, and Madhab Neupane, Observation of topological surface state in a superconducting material, Under review, preprint at arXiv:1911.08519.

# APPENDIX B: LIST OF PRESENTATIONS

1. Contributed talk at the *Association of Nepali Physicists in America (ANPA) Conference 2022*; Title: "**Observation of multiple nodal lines in SmSbTe**", 15 July 2022.

2. Poster presentation at the *2022 Annual Symposium, Florida Chapter of the AVS Science and Technology Society, Orlando, Florida*; Title: "**Observation of multiple nodal lines in SmSbTe**", 05 May 2022.

3. Poster presentation at the *2022 Student Scholar Symposium, University of Central Florida, Orlando, Florida*; Title: "**Observation of multiple nodal lines in SmSbTe**", 31 March 2022.

4. Contributed talk at the *APS March Meeting 2022, Chicago, Illinois*; Title: "**Observation of multiple nodal lines in SmSbTe**", 17 March 2022.

5. Contributed talk at the *International Conference on Strongly Correlated Electron Systems, Brazil (Online)*; Title: "**Temperature-dependent electronic structure in a higher-order topological insulator candidate $EuIn_2As_2$**", 27 September 2021.

6. Poster presentation at the *2021 ALS User Meeting (Online)*; Title: "**Temperature-dependent electronic structure in a higher-order topological insulator candidate $EuIn_2As_2$**", 10 August 2021.

7. Contributed talk at the *APS March Meeting 2021 (Virtual)*; Title: "**Temperature-dependent electronic structure in a higher-order topological insulator candidate $EuIn_2As_2$**", 16 March 2021.

8. Poster presentation at the *2021 Student Scholar Symposium, University of Central Florida, Orlando, Florida*; Title: "**Temperature-dependent electronic structure in a higher-order topological insulator candidate $EuIn_2As_2$**", 01 April 2021.

9. Contributed talk at the *Association of Nepali Physicists in America (ANPA) conference 2020 (Online)*; Title: "**Temperature-dependent electronic structure in a higher-order topological insulator candidate $EuIn_2As_2$**", 19 July 2020.

10. Poster presentation at the *2020 Annual symposium, Florida chapter of the AVS science and technology society, Orlando, Florida*; Title: "**Dirac state switching in transition metal diarsenides**", 09 March 2020.

11. Poster presentation at the *APS March Meeting 2020, Denver, Colorado*; Title: "**Dirac state switching in transition metal diarsenides**", Scheduled for 03 March 2020 (Canceled). (Contributed talk at the *Mini March Meeting 2020 organized by Department of Physics, University of Central Florida* as an alternative to canceled APS March meeting 2020.)

12. Poster presentation at the *APS March Meeting 2019, Boston, Massachusetts*; Title: "**Discovery of topological nodal-line fermionic phase in a magnetic material GdSbTe**", 07 March 2019.

# LIST OF REFERENCES


[1] K. v. Klitzing, G. Dorda, and M. Pepper, New Method for High-Accuracy Determination of the Fine-Structure Constant Based on Quantized Hall Resistance, Phys. Rev. Lett. **45**, 494 (1980).

[2] K. v. Klitzing, The quantized Hall effect, Rev. Mod. Phys. **58**, 519 (1986).

[3] M. Z. Hasan and C. L. Kane, Colloquium: Topological insulators, Rev. Mod. Phys. **82**, 3045 (2010).

[4] X.-L. Qi and S.-C. Zhang, Topological insulators and superconductors, Rev. Mod. Phys. **83**, 1057 (2011).

[5] N. P. Armitage, E. J. Mele, and A. Vishwanath, Weyl and Dirac semimetals in three-dimensional solids, Rev. Mod. Phys. **90**, 015001 (2018).

[6] B. Yan and C. Felser, Topological Materials: Weyl Semimetals, Annu. Rev. Condens. Matter Phys. **8**, 337 (2017).

[7] A. A. Burkov, M. D. Hook, and L. Balents, Topological nodal semimetals, Phys. Rev. B **84**, 235126 (2011).

[8] M. Sato and Y. Ando, Topological superconductors: a review, Rep. Prog. Phys. **80**, 076501 (2017).

[9] E. H. Hall, On a New Action of the Magnet on Electric Currents, American Journal of Mathematics **2**, 287 (1879).

[10] E. H. Hall, XVIII. On the "Rotational Coefficient" in nickel and cobalt, The London, Edinburgh, and Dublin Philosophical Magazine and Journal of Science **12**, 157 (1881).

[11] E. M. Pugh and N. Rostoker, Hall Effect in Ferromagnetic Materials, Rev. Mod. Phys. **25**, 151 (1953).

[12] N. Nagaosa, J. Sinova, S. Onoda, A. H. MacDonald, and N. P. Ong, Anomalous Hall effect, Rev. Mod. Phys. **82**, 1539 (2010).

[13] D. J. Thouless, M. Kohmoto, M. P. Nightingale, and M. den Nijs, Quantized Hall Conductance in a Two-Dimensional Periodic Potential, Phys. Rev. Lett. **49**, 405 (1982).

[14] B. I. Halperin, Quantized Hall conductance, current-carrying edge states, and the existence of extended states in a two-dimensional disordered potential, Phys. Rev. B **25**, 2185 (1982).

[15] C. L. Kane and E. J. Mele, Quantum Spin Hall Effect in Graphene, Phys. Rev. Lett. **95**, 226801 (2005).

[16] B. A. Bernevig and S.-C. Zhang, Quantum Spin Hall Effect, Phys. Rev. Lett. **96**, 106802 (2006).

[17] F. D. M. Haldane, Model for a Quantum Hall Effect without Landau Levels: Condensed-Matter Realization of the "Parity Anomaly", Phys. Rev. Lett. **61**, 2015 (1988).

[18] M. König, S. Wiedmann, C. Brüne, A. Roth, H. Buhmann, W. Molenkamp Laurens, X.-L. Qi, and S.-C. Zhang, Quantum Spin Hall Insulator State in HgTe Quantum Wells, Science **318**, 766 (2007).

[19] B. A. Bernevig, L. Hughes Taylor, and S.-C. Zhang, Quantum Spin Hall Effect and Topological Phase Transition in HgTe Quantum Wells, Science **314**, 1757 (2006).

[20] C. L. Kane and E. J. Mele, $Z_2$ Topological Order and the Quantum Spin Hall Effect, Phys. Rev. Lett. **95**, 146802 (2005).

[21] L. Fu, C. L. Kane, and E. J. Mele, Topological Insulators in Three Dimensions, Phys. Rev. Lett. **98**, 106803 (2007).

[22] H. A. Kramers, Théorie générale de la rotation paramagnétique dans les cristaux, Proc. Acad. Amst **33**, 959 (1930).

[23] L. Fu and C. L. Kane, Topological insulators with inversion symmetry, Phys. Rev. B **76**, 045302 (2007).

[24] J. E. Moore and L. Balents, Topological invariants of time-reversal-invariant band structures, Phys. Rev. B **75**, 121306 (2007).

[25] A. Bansil, H. Lin, and T. Das, Colloquium: Topological band theory, Rev. Mod. Phys. **88**, 021004 (2016).

[26] D. Hsieh, D. Qian, L. Wray, Y. Xia, Y. S. Hor, R. J. Cava, and M. Z. Hasan, A topological Dirac insulator in a quantum spin Hall phase, Nature **452**, 970 (2008).

[27] Y. Xia, D. Qian, D. Hsieh, L. Wray, A. Pal, H. Lin, A. Bansil, D. Grauer, Y. S. Hor, R. J. Cava, and M. Z. Hasan, Observation of a large-gap topological-insulator class with a single Dirac cone on the surface, Nat. Phys. **5**, 398 (2009).

[28] H. Zhang, C.-X. Liu, X.-L. Qi, X. Dai, Z. Fang, and S.-C. Zhang, Topological insulators in $Bi_2Se_3$, $Bi_2Te_3$ and $Sb_2Te_3$ with a single Dirac cone on the surface, Nat. Phys. **5**, 438 (2009).

[29] Y. L. Chen, J. H. Chu, J. G. Analytis, Z. K. Liu, K. Igarashi, H. H. Kuo, X. L. Qi, S. K. Mo, R. G. Moore, D. H. Lu, M. Hashimoto, T. Sasagawa, S. C. Zhang, I. R. Fisher, Z. Hussain, and Z. X. Shen, Massive Dirac Fermion on the Surface of a Magnetically Doped Topological Insulator, Science **329**, 659 (2010).

[30] L. A. Wray, S.-Y. Xu, Y. Xia, D. Hsieh, A. V. Fedorov, Y. S. Hor, R. J. Cava, A. Bansil, H. Lin, and M. Z. Hasan, A topological insulator surface under strong Coulomb, magnetic and disorder perturbations, Nat. Phys. **7**, 32 (2011).

[31] A. M. Essin, J. E. Moore, and D. Vanderbilt, Magnetoelectric Polarizability and Axion Electrodynamics in Crystalline Insulators, Phys. Rev. Lett. **102**, 146805 (2009).

[32] R. S. K. Mong, A. M. Essin, and J. E. Moore, Antiferromagnetic topological insulators, Phys. Rev. B **81**, 245209 (2010).

[33] C.-Z. Chang, J. Zhang, X. Feng, J. Shen, Z. Zhang, M. Guo, K. Li, Y. Ou, P. Wei, L.-L. Wang, Z.-Q. Ji, Y. Feng, S. Ji, X. Chen, J. Jia, X. Dai, Z. Fang, S.-C. Zhang, K. He, Y. Wang, L. Lu, X.-C. Ma, and Q.-K. Xue, Experimental Observation of the Quantum Anomalous Hall Effect in a Magnetic Topological Insulator, Science **340**, 167 (2013).

[34] Y. Tokura, K. Yasuda, and A. Tsukazaki, Magnetic topological insulators, Nat. Rev. Phys. **1**, 126 (2019).

[35] R. Noguchi, T. Takahashi, K. Kuroda, M. Ochi, T. Shirasawa, M. Sakano, C. Bareille, M. Nakayama, M. D. Watson, K. Yaji, A. Harasawa, H. Iwasawa, P. Dudin, T. K. Kim, M. Hoesch, V. Kandyba, A. Giampietri, A. Barinov, S. Shin, R. Arita, T. Sasagawa, and T. Kondo, A weak topological insulator state in quasi-one-dimensional bismuth iodide, Nature **566**, 518 (2019).

[36] L. Fu, Topological Crystalline Insulators, Phys. Rev. Lett. **106**, 106802 (2011).

[37] T. H. Hsieh, H. Lin, J. Liu, W. Duan, A. Bansil, and L. Fu, Topological crystalline insulators in the $\mathrm{SnTe}$ material class, Nat. Commun. **3**, 982 (2012).

[38] Y. Tanaka, Z. Ren, T. Sato, K. Nakayama, S. Souma, T. Takahashi, K. Segawa, and Y. Ando, Experimental realization of a topological crystalline insulator in $\mathrm{SnTe}$, Nat. Phys. **8**, 800 (2012).

[39] Z. K. Liu, B. Zhou, Y. Zhang, Z. J. Wang, H. M. Weng, D. Prabhakaran, S. K. Mo, Z. X. Shen, Z. Fang, X. Dai, Z. Hussain, and Y. L. Chen, Discovery of a Three-Dimensional Topological Dirac Semimetal, $\mathrm{Na_3Bi}$, Science **343**, 864 (2014).

[40] M. Neupane, S.-Y. Xu, R. Sankar, N. Alidoust, G. Bian, C. Liu, I. Belopolski, T.-R. Chang, H.-T. Jeng, H. Lin, A. Bansil, F. Chou, and M. Z. Hasan, Observation of a three-dimensional topological Dirac semimetal phase in high-mobility $\mathrm{Cd_3As_2}$, Nat. Commun. **5**, 3786 (2014).

[41] S. Borisenko, Q. Gibson, D. Evtushinsky, V. Zabolotnyy, B. Büchner, and R. J. Cava, Experimental Realization of a Three-Dimensional Dirac Semimetal, Phys. Rev. Lett. **113**, 027603 (2014).

[42] S.-Y. Xu, I. Belopolski, N. Alidoust, M. Neupane, G. Bian, C. Zhang, R. Sankar, G. Chang, Z. Yuan, C.-C. Lee, S.-M. Huang, H. Zheng, J. Ma, S. Sanchez Daniel, B. Wang, A. Bansil, F. Chou, P. Shibayev Pavel, H. Lin, S. Jia, and M. Z. Hasan, Discovery of a Weyl fermion semimetal and topological Fermi arcs, Science **349**, 613 (2015).

[43] B. Q. Lv, N. Xu, H. M. Weng, J. Z. Ma, P. Richard, X. C. Huang, L. X. Zhao, G. F. Chen, C. E. Matt, F. Bisti, V. N. Strocov, J. Mesot, Z. Fang, X. Dai, T. Qian, M. Shi, and H. Ding, Observation of Weyl nodes in TaAs, Nat. Phys. **11**, 724 (2015).

[44] G. Bian, T.-R. Chang, R. Sankar, S.-Y. Xu, H. Zheng, T. Neupert, C.-K. Chiu, S.-M. Huang, G. Chang, I. Belopolski, D. S. Sanchez, M. Neupane, N. Alidoust, C. Liu, B. Wang, C.-C. Lee, H.-T. Jeng, C. Zhang, Z. Yuan, S. Jia, A. Bansil, F. Chou, H. Lin, and M. Z. Hasan, Topological nodal-line fermions in spin-orbit metal $\mathrm{PbTaSe_2}$, Nat. Commun. **7**, 10556 (2016).

[45] M. Neupane, I. Belopolski, M. M. Hosen, D. S. Sanchez, R. Sankar, M. Szlawska, S.-Y. Xu, K. Dimitri, N. Dhakal, P. Maldonado, P. M. Oppeneer, D. Kaczorowski, F. Chou, M. Z. Hasan, and T. Durakiewicz, Observation of topological nodal fermion semimetal phase in $\mathrm{ZrSiS}$, Phys. Rev. B **93**, 201104 (2016).

[46] L. M. Schoop, M. N. Ali, C. Straßer, A. Topp, A. Varykhalov, D. Marchenko, V. Duppel, S. S. P. Parkin, B. V. Lotsch, and C. R. Ast, Dirac cone protected by non-symmorphic symmetry and three-dimensional Dirac line node in $\mathrm{ZrSiS}$, Nat. Commun. **7**, 11696 (2016).

[47] X. Wan, A. M. Turner, A. Vishwanath, and S. Y. Savrasov, Topological semimetal and Fermi-arc surface states in the electronic structure of pyrochlore iridates, Phys. Rev. B **83**, 205101 (2011).

[48] A. A. Soluyanov, D. Gresch, Z. Wang, Q. Wu, M. Troyer, X. Dai, and B. A. Bernevig, Type-II Weyl semimetals, Nature **527**, 495 (2015).

[49] I. Belopolski, D. S. Sanchez, Y. Ishida, X. Pan, P. Yu, S.-Y. Xu, G. Chang, T.-R. Chang, H. Zheng, N. Alidoust, G. Bian, M. Neupane, S.-M. Huang, C.-C. Lee, Y. Song, H. Bu, G. Wang, S. Li, G. Eda, H.-T. Jeng, T. Kondo, H. Lin, Z. Liu, F. Song, S. Shin, and M. Z. Hasan, Discovery of a new type of topological Weyl fermion semimetal state in $\mathrm{Mo}_x\mathrm{W}_{1-x}\mathrm{Te}_2$, Nat. Commun. **7**, 13643 (2016).

[50] S.-Y. Xu, N. Alidoust, G. Chang, H. Lu, B. Singh, I. Belopolski, S. Sanchez Daniel, X. Zhang, G. Bian, H. Zheng, M.-A. Husanu, Y. Bian, S.-M. Huang, C.-H. Hsu, T.-R. Chang, H.-T. Jeng, A. Bansil, T. Neupert, N. Strocov Vladimir, H. Lin, S. Jia, and M. Z. Hasan, Discovery of Lorentz-violating type II Weyl fermions in $\mathrm{LaAlGe}$, Sci. Adv. **3**, e1603266 (2017).

[51] T.-R. Chang, S.-Y. Xu, D. S. Sanchez, W.-F. Tsai, S.-M. Huang, G. Chang, C.-H. Hsu, G. Bian, I. Belopolski, Z.-M. Yu, S. A. Yang, T. Neupert, H.-T. Jeng, H. Lin, and M. Z. Hasan,

Type-II Symmetry-Protected Topological Dirac Semimetals, Phys. Rev. Lett. **119**, 026404 (2017).

[52] J. Jiang, Z. K. Liu, Y. Sun, H. F. Yang, C. R. Rajamathi, Y. P. Qi, L. X. Yang, C. Chen, H. Peng, C. C. Hwang, S. Z. Sun, S. K. Mo, I. Vobornik, J. Fujii, S. S. P. Parkin, C. Felser, B. H. Yan, and Y. L. Chen, Signature of type-II Weyl semimetal phase in $\mathrm{MoTe_2}$, Nat. Commun. **8**, 13973 (2017).

[53] B. Bradlyn, J. Cano, Z. Wang, M. G. Vergniory, C. Felser, R. J. Cava, and B. A. Bernevig, Beyond Dirac and Weyl fermions: Unconventional quasiparticles in conventional crystals, Science **353**, aaf5037 (2016).

[54] Z. Zhu, G. W. Winkler, Q. Wu, J. Li, and A. A. Soluyanov, Triple Point Topological Metals, Phys. Rev. X **6**, 031003 (2016).

[55] G. Chang, S.-Y. Xu, B. J. Wieder, D. S. Sanchez, S.-M. Huang, I. Belopolski, T.-R. Chang, S. Zhang, A. Bansil, H. Lin, and M. Z. Hasan, Unconventional Chiral Fermions and Large Topological Fermi Arcs in $\mathrm{RhSi}$, Phys. Rev. Lett. **119**, 206401 (2017).

[56] D. A. Pshenay-Severin, Y. V. Ivanov, A. A. Burkov, and A. T. Burkov, Band structure and unconventional electronic topology of $\mathrm{CoSi}$, J. Phys. Condens. Mater. **30**, 135501 (2018).

[57] D. Takane, Z. Wang, S. Souma, K. Nakayama, T. Nakamura, H. Oinuma, Y. Nakata, H. Iwasawa, C. Cacho, T. Kim, K. Horiba, H. Kumigashira, T. Takahashi, Y. Ando, and T. Sato, Observation of Chiral Fermions with a Large Topological Charge and Associated Fermi-Arc Surface States in $\mathrm{CoSi}$, Phys. Rev. Lett. **122**, 076402 (2019).

[58] Z. Rao, H. Li, T. Zhang, S. Tian, C. Li, B. Fu, C. Tang, L. Wang, Z. Li, W. Fan, J. Li, Y. Huang, Z. Liu, Y. Long, C. Fang, H. Weng, Y. Shi, H. Lei, Y. Sun, T. Qian, and H. Ding,

Observation of unconventional chiral fermions with long Fermi arcs in $\mathrm{CoSi}$, Nature **567**, 496 (2019).

[59] D. S. Sanchez, I. Belopolski, T. A. Cochran, X. Xu, J.-X. Yin, G. Chang, W. Xie, K. Manna, V. Süß, C.-Y. Huang, N. Alidoust, D. Multer, S. S. Zhang, N. Shumiya, X. Wang, G.-Q. Wang, T.-R. Chang, C. Felser, S.-Y. Xu, S. Jia, H. Lin, and M. Z. Hasan, Topological chiral crystals with helicoid-arc quantum states, Nature **567**, 500 (2019).

[60] C. Fang, H. Weng, X. Dai, and Z. Fang, Topological nodal line semimetals, Chinese Phys. B **25**, 117106 (2016).

[61] S.-Y. Yang, H. Yang, E. Derunova, S. S. P. Parkin, B. Yan, and M. N. Ali, Symmetry demanded topological nodal-line materials, Adv. Phys. X **3**, 1414631 (2018).

[62] H. Weng, Y. Liang, Q. Xu, R. Yu, Z. Fang, X. Dai, and Y. Kawazoe, Topological node-line semimetal in three-dimensional graphene networks, Phys. Rev. B **92**, 045108 (2015).

[63] G. Bian, T.-R. Chang, H. Zheng, S. Velury, S.-Y. Xu, T. Neupert, C.-K. Chiu, S.-M. Huang, D. S. Sanchez, I. Belopolski, N. Alidoust, P.-J. Chen, G. Chang, A. Bansil, H.-T. Jeng, H. Lin, and M. Z. Hasan, Drumhead surface states and topological nodal-line fermions in $\mathrm{TlTaSe_2}$, Phys. Rev. B **93**, 121113 (2016).

[64] Y. H. Chan, C.-K. Chiu, M. Y. Chou, and A. P. Schnyder, $\mathrm{Ca_3P_2}$ and other topological semimetals with line nodes and drumhead surface states, Phys. Rev. B **93**, 205132 (2016).

[65] N. B. Kopnin, T. T. Heikkilä, and G. E. Volovik, High-temperature surface superconductivity in topological flat-band systems, Phys. Rev. B **83**, 220503 (2011).

[66] T. T. Heikkilä, N. B. Kopnin, and G. E. Volovik, Flat bands in topological media, JETP Letters **94**, 233 (2011).

[67] Q. Xu, R. Yu, Z. Fang, X. Dai, and H. Weng, Topological nodal line semimetals in the $\mathrm{CaP_3}$ family of materials, Phys. Rev. B **95**, 045136 (2017).

[68] R. Yu, H. Weng, Z. Fang, X. Dai, and X. Hu, Topological Node-Line Semimetal and Dirac Semimetal State in Antiperovskite $\mathrm{Cu_3PdN}$, Phys. Rev. Lett. **115**, 036807 (2015).

[69] H. Weng, C. Fang, Z. Fang, B. A. Bernevig, and X. Dai, Weyl Semimetal Phase in Noncentrosymmetric Transition-Metal Monophosphides, Phys. Rev. X **5**, 011029 (2015).

[70] S.-M. Huang, S.-Y. Xu, I. Belopolski, C.-C. Lee, G. Chang, B. Wang, N. Alidoust, G. Bian, M. Neupane, C. Zhang, S. Jia, A. Bansil, H. Lin, and M. Z. Hasan, A Weyl Fermion semimetal with surface Fermi arcs in the transition metal monopnictide $\mathrm{TaAs}$ class, Nat. Commun. **6**, 7373 (2015).

[71] C. Chen, X. Xu, J. Jiang, S. C. Wu, Y. P. Qi, L. X. Yang, M. X. Wang, Y. Sun, N. B. M. Schröter, H. F. Yang, L. M. Schoop, Y. Y. Lv, J. Zhou, Y. B. Chen, S. H. Yao, M. H. Lu, Y. F. Chen, C. Felser, B. H. Yan, Z. K. Liu, and Y. L. Chen, Dirac line nodes and effect of spin-orbit coupling in the nonsymmorphic critical semimetals $M\mathrm{SiS}\,(M = \mathrm{Hf},\, \mathrm{Zr})$, Phys. Rev. B **95**, 125126 (2017).

[72] S. M. Young and C. L. Kane, Dirac Semimetals in Two Dimensions, Phys. Rev. Lett. **115**, 126803 (2015).

[73] W. A. Benalcazar, B. A. Bernevig, and T. L. Hughes, Electric multipole moments, topological multipole moment pumping, and chiral hinge states in crystalline insulators, Phys. Rev. B **96**, 245115 (2017).

[74] W. A. Benalcazar, B. A. Bernevig, and L. Hughes Taylor, Quantized electric multipole insulators, Science **357**, 61 (2017).

[75] F. Schindler, M. Cook Ashley, G. Vergniory Maia, Z. Wang, S. P. Parkin Stuart, B. A. Bernevig, and T. Neupert, Higher-order topological insulators, Sci. Adv. **4**, eaat0346 (2018).

[76] J. Langbehn, Y. Peng, L. Trifunovic, F. von Oppen, and P. W. Brouwer, Reflection-Symmetric Second-Order Topological Insulators and Superconductors, Phys. Rev. Lett. **119**, 246401 (2017).

[77] Z. Song, Z. Fang, and C. Fang, $(d-2)$-Dimensional Edge States of Rotation Symmetry Protected Topological States, Phys. Rev. Lett. **119**, 246402 (2017).

[78] M. Geier, L. Trifunovic, M. Hoskam, and P. W. Brouwer, Second-order topological insulators and superconductors with an order-two crystalline symmetry, Phys. Rev. B **97**, 205135 (2018).

[79] E. Khalaf, Higher-order topological insulators and superconductors protected by inversion symmetry, Phys. Rev. B **97**, 205136 (2018).

[80] S. Imhof, C. Berger, F. Bayer, J. Brehm, L. W. Molenkamp, T. Kiessling, F. Schindler, C. H. Lee, M. Greiter, T. Neupert, and R. Thomale, Topolectrical-circuit realization of topological corner modes, Nat. Phys. **14**, 925 (2018).

[81] C. W. Peterson, W. A. Benalcazar, T. L. Hughes, and G. Bahl, A quantized microwave quadrupole insulator with topologically protected corner states, Nature **555**, 346 (2018).

[82] M. Serra-Garcia, V. Peri, R. Süsstrunk, O. R. Bilal, T. Larsen, L. G. Villanueva, and S. D. Huber, Observation of a phononic quadrupole topological insulator, Nature **555**, 342 (2018).

[83] F. Schindler, Z. Wang, M. G. Vergniory, A. M. Cook, A. Murani, S. Sengupta, A. Y. Kasumov, R. Deblock, S. Jeon, I. Drozdov, H. Bouchiat, S. Guéron, A. Yazdani, B. A. Bernevig, and T. Neupert, Higher-order topology in bismuth, Nat. Phys. **14**, 918 (2018).

[84] H.-X. Wang, Z.-K. Lin, B. Jiang, G.-Y. Guo, and J.-H. Jiang, Higher-Order Weyl Semimetals, Phys. Rev. Lett. **125**, 146401 (2020).

[85] S. A. A. Ghorashi, T. Li, and T. L. Hughes, Higher-Order Weyl Semimetals, Phys. Rev. Lett. **125**, 266804 (2020).

[86] M. Ezawa, Higher-Order Topological Insulators and Semimetals on the Breathing Kagome and Pyrochlore Lattices, Phys. Rev. Lett. **120**, 026801 (2018).

[87] E. Edvardsson, F. K. Kunst, and E. J. Bergholtz, Non-Hermitian extensions of higher-order topological phases and their biorthogonal bulk-boundary correspondence, Phys. Rev. B **99**, 081302 (2019).

[88] T. Liu, Y.-R. Zhang, Q. Ai, Z. Gong, K. Kawabata, M. Ueda, and F. Nori, Second-Order Topological Phases in Non-Hermitian Systems, Phys. Rev. Lett. **122**, 076801 (2019).

[89] Y. Peng and G. Refael, Floquet Second-Order Topological Insulators from Nonsymmorphic Space-Time Symmetries, Phys. Rev. Lett. **123**, 016806 (2019).

[90] Z. Lin, J.-H. Choi, Q. Zhang, W. Qin, S. Yi, P. Wang, L. Li, Y. Wang, H. Zhang, Z. Sun, L. Wei, S. Zhang, T. Guo, Q. Lu, J.-H. Cho, C. Zeng, and Z. Zhang, Flatbands and Emergent Ferromagnetic Ordering in $Fe_3Sn_2$ Kagome Lattices, Phys. Rev. Lett. **121**, 096401 (2018).

[91] Z. Liu, M. Li, Q. Wang, G. Wang, C. Wen, K. Jiang, X. Lu, S. Yan, Y. Huang, D. Shen, J.-X. Yin, Z. Wang, Z. Yin, H. Lei, and S. Wang, Orbital-selective Dirac fermions and extremely flat bands in frustrated kagome-lattice metal $CoSn$, Nat. Commun. **11**, 4002 (2020).

[92] M. Kang, S. Fang, L. Ye, H. C. Po, J. Denlinger, C. Jozwiak, A. Bostwick, E. Rotenberg, E. Kaxiras, J. G. Checkelsky, and R. Comin, Topological flat bands in frustrated kagome lattice $CoSn$, Nat. Commun. **11**, 4004 (2020).

[93] M. Kang, L. Ye, S. Fang, J.-S. You, A. Levitan, M. Han, J. I. Facio, C. Jozwiak, A. Bostwick, E. Rotenberg, M. K. Chan, R. D. McDonald, D. Graf, K. Kaznatcheev, E. Vescovo, D. C. Bell, E. Kaxiras, J. van den Brink, M. Richter, M. Prasad Ghimire, J. G. Checkelsky, and R. Comin, Dirac fermions and flat bands in the ideal kagome metal $\mathrm{FeSn}$, Nat. Mater. **19**, 163 (2020).

[94] M. Li, Q. Wang, G. Wang, Z. Yuan, W. Song, R. Lou, Z. Liu, Y. Huang, Z. Liu, H. Lei, Z. Yin, and S. Wang, Dirac cone, flat band and saddle point in kagome magnet $\mathrm{YMn_6Sn_6}$, Nat. Commun. **12**, 3129 (2021).

[95] I. I. Mazin, H. O. Jeschke, F. Lechermann, H. Lee, M. Fink, R. Thomale, and R. Valentí, Theoretical prediction of a strongly correlated Dirac metal, Nat. Commun. **5**, 4261 (2014).

[96] L. Ye, M. Kang, J. Liu, F. von Cube, C. R. Wicker, T. Suzuki, C. Jozwiak, A. Bostwick, E. Rotenberg, D. C. Bell, L. Fu, R. Comin, and J. G. Checkelsky, Massive Dirac fermions in a ferromagnetic kagome metal, Nature **555**, 638 (2018).

[97] J.-X. Yin, W. Ma, T. A. Cochran, X. Xu, S. S. Zhang, H.-J. Tien, N. Shumiya, G. Cheng, K. Jiang, B. Lian, Z. Song, G. Chang, I. Belopolski, D. Multer, M. Litskevich, Z.-J. Cheng, X. P. Yang, B. Swidler, H. Zhou, H. Lin, T. Neupert, Z. Wang, N. Yao, T.-R. Chang, S. Jia, and M. Zahid Hasan, Quantum-limit Chern topological magnetism in $\mathrm{TbMn_6Sn_6}$, Nature **583,** 533 (2020).

[98] A. Bolens and N. Nagaosa, Topological states on the breathing kagome lattice, Phys. Rev. B **99**, 165141 (2019).

[99] Z. A. Kelly, T. T. Tran, and T. M. McQueen, Nonpolar-to-Polar Trimerization Transitions in the S = 1 Kagomé Magnet $\mathrm{Na_2Ti_3Cl_8}$, lnorg. Chem. **58**, 11941 (2019).

[100] M. Ezawa, Higher-Order Topological Insulators and Semimetals on the Breathing Kagome and Pyrochlore Lattices, Phys. Rev. Lett. **120**, 026801 (2018).

[101] A. Sil and A. K. Ghosh, First and second order topological phases on ferromagnetic breathing kagome lattice, J. Phys. Condens. Mater. **32**, 205601 (2020).

[102] G. Grüner, The dynamics of charge-density waves, Rev. Mod. Phys. **60**, 1129 (1988).

[103] G. Grüner, *Density waves in solids* (Perseus Publishing, Cambridge, MA, 1994).

[104] R. E. Thorne, Charge-Density-Wave Conductors, Phys. Today **49**, 42 (1996).

[105] R. C. Morris, Connection between Charge-Density Waves and Superconductivity in $NbSe_2$, Phys. Rev. Lett. **34**, 1164 (1975).

[106] A. M. Gabovich, A. I. Voitenko, J. F. Annett, and M. Ausloos, Charge- and spin-density-wave superconductors, Supercon. Sci. Technol. **14**, R1 (2001).

[107] M. H. Jung, A. Alsmadi, H. C. Kim, Y. Bang, K. H. Ahn, K. Umeo, A. H. Lacerda, H. Nakotte, H. C. Ri, and T. Takabatake, Superconductivity in magnetically ordered $CeTe_{1.82}$, Phys. Rev. B **67**, 212504 (2003).

[108] T. Valla, A. V. Fedorov, P. D. Johnson, P. A. Glans, C. McGuinness, K. E. Smith, E. Y. Andrei, and H. Berger, Quasiparticle Spectra, Charge-Density Waves, Superconductivity, and Electron-Phonon Coupling in $2H-NbSe_2$, Phys. Rev. Lett. **92**, 086401 (2004).

[109] Y. Singh, R. Nirmala, S. Ramakrishnan, and S. K. Malik, Competition between superconductivity and charge-density-wave ordering in the $Lu_5Ir_4(Si_{1-x}Ge_x)_{10}$ alloy system, Phys. Rev. B **72**, 045106 (2005).

[110] B. Sipos, A. F. Kusmartseva, A. Akrap, H. Berger, L. Forró, and E. Tutiš, From Mott state to superconductivity in $1T - TaS_2$, Nat. Mater. **7**, 960 (2008).

[111] N. Ru, J. H. Chu, and I. R. Fisher, Magnetic properties of the charge density wave compounds $R\mathrm{Te}_3$ ($R = \mathrm{Y}, \mathrm{La}, \mathrm{Ce}, \mathrm{Pr}, \mathrm{Nd}, \mathrm{Sm}, \mathrm{Gd}, \mathrm{Tb}, \mathrm{Dy}, \mathrm{Ho}, \mathrm{Er},$ and $\mathrm{Tm}$), Phys. Rev. B **78**, 012410 (2008).

[112] I. Naik and A. K. Rastogi, Charge density wave and superconductivity in $2\mathrm{H}-$ and $4\mathrm{H} - \mathrm{NbSe}_2$: A revisit, Pramana **76**, 957 (2011).

[113] C.-W. Chen, J. Choe, and E. Morosan, Charge density waves in strongly correlated electron systems, Rep. Prog. Phys. **79**, 084505 (2016).

[114] A. Kogar, G. A. de la Pena, S. Lee, Y. Fang, S. X. L. Sun, D. B. Lioi, G. Karapetrov, K. D. Finkelstein, J. P. C. Ruff, P. Abbamonte, and S. Rosenkranz, Observation of a Charge Density Wave Incommensuration Near the Superconducting Dome in $\mathrm{Cu}_x\mathrm{TiSe}_2$, Phys. Rev. Lett. **118**, 027002 (2017).

[115] D. Won, D. H. Kiem, H. Cho, D. Kim, Y. Kim, M. Y. Jeong, C. Seo, J. Kim, J.-G. Park, M. J. Han, H. Yang, and S. Cho, Polymorphic Spin, Charge, and Lattice Waves in Vanadium Ditelluride, Adv. Mater. **32**, 1906578 (2020).

[116] R. Peierls and R. E. Peierls, *Quantum theory of solids* (Oxford University Press, 1955).

[117] N. W. Ashcroft and N. D. Mermin, *Solid State Physics* (Holt, Rinehart and Winston, 1976).

[118] G. H. Gweon, J. D. Denlinger, J. A. Clack, J. W. Allen, C. G. Olson, E. DiMasi, M. C. Aronson, B. Foran, and S. Lee, Direct Observation of Complete Fermi Surface, Imperfect Nesting, and Gap Anisotropy in the High-Temperature Incommensurate Charge-Density-Wave Compound $\mathrm{SmTe}_3$, Phys. Rev. Lett. **81**, 886 (1998).

[119] D. R. Garcia, G. H. Gweon, S. Y. Zhou, J. Graf, C. M. Jozwiak, M. H. Jung, Y. S. Kwon, and A. Lanzara, Revealing Charge Density Wave Formation in the $\mathrm{LaTe}_2$ System by Angle Resolved Photoemission Spectroscopy, Phys. Rev. Lett. **98**, 166403 (2007).

[120] P. Aebi, T. Pillo, H. Berger, and F. Lévy, On the search for Fermi surface nesting in quasi-2D materials, J. Electron Spectros. Relat. Phenomena **117-118**, 433 (2001).

[121] Z. Xu, H. Yang, X. Song, Y. Chen, H. Yang, M. Liu, Z. Huang, Q. Zhang, J. Sun, L. Liu, and Y. Wang, Topical review: recent progress of charge density waves in 2D transition metal dichalcogenide-based heterojunctions and their applications, Nanotechnology **32**, 492001 (2021).

[122] F. J. Himpsel, Angle-resolved measurements of the photoemission of electrons in the study of solids, Adv. Phys. **32**, 1 (1983).

[123] S. D. Kevan, *Angle-resolved photoemission: theory and current applications* (Elsevier, 1992).

[124] S. Hüfner, *Potoelectron Spectroscopy: Principles and Applications* (Springer Berlin, 1995).

[125] A. Damascelli, Z. Hussain, and Z.-X. Shen, Angle-resolved photoemission studies of the cuprate superconductors, Rev. Mod. Phys. **75**, 473 (2003).

[126] A. Damascelli, Probing the Electronic Structure of Complex Systems by ARPES, Phys. Scr. **2004**, 61 (2004).

[127] D. Lu, I. M. Vishik, M. Yi, Y. Chen, R. G. Moore, and Z.-X. Shen, Angle-Resolved Photoemission Studies of Quantum Materials, Annu. Rev. Condens. Matter Phys. **3**, 129 (2012).

[128] H. Yang, A. Liang, C. Chen, C. Zhang, N. B. M. Schroeter, and Y. Chen, Visualizing electronic structures of quantum materials by angle-resolved photoemission spectroscopy, Nat. Rev. Mater.**3**, 341 (2018).

[129] B. Lv, T. Qian, and H. Ding, Angle-resolved photoemission spectroscopy and its application to topological materials, Nat. Rev. Phys. **1**, 609 (2019).

[130] J. A. Sobota, Y. He, and Z.-X. Shen, Angle-resolved photoemission studies of quantum materials, Rev. Mod. Phys. **93**, 025006 (2021).

[131] S. Suga, A. Sekiyama, and C. Tusche, *Photoelectrom Spectroscopy*, (Springer, 2021).

[132] H. Hertz, Ueber sehr schnelle electrische Schwingungen, Ann. Phys. **267**, 421 (1887).

[133] W. Hallwachs, Ueber den Einfluss des Lichtes auf electrostatisch geladene Körper, Ann. Phys. **269**, 301 (1888).

[134] P. Lenard, Erzeugung von Kathodenstrahlen durch ultraviolettes Licht, Ann. Phys. **307**, 359 (1900).

[135] A. Einstein, Zur Theorie der Lichterzeugung und Lichtabsorption, Ann. Phys. **325**, 199 (1906).

[136] Y. Liu, J. E. Beetar, M. M. Hosen, G. Dhakal, C. Sims, F. Kabir, M. B. Etienne, K. Dimitri, S. Regmi, Y. Liu, A. K. Pathak, D. Kaczorowski, M. Neupane, and M. Chini, Extreme ultraviolet time- and angle-resolved photoemission setup with 21.5 meV resolution using high-order harmonic generation from a turn-key Yb:KGW amplifier, Rev. Sci. Instrum. **91**, 013102 (2020).

[137] N. Mårtensson, P. Baltzer, P. A. Brühwiler, J. O. Forsell, A. Nilsson, A. Stenborg, and B. Wannberg, A very high resolution electron spectrometer, J. Electron Spectrosc. Relat. Phenom. **70**, 117 (1994).

[138] J. Castle, *Practical surface analysis by Auger and X-ray photoelectron spectroscopy* (Wiley Online Library, 1984).

[139] F. Schmitt, P. S. Kirchmann, U. Bovensiepen, R. G. Moore, L. Rettig, M. Krenz, J.-H. Chu, N. Ru, L. Perfetti, D. H. Lu, M. Wolf, I. R. Fisher, and Z.-X. Shen, Transient Electronic Structure and Melting of a Charge Density Wave in $\mathrm{TbTe_3}$, Science **321**, 1649 (2008).

[140] C. L. Smallwood, J. P. Hinton, C. Jozwiak, W. Zhang, J. D. Koralek, H. Eisaki, D.-H. Lee, J. Orenstein, and A. Lanzara, Tracking Cooper Pairs in a Cuprate Superconductor by Ultrafast Angle-Resolved Photoemission, Science **336**, 1137 (2012).

[141] F. Liu, M. E. Ziffer, K. R. Hansen, J. Wang, and X. Zhu, Direct Determination of Band-Gap Renormalization in the Photoexcited Monolayer $\mathrm{MoS_2}$, Phys. Rev. Lett. **122**, 246803 (2019).

[142] G. Gatti, A. Crepaldi, M. Puppin, N. Tancogne-Dejean, L. Xian, U. De Giovannini, S. Roth, S. Polishchuk, P. Bugnon, A. Magrez, H. Berger, F. Frassetto, L. Poletto, L. Moreschini, S. Moser, A. Bostwick, E. Rotenberg, A. Rubio, M. Chergui, and M. Grioni, Light-Induced Renormalization of the Dirac Quasiparticles in the Nodal-Line Semimetal $\mathrm{ZrSiSe}$, Phys. Rev. Lett. **125**, 076401 (2020).

[143] J. Madéo, M. K. L. Man, C. Sahoo, M. Campbell, V. Pareek, E. L. Wong, A. Al-Mahboob, N. S. Chan, A. Karmakar, B. M. K. Mariserla, X. Li, T. F. Heinz, T. Cao, and K. M. Dani, Directly visualizing the momentum-forbidden dark excitons and their dynamics in atomically thin semiconductors, Science **370**, 1199 (2020).

[144] P. Hein, S. Jauernik, H. Erk, L. Yang, Y. Qi, Y. Sun, C. Felser, and M. Bauer, Mode-resolved reciprocal space mapping of electron-phonon interaction in the Weyl semimetal candidate $\mathrm{T_d - WTe_2}$, Nat. Commun. **11**, 2613 (2020).

[145] T. Suzuki, Y. Shinohara, Y. Lu, M. Watanabe, J. Xu, K. L. Ishikawa, H. Takagi, M. Nohara, N. Katayama, H. Sawa, M. Fujisawa, T. Kanai, J. Itatani, T. Mizokawa, S. Shin, and K. Okazaki, Detecting electron-phonon coupling during photoinduced phase transition, Phys. Rev. B **103**, L121105 (2021).

[146] Y. Liu, G. Dhakal, A. P. Sakhya, J. E. Beetar, F. Kabir, S. Regmi, D. Kaczorowski, M. Chini, B. M. Fregoso, and M. Neupane, Ultrafast relaxation of acoustic and optical phonons in a topological nodal-line semimetal $ZrSiS$, Commun. Phys. **5**, 203 (2022).

[147] G. Dhanaraj, K. Byrappa, V. Prasad, and M. Dudley, *Springer handbook of crystal growth* (Springer Berlin, 2010).

[148] W. H. Bragg and W. L. Bragg, The reflection of X-rays by crystals, Proceedings of the Royal Society of London. Series A, Containing Papers of a Mathematical and Physical Character **88**, 428 (1913).

[149] S. Roy, H. L. Meyerheim, K. Mohseni, A. Ernst, M. M. Otrokov, M. G. Vergniory, G. Mussler, J. Kampmeier, D. Grützmacher, C. Tusche, J. Schneider, E. V. Chulkov, and J. Kirschner, Atomic relaxations at the (0001) surface of $Bi_2Se_3$ single crystals and ultrathin films, Phys. Rev. B **90**, 155456 (2014).

[150] T. P. Ginley, Y. Wang, and S. Law, Topological Insulator Film Growth by Molecular Beam Epitaxy: A Review, Crystals **6**, 154 (2016).

[151] A. Y. Cho, Film Deposition by Molecular-Beam Techniques, Journal of Vacuum Science and Technology **8**, S31 (1971).

[152] A. Y. Cho, Advances in molecular beam epitaxy (MBE), J. Cryst. Growth **111**, 1 (1991).

[153] B. A. Joyce, Molecular beam epitaxy, Rep. Prog. Phys. **48**, 1637 (1985).

[154] L. He, X. Kou, and K. L. Wang, Review of 3D topological insulator thin-film growth by molecular beam epitaxy and potential applications, Phys. Status Solidi RRL **7**, 50 (2013).

[155] W. Nunn, T. K. Truttmann, and B. Jalan, A review of molecular-beam epitaxy of wide bandgap complex oxide semiconductors, J. Mater. Res. **36**, 4846 (2021).

[156] M. Z. Hasan, S.-Y. Xu, and M. Neupane, Topological Insulators, Topological Dirac semimetals, Topological Crystalline Insulators, and Topological Kondo Insulators in *Topological insulators: Fundamentals and perspectives*, edited by S. R. Frank Ortmann, Sergio O. Valenzuela (John Wiley & Sons, 2015), pp. 55.

[157] Y. Xu, Z. Song, Z. Wang, H. Weng, and X. Dai, Higher-Order Topology of the Axion Insulator $\mathrm{EuIn_2As_2}$, Phys. Rev. Lett. **122**, 256402 (2019).

[158] C. Yue, Y. Xu, Z. Song, H. Weng, Y.-M. Lu, C. Fang, and X. Dai, Symmetry-enforced chiral hinge states and surface quantum anomalous Hall effect in the magnetic axion insulator $\mathrm{Bi_{2-x}Sm_xSe_3}$, Nat. Phys. **15**, 577 (2019).

[159] M. Ezawa, Minimal models for Wannier-type higher-order topological insulators and phosphorene, Phys. Rev. B **98**, 045125 (2018).

[160] R.-X. Zhang, F. Wu, and S. Das Sarma, Möbius Insulator and Higher-Order Topology in $\mathrm{MnBi_{2n}Te_{3n+1}}$, Phys. Rev. Lett. **124**, 136407 (2020).

[161] M. M. Otrokov, I. I. Klimovskikh, H. Bentmann, D. Estyunin, A. Zeugner, Z. S. Aliev, S. Gaß, A. U. B. Wolter, A. V. Koroleva, A. M. Shikin, M. Blanco-Rey, M. Hoffmann, I. P. Rusinov, A. Y. Vyazovskaya, S. V. Eremeev, Y. M. Koroteev, V. M. Kuznetsov, F. Freyse, J. Sánchez-Barriga, I. R. Amiraslanov, M. B. Babanly, N. T. Mamedov, N. A. Abdullayev, V. N. Zverev, A. Alfonsov, V. Kataev, B. Büchner, E. F. Schwier, S. Kumar, A. Kimura, L. Petaccia, G. Di Santo, R. C. Vidal, S. Schatz, K. Kißner, M. Ünzelmann, C. H. Min, S. Moser, T. R. F. Peixoto, F. Reinert, A. Ernst, P. M. Echenique, A. Isaeva, and E. V. Chulkov, Prediction and observation of an antiferromagnetic topological insulator, Nature **576**, 416 (2019).

[162] Y.-J. Hao, P. Liu, Y. Feng, X.-M. Ma, E. F. Schwier, M. Arita, S. Kumar, C. Hu, R. e. Lu, M. Zeng, Y. Wang, Z. Hao, H.-Y. Sun, K. Zhang, J. Mei, N. Ni, L. Wu, K. Shimada, C. Chen,

Q. Liu, and C. Liu, Gapless Surface Dirac Cone in Antiferromagnetic Topological Insulator $MnBi_2Te_4$, Phys. Rev. X **9**, 041038 (2019).

[163] H. Li, S.-Y. Gao, S.-F. Duan, Y.-F. Xu, K.-J. Zhu, S.-J. Tian, J.-C. Gao, W.-H. Fan, Z.-C. Rao, J.-R. Huang, J.-J. Li, D.-Y. Yan, Z.-T. Liu, W.-L. Liu, Y.-B. Huang, Y.-L. Li, Y. Liu, G.-B. Zhang, P. Zhang, T. Kondo, S. Shin, H.-C. Lei, Y.-G. Shi, W.-T. Zhang, H.-M. Weng, T. Qian, and H. Ding, Dirac Surface States in Intrinsic Magnetic Topological Insulators $EuSn_2As_2$ and $MnBi_{2n}Te_{3n+1}$, Phys. Rev. X **9**, 041039 (2019).

[164] Y. J. Chen, L. X. Xu, J. H. Li, Y. W. Li, H. Y. Wang, C. F. Zhang, H. Li, Y. Wu, A. J. Liang, C. Chen, S. W. Jung, C. Cacho, Y. H. Mao, S. Liu, M. X. Wang, Y. F. Guo, Y. Xu, Z. K. Liu, L. X. Yang, and Y. L. Chen, Topological Electronic Structure and Its Temperature Evolution in Antiferromagnetic Topological Insulator $MnBi_2Te_4$, Phys. Rev. X **9**, 041040 (2019).

[165] C. Hu, K. N. Gordon, P. Liu, J. Liu, X. Zhou, P. Hao, D. Narayan, E. Emmanouilidou, H. Sun, Y. Liu, H. Brawer, A. P. Ramirez, L. Ding, H. Cao, Q. Liu, D. Dessau, and N. Ni, A van der Waals antiferromagnetic topological insulator with weak interlayer magnetic coupling, Nat. Commun. **11**, 97 (2020).

[166] X. Gui, I. Pletikosic, H. Cao, H.-J. Tien, X. Xu, R. Zhong, G. Wang, T.-R. Chang, S. Jia, T. Valla, W. Xie, and R. J. Cava, A New Magnetic Topological Quantum Material Candidate by Design, ACS Cent. Sci. **5**, 900 (2019).

[167] A. M. Goforth, P. Klavins, J. C. Fettinger, and S. M. Kauzlarich, Magnetic Properties and Negative Colossal Magnetoresistance of the Rare Earth Zintl phase $EuIn_2As_2$, lnorg. Chem. 47, 11048 (2008).

[168] P. C. Canfield and Z. Fisk, Growth of single crystals from metallic fluxes, Philos. Mag. B **65**, 1117 (1992).

[169] P. Hohenberg and W. Kohn, Inhomogeneous Electron Gas, Phys. Rev. **136**, B864 (1964).

[170] W. Kohn and L. J. Sham, Self-Consistent Equations Including Exchange and Correlation Effects, Phys. Rev. **140**, A1133 (1965).

[171] P. E. Blöchl, Projector augmented-wave method, Phys. Rev. B **50**, 17953 (1994).

[172] G. Kresse and D. Joubert, From ultrasoft pseudopotentials to the projector augmented-wave method, Phys. Rev. B **59**, 1758 (1999).

[173] G. Kresse and J. Furthmüller, Efficient iterative schemes for ab initio total-energy calculations using a plane-wave basis set, Phys. Rev. B **54**, 11169 (1996).

[174] G. Kresse and J. Furthmüller, Efficiency of ab-initio total energy calculations for metals and semiconductors using a plane-wave basis set, Comput. Mater. Sci. **6**, 15 (1996).

[175] J. P. Perdew, K. Burke, and M. Ernzerhof, Generalized Gradient Approximation Made Simple, Phys. Rev. Lett. **77**, 3865 (1996).

[176] S. L. Dudarev, G. A. Botton, S. Y. Savrasov, C. J. Humphreys, and A. P. Sutton, Electron-energy-loss spectra and the structural stability of nickel oxide: An LSDA+U study, Phys. Rev. B **57**, 1505 (1998).

[177] N. Marzari and D. Vanderbilt, Maximally localized generalized Wannier functions for composite energy bands, Phys. Rev. B **56**, 12847 (1997).

[178] Q. Wu, S. Zhang, H.-F. Song, M. Troyer, and A. A. Soluyanov, WannierTools: An open-source software package for novel topological materials, Comput. Phys. Commun. **224**, 405 (2018).

[179] A. Topp, J. M. Lippmann, A. Varykhalov, V. Duppel, B. V. Lotsch, C. R. Ast, and L. M. Schoop, Non-symmorphic band degeneracy at the Fermi level in $\mathrm{ZrSiTe}$, New J. Phys. **18,** 125014 (2016).

[180] J. Hu, Z. Tang, J. Liu, X. Liu, Y. Zhu, D. Graf, K. Myhro, S. Tran, C. N. Lau, J. Wei, and Z. Mao, Evidence of Topological Nodal-Line Fermions in $\mathrm{ZrSiSe}$ and $\mathrm{ZrSiTe}$, Phys. Rev. Lett. **117,** 016602 (2016).

[181] D. Takane, Z. Wang, S. Souma, K. Nakayama, C. X. Trang, T. Sato, T. Takahashi, and Y. Ando, Dirac-node arc in the topological line-node semimetal $\mathrm{HfSiS}$, Phys. Rev. B **94,** 121108 (2016).

[182] R. Lou, J. Z. Ma, Q. N. Xu, B. B. Fu, L. Y. Kong, Y. G. Shi, P. Richard, H. M. Weng, Z. Fang, S. S. Sun, Q. Wang, H. C. Lei, T. Qian, H. Ding, and S. C. Wang, Emergence of topological bands on the surface of $\mathrm{ZrSnTe}$ crystal, Phys. Rev. B **93,** 241104 (2016).

[183] M. M. Hosen, K. Dimitri, I. Belopolski, P. Maldonado, R. Sankar, N. Dhakal, G. Dhakal, T. Cole, P. M. Oppeneer, D. Kaczorowski, F. Chou, M. Z. Hasan, T. Durakiewicz, and M. Neupane, Tunability of the topological nodal-line semimetal phase in $\mathrm{ZrSi}X$-type materials ($X = \mathrm{S}, \mathrm{Se}, \mathrm{Te}$), Phys. Rev. B **95,** 161101 (2017).

[184] C. Chen, X. Xu, J. Jiang, S. C. Wu, Y. P. Qi, L. X. Yang, M. X. Wang, Y. Sun, N. B. M. Schröter, H. F. Yang, L. M. Schoop, Y. Y. Lv, J. Zhou, Y. B. Chen, S. H. Yao, M. H. Lu, Y. F. Chen, C. Felser, B. H. Yan, Z. K. Liu, and Y. L. Chen, Dirac line nodes and effect of spin-orbit coupling in the nonsymmorphic critical semimetals $M\mathrm{SiS}$ ($M = \mathrm{Hf}, \mathrm{Zr}$), Phys. Rev. B 95, 125126 (2017).

[185] J. Hu, Y. Zhu, X. Gui, D. Graf, Z. Tang, W. Xie, and Z. Mao, Quantum oscillation evidence for a topological semimetal phase in $\mathrm{ZrSnTe}$, Phys. Rev. B **97,** 155101 (2018).

[186] J. Zhang, M. Gao, J. Zhang, X. Wang, X. Zhang, M. Zhang, W. Niu, R. Zhang, and Y. Xu, Transport evidence of 3D topological nodal-line semimetal phase in $\mathrm{ZrSiS}$, Front. Phys. **13,** 137201 (2018).

[187] M. M. Hosen, K. Dimitri, A. Aperis, P. Maldonado, I. Belopolski, G. Dhakal, F. Kabir, C. Sims, M. Z. Hasan, D. Kaczorowski, T. Durakiewicz, P. M. Oppeneer, and M. Neupane, Observation of gapless Dirac surface states in $\mathrm{ZrGeTe}$, Phys. Rev. B **97,** 121103 (2018).

[188] Y. Yen, C.-L. Chiu, P.-H. Lin, R. Sankar, F. Chou, T.-M. Chuang, and G.-Y. Guo, Dirac Nodal Line and Rashba Splitting Surface States in Nonsymmorphic $\mathrm{ZrGeTe}$, arXiv:1912.07002 (2019).

[189] Z. Cheng, Z. Zhang, H. Sun, S. Li, H. Yuan, Z. Wang, Y. Cao, Z. Shao, Q. Bian, X. Zhang, F. Li, J. Feng, S. Ding, Z. Mao, and M. Pan, Visualizing Dirac nodal-line band structure of topological semimetal $\mathrm{ZrGeSe}$ by ARPES, APL Mater. **7,** 051105 (2019).

[190] B. B. Fu, C. J. Yi, T. T. Zhang, M. Caputo, J. Z. Ma, X. Gao, B. Q. Lv, L. Y. Kong, Y. B. Huang, P. Richard, M. Shi, V. N. Strocov, C. Fang, H. M. Weng, Y. G. Shi, T. Qian, and H. Ding, Dirac nodal surfaces and nodal lines in $\mathrm{ZrSiS}$, Sci. Adv. **5,** eaau6459 (2019).

[191] M. N. Ali, L. M. Schoop, C. Garg, J. M. Lippmann, E. Lara, B. Lotsch, and S. S. P. Parkin, Butterfly magnetoresistance, quasi-2D Dirac Fermi surface and topological phase transition in $\mathrm{ZrSiS}$, Sci. Adv. **2,** e1601742 (2016).

[192] Y.-Y. Lv, B.-B. Zhang, X. Li, S.-H. Yao, Y. B. Chen, J. Zhou, S.-T. Zhang, M.-H. Lu, and Y.-F. Chen, Extremely large and significantly anisotropic magnetoresistance in $\mathrm{ZrSiS}$ single crystals, Appl. Phys. Lett. **108,** 244101 (2016).

[193] R. Singha, A. K. Pariari, B. Satpati, and P. Mandal, Large nonsaturating magnetoresistance and signature of nondegenerate Dirac nodes in $ZrSiS$, Proc. Natl. Acad. Sci. **114,** 2468 (2017).

[194] N. Kumar, K. Manna, Y. Qi, S.-C. Wu, L. Wang, B. Yan, C. Felser, and C. Shekhar, Unusual magnetotransport from Si-square nets in topological semimetal $HfSiS$, Phys. Rev. B **95,** 121109 (2017).

[195] S. Pezzini, M. R. van Delft, L. M. Schoop, B. V. Lotsch, A. Carrington, M. I. Katsnelson, N. E. Hussey, and S. Wiedmann, Unconventional mass enhancement around the Dirac nodal loop in $ZrSiS$, Nat. Phys. **14,** 178 (2018).

[196] M. B. Schilling, L. M. Schoop, B. V. Lotsch, M. Dressel, and A. V. Pronin, Flat Optical Conductivity in $ZrSiS$ due to Two-Dimensional Dirac Bands, Phys. Rev. Lett. **119,** 187401 (2017).

[197] M. M. Hosen, G. Dhakal, K. Dimitri, P. Maldonado, A. Aperis, F. Kabir, C. Sims, P. Riseborough, P. M. Oppeneer, D. Kaczorowski, T. Durakiewicz, and M. Neupane, Discovery of topological nodal-line fermionic phase in a magnetic material $GdSbTe$, Sci. Rep. **8**, 13283 (2018).

[198] L. M. Schoop, A. Topp, J. Lippmann, F. Orlandi, L. Müchler, M. G. Vergniory, Y. Sun, A. W. Rost, V. Duppel, M. Krivenkov, S. Sheoran, P. Manuel, A. Varykhalov, B. Yan, R. K. Kremer, C. R. Ast, and B. V. Lotsch, Tunable Weyl and Dirac states in the nonsymmorphic compound $CeSbTe$, Sci. Adv. **4**, eaar2317 (2018).

[199] A. Topp, M. G. Vergniory, M. Krivenkov, A. Varykhalov, F. Rodolakis, J. L. McChesney, B. V. Lotsch, C. R. Ast, and L. M. Schoop, The effect of spin-orbit coupling on nonsymmorphic square-net compounds, J. Phys. Chem. Solids **128**, 296 (2019).

[200] Y. Wang, Y. Qian, M. Yang, H. Chen, C. Li, Z. Tan, Y. Cai, W. Zhao, S. Gao, Y. Feng, S. Kumar, E. F. Schwier, L. Zhao, H. Weng, Y. Shi, G. Wang, Y. Song, Y. Huang, K. Shimada, Z. Xu, X. J. Zhou, and G. Liu, Spectroscopic evidence for the realization of a genuine topological nodal-line semimetal in $\mathrm{LaSbTe}$, Phys. Rev. B **103**, 125131 (2021).

[201] S. Yue, Y. Qian, M. Yang, D. Geng, C. Yi, S. Kumar, K. Shimada, P. Cheng, L. Chen, Z. Wang, H. Weng, Y. Shi, K. Wu, and B. Feng, Topological electronic structure in the antiferromagnet $\mathrm{HoSbTe}$, Phys. Rev. B **102**, 155109 (2020).

[202] K. Pandey, D. Mondal, J. W. Villanova, J. Roll, R. Basnet, A. Wegner, G. Acharya, M. R. U. Nabi, B. Ghosh, J. Fujii, J. Wang, B. Da, A. Agarwal, I. Vobornik, A. Politano, S. Barraza-Lopez, and J. Hu, Magnetic Topological Semimetal Phase with Electronic Correlation Enhancement in $\mathrm{SmSbTe}$, Adv. Quantum Technol. **4**, 2100063 (2021).

[203] Z. Ren, A. A. Taskin, S. Sasaki, K. Segawa, and Y. Ando, Large bulk resistivity and surface quantum oscillations in the topological insulator $\mathrm{Bi_2Te_2Se}$, Phys. Rev. B **82**, 241306 (2010).

[204] A. A. Taskin, Z. Ren, S. Sasaki, K. Segawa, and Y. Ando, Observation of Dirac Holes and Electrons in a Topological Insulator, Phys. Rev. Lett. **107**, 016801 (2011).

[205] K. Pandey, R. Basnet, A. Wegner, G. Acharya, M. R. U. Nabi, J. Liu, J. Wang, Y. K. Takahashi, B. Da, and J. Hu, Electronic and magnetic properties of the topological semimetal candidate $\mathrm{NdSbTe}$, Phys. Rev. B 101, 235161 (2020).

[206] R. Sankar, I. P. Muthuselvam, K. Rajagopal, K. Ramesh Babu, G. S. Murugan, K. S. Bayikadi, K. Moovendaran, C. Ting Wu, and G.-Y. Guo, Anisotropic Magnetic Properties of Nonsymmorphic Semimetallic Single Crystal $\mathrm{NdSbTe}$, Crys. Growth Des. **20**, 6585 (2020).

[207] J. P. Charvillat, D. Damien, and A. Wojakowski, Crystal chemistry of binary $\mathrm{MSb_2}$ and ternary $\mathrm{MSbTe}$ compounds of transuranium elements, Revue de Chimie Minerale **14**, 178 (1977).

[208] M. S. Lodge, G. Chang, C.-Y. Huang, B. Singh, J. Hellerstedt, M. T. Edmonds, D. Kaczorowski, M. M. Hosen, M. Neupane, H. Lin, M. S. Fuhrer, B. Weber, and M. Ishigami, Observation of Effective Pseudospin Scattering in $\mathrm{ZrSiS}$, Nano Lett. **17**, 7213 (2017).

[209] M. P. L. Sancho, J. M. L. Sancho, J. M. L. Sancho, and J. Rubio, Highly convergent schemes for the calculation of bulk and surface Green functions, J. Phys. F: Metal Physics **15**, 851 (1985).

[210] A. A. Mostofi, J. R. Yates, G. Pizzi, Y.-S. Lee, I. Souza, D. Vanderbilt, and N. Marzari, An updated version of wannier90: A tool for obtaining maximally-localised Wannier functions, Comput. Phys. Commun. **185**, 2309 (2014).

[211] H. J. Monkhorst and J. D. Pack, Special points for Brillouin-zone integrations, Phys. Rev. B **13**, 5188 (1976).

[212] A. I. Liechtenstein, V. I. Anisimov, and J. Zaanen, Density-functional theory and strong interactions: Orbital ordering in Mott-Hubbard insulators, Phys. Rev. B **52**, R5467 (1995).

[213] P. Giannozzi, S. Baroni, N. Bonini, M. Calandra, R. Car, C. Cavazzoni, D. Ceresoli, G. L. Chiarotti, M. Cococcioni, I. Dabo, A. Dal Corso, S. de Gironcoli, S. Fabris, G. Fratesi, R. Gebauer, U. Gerstmann, C. Gougoussis, A. Kokalj, M. Lazzeri, L. Martin-Samos, N. Marzari, F. Mauri, R. Mazzarello, S. Paolini, A. Pasquarello, L. Paulatto, C. Sbraccia, S. Scandolo, G. Sclauzero, A. P. Seitsonen, A. Smogunov, P. Umari, and R. M. Wentzcovitch, QUANTUM ESPRESSO: a modular and open-source software project for quantum simulations of materials, J. Phys. Condens. Mater. **21**, 395502 (2009).

[214] P. Giannozzi, O. Andreussi, T. Brumme, O. Bunau, M. Buongiorno Nardelli, M. Calandra, R. Car, C. Cavazzoni, D. Ceresoli, M. Cococcioni, N. Colonna, I. Carnimeo, A. Dal Corso, S. de Gironcoli, P. Delugas, R. A. DiStasio, A. Ferretti, A. Floris, G. Fratesi, G. Fugallo, R. Gebauer, U. Gerstmann, F. Giustino, T. Gorni, J. Jia, M. Kawamura, H. Y. Ko, A. Kokalj, E. Küçükbenli, M. Lazzeri, M. Marsili, N. Marzari, F. Mauri, N. L. Nguyen, H. V. Nguyen, A. Otero-de-la-Roza, L. Paulatto, S. Poncé, D. Rocca, R. Sabatini, B. Santra, M. Schlipf, A. P. Seitsonen, A. Smogunov, I. Timrov, T. Thonhauser, P. Umari, N. Vast, X. Wu, and S. Baroni, Advanced capabilities for materials modelling with Quantum ESPRESSO, J. Phys. Condens. Mater. **29**, 465901 (2017).

[215] P. Giannozzi, O. Baseggio, P. Bonfà, D. Brunato, R. Car, I. Carnimeo, C. Cavazzoni, S. de Gironcoli, P. Delugas, F. Ferrari Ruffino, A. Ferretti, N. Marzari, I. Timrov, A. Urru, and S. Baroni, Quantum ESPRESSO toward the exascale, J. Chem. Phys. **152**, 154105 (2020).

[216] A. Dal Corso, Pseudopotentials periodic table: From H to Pu, Comput. Mater. Sci. **95**, 337 (2014).

[217] I. Souza, N. Marzari, and D. Vanderbilt, Maximally localized Wannier functions for entangled energy bands, Phys. Rev. B **65**, 035109 (2001).

[218] N. Marzari, A. A. Mostofi, J. R. Yates, I. Souza, and D. Vanderbilt, Maximally localized Wannier functions: Theory and applications, Rev. Mod. Phys. **84**, 1419 (2012).

[219] H. M. Guo and M. Franz, Topological insulator on the kagome lattice, Phys. Rev. B **80,** 113102 (2009).

[220] J. Wen, A. Rüegg, C. C. J. Wang, and G. A. Fiete, Interaction-driven topological insulators on the kagome and the decorated honeycomb lattices, Phys. Rev. B **82,** 075125 (2010).

[221] T. Kida, L. A. Fenner, A. A. Dee, I. Terasaki, M. Hagiwara, and A. S. Wills, The giant anomalous Hall effect in the ferromagnet $Fe_3Sn_2$ — a frustrated kagome metal, J. Phys. Condens. Mater. **23,** 112205 (2011).

[222] T.-H. Han, J. S. Helton, S. Chu, D. G. Nocera, J. A. Rodriguez-Rivera, C. Broholm, and Y. S. Lee, Fractionalized excitations in the spin-liquid state of a kagome-lattice antiferromagnet, Nature **492,** 406 (2012).

[223] S. Nakatsuji, N. Kiyohara, and T. Higo, Large anomalous Hall effect in a non-collinear antiferromagnet at room temperature, Nature **527,** 212 (2015).

[224] K. Kuroda, T. Tomita, M. T. Suzuki, C. Bareille, A. A. Nugroho, P. Goswami, M. Ochi, M. Ikhlas, M. Nakayama, S. Akebi, R. Noguchi, R. Ishii, N. Inami, K. Ono, H. Kumigashira, A. Varykhalov, T. Muro, T. Koretsune, R. Arita, S. Shin, T. Kondo, and S. Nakatsuji, Evidence for magnetic Weyl fermions in a correlated metal, Nat. Mater. **16,** 1090 (2017).

[225] J.-X. Yin, S. S. Zhang, H. Li, K. Jiang, G. Chang, B. Zhang, B. Lian, C. Xiang, I. Belopolski, H. Zheng, T. A. Cochran, S.-Y. Xu, G. Bian, K. Liu, T.-R. Chang, H. Lin, Z.-Y. Lu, Z. Wang, S. Jia, W. Wang, and M. Z. Hasan, Giant and anisotropic many-body spin–orbit tunability in a strongly correlated kagome magnet, Nature **562,** 91 (2018).

[226] J.-X. Yin, S. S. Zhang, G. Chang, Q. Wang, S. S. Tsirkin, Z. Guguchia, B. Lian, H. Zhou, K. Jiang, I. Belopolski, N. Shumiya, D. Multer, M. Litskevich, T. A. Cochran, H. Lin, Z. Wang, T. Neupert, S. Jia, H. Lei, and M. Z. Hasan, Negative flat band magnetism in a spin–orbit-coupled correlated kagome magnet, Nat. Phys. **15,** 443 (2019).

[227] L. Jiao, Q. Xu, Y. Cheon, Y. Sun, C. Felser, E. Liu, and S. Wirth, Signatures for half-metallicity and nontrivial surface states in the kagome lattice Weyl semimetal $Co_3Sn_2S_2$, Phys. Rev. B **99,** 245158 (2019).

[228] Z. Lin, C. Wang, P. Wang, S. Yi, L. Li, Q. Zhang, Y. Wang, Z. Wang, H. Huang, Y. Sun, Y. Huang, D. Shen, D. Feng, Z. Sun, J.-H. Cho, C. Zeng, and Z. Zhang, Dirac fermions in antiferromagnetic $\mathrm{FeSn}$ kagome lattices with combined space inversion and time-reversal symmetry, Phys. Rev. B **102,** 155103 (2020).

[229] J. Ghimire Nirmal, L. Dally Rebecca, L. Poudel, D. C. Jones, D. Michel, N. T. Magar, M. Bleuel, A. McGuire Michael, J. S. Jiang, J. F. Mitchell, W. Lynn Jeffrey, and I. I. Mazin, Competing magnetic phases and fluctuation-driven scalar spin chirality in the kagome metal $\mathrm{YMn_6Sn_6}$, Sci. Adv. **6,** eabe2680 (2020).

[230] T. Asaba, S. M. Thomas, M. Curtis, J. D. Thompson, E. D. Bauer, and F. Ronning, Anomalous Hall effect in the kagome ferrimagnet $\mathrm{GdMn_6Sn_6}$, Phys. Rev. B **101,** 174415 (2020).

[231] Y.-X. Jiang, J.-X. Yin, M. M. Denner, N. Shumiya, B. R. Ortiz, G. Xu, Z. Guguchia, J. He, M. S. Hossain, X. Liu, J. Ruff, L. Kautzsch, S. S. Zhang, G. Chang, I. Belopolski, Q. Zhang, T. A. Cochran, D. Multer, M. Litskevich, Z.-J. Cheng, X. P. Yang, Z. Wang, R. Thomale, T. Neupert, S. D. Wilson, and M. Z. Hasan, Unconventional chiral charge order in kagome superconductor $\mathrm{KV_3Sb_5}$, Nat. Mater. **20,** 1353 (2021).

[232] W. Ma, X. Xu, J.-X. Yin, H. Yang, H. Zhou, Z.-J. Cheng, Y. Huang, Z. Qu, F. Wang, M. Z. Hasan, and S. Jia, Rare Earth Engineering in $R\mathrm{Mn_6Sn_6}$ ($R = \mathrm{Gd}-\mathrm{Tm}$, Lu) Topological Kagome Magnets, Phys. Rev. Lett. **126,** 246602 (2021).

[233] Q. Wang, K. J. Neubauer, C. Duan, Q. Yin, S. Fujitsu, H. Hosono, F. Ye, R. Zhang, S. Chi, K. Krycka, H. Lei, and P. Dai, Field-induced topological Hall effect and double-fan spin structure with a $c$-axis component in the metallic kagome antiferromagnetic compound $\mathrm{YMn_6Sn_6}$, Phys. Rev. B **103,** 014416 (2021).

[234] E. Tang, J.-W. Mei, and X.-G. Wen, High-Temperature Fractional Quantum Hall States, Phys. Rev. Lett. **106,** 236802 (2011).

[235] G. Xu, B. Lian, and S.-C. Zhang, Intrinsic Quantum Anomalous Hall Effect in the Kagome Lattice $\mathrm{Cs_2LiMn_3F_{12}}$, Phys. Rev. Lett. **115,** 186802 (2015).

[236] Y. Li, C. Liu, G.-D. Zhao, T. Hu, and W. Ren, Two-dimensional multiferroics in a breathing kagome lattice, Phys. Rev. B **104**, L060405 (2021).

[237] H. Tanaka, Y. Fujisawa, K. Kuroda, R. Noguchi, S. Sakuragi, C. Bareille, B. Smith, C. Cacho, S. W. Jung, T. Muro, Y. Okada, and T. Kondo, Three-dimensional electronic structure in ferromagnetic $\mathrm{Fe_3Sn_2}$ with breathing kagome bilayers, Phys. Rev. B **101**, 161114 (2020).

[238] G. Dhakal, F. Cheenicode Kabeer, A. K. Pathak, F. Kabir, N. Poudel, R. Filippone, J. Casey, A. Pradhan Sakhya, S. Regmi, C. Sims, K. Dimitri, P. Manfrinetti, K. Gofryk, P. M. Oppeneer, and M. Neupane, Anisotropically large anomalous and topological Hall effect in a kagome magnet, Phys. Rev. B **104,** L161115 (2021).

[239] S. Peng, Y. Han, G. Pokharel, J. Shen, Z. Li, M. Hashimoto, D. Lu, B. R. Ortiz, Y. Luo, H. Li, M. Guo, B. Wang, S. Cui, Z. Sun, Z. Qiao, S. D. Wilson, and J. He, Realizing Kagome Band Structure in Two-Dimensional Kagome Surface States of $R\mathrm{V_6Sn_6}$ ($R = \mathrm{Gd, Ho}$), Phys. Rev. Lett. **127,** 266401 (2021).

[240] F. Kabir, R. Filippone, G. Dhakal, Y. Lee, N. Poudel, J. Casey, A. P. Sakhya, S. Regmi, R. Smith, P. Manfrinetti, L. Ke, K. Gofryk, M. Neupane, and A. K. Pathak, Unusual magnetic and transport properties in $\mathrm{HoMn_6Sn_6}$ kagome magnet, Phys. Rev. Materials **6**, 064404 (2022).

[241] S. N. Magonov, P. Zoennchen, H. Rotter, H. J. Cantow, G. Thiele, J. Ren, and M. H. Whangbo, Scanning tunneling and atomic force microscopy study of layered transition metal halides $\mathrm{Nb_3X_8}$ (X = Cl, Br, I), J. Am. Chem. Soc. **115,** 2495 (1993).

[242] J. Jiang, Q. Liang, R. Meng, Q. Yang, C. Tan, X. Sun, and X. Chen, Exploration of new ferromagnetic, semiconducting and biocompatible $Nb_3X_8$ (X = Cl, Br or I) monolayers with considerable visible and infrared light absorption, Nanoscale **9,** 2992 (2017).

[243] B. J. Kim, B. J. Jeong, S. Oh, S. Chae, K. H. Choi, S. S. Nanda, T. Nasir, S. H. Lee, K.-W. Kim, H. K. Lim, L. Chi, I. J. Choi, M.-K. Hong, D. K. Yi, H. K. Yu, J.-H. Lee, and J.-Y. Choi, Structural and Electrical Properties of $Nb_3I_8$ Layered Crystal, Phys. Status Solidi RRL **13,** 1800448 (2019).

[244] S. Oh, K. H. Choi, S. Chae, B. J. Kim, B. J. Jeong, S. H. Lee, J. Jeon, Y. Kim, S. S. Nanda, L. Shi, D. K. Yi, J.-H. Lee, H. K. Yu, and J.-Y. Choi, Large-area synthesis of van der Waals two-dimensional material $Nb_3I_8$ and its infrared detection applications, J. Alloys Compd. **831,** 154877 (2020).

[245] J. Yoon, E. Lesne, K. Sklarek, J. Sheckelton, C. Pasco, S. S. P. Parkin, T. M. McQueen, and M. N. Ali, Anomalous thickness-dependent electrical conductivity in van der Waals layered transition metal halide, $Nb_3Cl_8$, J. Phys. Condens. Mater. **32,** 304004 (2020).

[246] F. Conte, D. Ninno, and G. Cantele, Layer-dependent electronic and magnetic properties of $Nb_3I_8$, Phys. Rev. Res. **2,** 033001 (2020).

[247] G. Cantele, F. Conte, L. Zullo, and D. Ninno, Tunable electronic and magnetic properties of thin $Nb_3I_8$ nanofilms: Interplay between strain and thickness, Phys. Rev. B G. Cantele, F. Conte, L. Zullo, and D. Ninno, Tunable electronic and magnetic properties of thin $Nb_3I_8$ nanofilms: Interplay between strain and thickness, Phys. Rev. B 106, 085418 (2022)..

[248] Z. Sun, H. Zhou, C. Wang, S. Kumar, D. Geng, S. Yue, X. Han, Y. Haraguchi, K. Shimada, P. Cheng, L. Chen, Y. Shi, K. Wu, S. Meng, and B. Feng, Observation of Topological Flat Bands in the Kagome Semiconductor $Nb_3Cl_8$, Nano Lett. **22**, 4596 (2022).

[249] D. R. Hamann, Optimized norm-conserving Vanderbilt pseudopotentials, Phys. Rev. B **88**, 085117 (2013).

[250] D. R. Hamann, Erratum: Optimized norm-conserving Vanderbilt pseudopotentials [Phys. Rev. B **88**, 085117 (2013)], Phys. Rev. B **95**, 239906 (2017).

[251] S. Grimme, Semiempirical GGA-type density functional constructed with a long-range dispersion correction, J. Comput. Chem. **27**, 1787 (2006).

[252] N. Ru, C. L. Condron, G. Y. Margulis, K. Y. Shin, J. Laverock, S. B. Dugdale, M. F. Toney, and I. R. Fisher, Effect of chemical pressure on the charge density wave transition in rare-earth tritellurides $R\mathrm{Te}_3$, Phys. Rev. B **77**, 035114 (2008).

[253] N. Ru, C. L. Condron, G. Y. Margulis, K. Y. Shin, J. Laverock, S. B. Dugdale, M. F. Toney, and I. R. Fisher, Erratum: Effect of chemical pressure on the charge density wave transition in rare-earth tritellurides $R\mathrm{Te}_3$ [Phys. Rev. B **77**, 035114 (2008)], Phys. Rev. B **77**, 249908 (2008).

[254] N. Ru, J. H. Chu, and I. R. Fisher, Magnetic properties of the charge density wave compounds $R\mathrm{Te}_3$ ($R$ = Y, La, Ce, Pr, Nd, Sm, Gd, Tb, Dy, Ho, Er, and Tm), Phys. Rev. B **78**, 012410 (2008).

[255] K. Yumigeta, Y. Qin, H. Li, M. Blei, Y. Attarde, C. Kopas, and S. Tongay, Advances in Rare-Earth Tritelluride Quantum Materials: Structure, Properties, and Synthesis, Adv. Sci. **8**, 2004762 (2021).

[256] H. Komoda, T. Sato, S. Souma, T. Takahashi, Y. Ito, and K. Suzuki, High-resolution angle-resolved photoemission study of incommensurate charge-density-wave compound $\mathrm{CeTe}_3$, Phys. Rev. B **70**, 195101 (2004).

[257] V. Brouet, W. L. Yang, X. J. Zhou, Z. Hussain, R. G. Moore, R. He, D. H. Lu, Z. X. Shen, J. Laverock, S. B. Dugdale, N. Ru, and I. R. Fisher, Angle-resolved photoemission study of the evolution of band structure and charge density wave properties in $R\mathrm{Te}_3$ ($R = \mathrm{Y}, \mathrm{La}, \mathrm{Ce}, \mathrm{Sm}, \mathrm{Gd}, \mathrm{Tb},$ and $\mathrm{Dy}$), Phys. Rev. B **77**, 235104 (2008).

[258] F. Schmitt, P. S. Kirchmann, U. Bovensiepen, R. G. Moore, L. Rettig, M. Krenz, J. H. Chu, N. Ru, L. Perfetti, D. H. Lu, M. Wolf, I. R. Fisher, and Z. X. Shen, Transient Electronic Structure and Melting of a Charge Density Wave in $\mathrm{TbTe}_3$, Science **321**, 1649 (2008).

[259] R. G. Moore, V. Brouet, R. He, D. H. Lu, N. Ru, J. H. Chu, I. R. Fisher, and Z. X. Shen, Fermi surface evolution across multiple charge density wave transitions in $\mathrm{ErTe}_3$, Phys. Rev. B **81**, 073102 (2010).

[260] R. Lou, Y. Cai, Z. Liu, T. Qian, L. Zhao, Y. Li, K. Liu, Z. Han, D. Zhang, J. He, G. Chen, H. Ding, and S. Wang, Interplay between multiple charge-density waves and the relationship with superconductivity in $\mathrm{Pd}_x\mathrm{HoTe}_3$, Phys. Rev. B **93**, 115133 (2016).

[261] E. Lee, D. H. Kim, H. w. Kim, J. D. Denlinger, H. Kim, J. Kim, K. Kim, B. I. Min, B. H. Min, Y. S. Kwon, and J. S. Kang, The $7 \times 1$ Fermi surface reconstruction in a two-dimensional $f$-electron charge density wave system: $\mathrm{PrTe}_3$, Sci. Rep. **6**, 30318 (2016).

[262] J. S. Liu, S. C. Huan, Z. H. Liu, W. L. Liu, Z. T. Liu, X. L. Lu, Z. Huang, Z. C. Jiang, X. Wang, N. Yu, Z. Q. Zou, Y. F. Guo, and D. W. Shen, Electronic structure of the high-mobility two-dimensional antiferromagnetic metal $\mathrm{GdTe}_3$, Phys. Rev. Materials **4**, 114005 (2020).

[263] S. Seong, H. Kim, K. Kim, B. I. Min, Y. S. Kwon, S. W. Han, B.-G. Park, R. Stania, Y. Seo, and J. S. Kang, Angle-resolved photoemission spectroscopy study of a system with a double charge density wave transition: $\mathrm{ErTe}_3$, Phys. Rev. B **104**, 195153 (2021).

[264] S. Lei, J. Lin, Y. Jia, M. Gray, A. Topp, G. Farahi, S. Klemenz, T. Gao, F. Rodolakis, L. McChesney Jessica, R. A. Christian, A. Yazdani, S. B. Kenneth, S. Wu, P. O. Nai, and L. M. Schoop, Sci. Adv. **6**, eaay6407 (2020).

[265] D. A. Zocco, J. J. Hamlin, K. Grube, J. H. Chu, H. H. Kuo, I. R. Fisher, and M. B. Maple, Pressure dependence of the charge-density-wave and superconducting states in $GdTe_3, TbTe_3$, and $DyTe_3$, Phys. Rev. B **91**, 205114 (2015).

[266] Y. Chen, P. Wang, M. Wu, J. Ma, S. Wen, X. Wu, G. Li, Y. Zhao, K. Wang, L. Zhang, L. Huang, W. Li, and M. Huang, Raman spectra and dimensional effect on the charge density wave transition in $GdTe_3$, Appl. Phys. Lett. **115**, 151905 (2019).

[267] Y. Okada, M. Serbyn, H. Lin, D. Walkup, W. Zhou, C. Dhital, M. Neupane, S. Xu, Y. J. Wang, R. Sankar, F. Chou, A. Bansil, M. Z. Hasan, S. D. Wilson, L. Fu, and V. Madhavan, Observation of Dirac Node Formation and Mass Acquisition in a Topological Crystalline Insulator, Science **341**, 1496 (2013).

[268] I. Zeljkovic, Y. Okada, M. Serbyn, R. Sankar, D. Walkup, W. Zhou, J. Liu, G. Chang, Y. J. Wang, M. Z. Hasan, F. Chou, H. Lin, A. Bansil, L. Fu, and V. Madhavan, Dirac mass generation from crystal symmetry breaking on the surfaces of topological crystalline insulators, Nat. Mater. **14**, 318 (2015).

[269] X. Zhou, C.-H. Hsu, T.-R. Chang, H.-J. Tien, Q. Ma, P. Jarillo-Herrero, N. Gedik, A. Bansil, V. M. Pereira, S.-Y. Xu, H. Lin, and L. Fu, Topological crystalline insulator states in the $Ca_2As$ family, Phys. Rev. B **98**, 241104 (2018).

[270] C.-H. Hsu, X. Zhou, Q. Ma, N. Gedik, A. Bansil, V. M. Pereira, H. Lin, L. Fu, S.-Y. Xu, and T.-R. Chang, Purely rotational symmetry-protected topological crystalline insulator $\alpha - Bi_4Br_4$, 2D Materials **6**, 031004 (2019).

[271] B. Wang, B. Singh, B. Ghosh, W.-C. Chiu, M. M. Hosen, Q. Zhang, L. Ying, M. Neupane, A. Agarwal, H. Lin, and A. Bansil, Topological crystalline insulator state with type-II Dirac fermions in transition metal dipnictides, Phys. Rev. B **100**, 205118 (2019).

[272] K. Wang, D. Graf, L. Li, L. Wang, and C. Petrovic, Anisotropic giant magnetoresistance in $NbSb_2$, Sci. Rep. **4**, 7328 (2014).

[273] Y.-Y. Wang, Q.-H. Yu, P.-J. Guo, K. Liu, and T.-L. Xia, Resistivity plateau and extremely large magnetoresistance in $NbAs_2$ and $TaAs_2$, Phys. Rev. B **94**, 041103 (2016).

[274] D. Wu, J. Liao, W. Yi, X. Wang, P. Li, H. Weng, Y. Shi, Y. Li, J. Luo, X. Dai, and Z. Fang, Giant semiclassical magnetoresistance in high mobility $TaAs_2$ semimetal, Appl. Phys. Lett. **108**, 042105 (2016).

[275] Z. Yuan, H. Lu, Y. Liu, J. Wang, and S. Jia, Large magnetoresistance in compensated semimetals $TaAs_2$ and $NbAs_2$, Phys. Rev. B **93**, 184405 (2016).

[276] Y. Li, L. Li, J. Wang, T. Wang, X. Xu, C. Xi, C. Cao, and J. Dai, Resistivity plateau and negative magnetoresistance in the topological semimetal $TaSb_2$, Phys. Rev. B **94**, 121115 (2016).

[277] B. Shen, X. Deng, G. Kotliar, and N. Ni, Fermi surface topology and negative longitudinal magnetoresistance observed in the semimetal $NbAs_2$, Phys. Rev. B **93**, 195119 (2016).

[278] N. Kumar, Y. Sun, N. Xu, K. Manna, M. Yao, V. Süss, I. Leermakers, O. Young, T. Förster, M. Schmidt, H. Borrmann, B. Yan, U. Zeitler, M. Shi, C. Felser, and C. Shekhar, Extremely high magnetoresistance and conductivity in the type-II Weyl semimetals $WP_2$ and $MoP_2$, Nat. Commun. **8**, 1642 (2017).

[279] R. Lou, Y. F. Xu, L. X. Zhao, Z. Q. Han, P. J. Guo, M. Li, J. C. Wang, B. B. Fu, Z. H. Liu, Y. B. Huang, P. Richard, T. Qian, K. Liu, G. F. Chen, H. M. Weng, H. Ding, and S. C. Wang,

Observation of open-orbit Fermi surface topology in the extremely large magnetoresistance semimetal $MoAs_2$, Phys. Rev. B **96**, 241106 (2017).

[280] J. Wang, L. Li, W. You, T. Wang, C. Cao, J. Dai, and Y. Li, Magnetoresistance and robust resistivity plateau in $MoAs_2$, Sci. Rep. **7**, 15669 (2017).

[281] R. Singha, A. Pariari, G. K. Gupta, T. Das, and P. Mandal, Probing the Fermi surface and magnetotransport properties of $MoAs_2$, Phys. Rev. B **97**, 155120 (2018).

[282] K. Yokoi, H. Murakawa, M. Komada, T. Kida, M. Hagiwara, H. Sakai, and N. Hanasaki, Enhanced magnetoresistance in the binary semimetal $NbAs_2$ due to improved crystal quality, Phys. Rev. Mater. **2**, 024203 (2018).

[283] T. A. Butcher, J. Hornung, T. Förster, M. Uhlarz, J. Klotz, I. Sheikin, J. Wosnitza, and D. Kaczorowski, Fermi surface investigation of the semimetal $TaAs_2$, Phys. Rev. B **99**, 245112 (2019).

[284] S. Chen, Z. Lou, Y. Zhou, Q. Chen, B. Xu, C. Wu, J. Du, J. Yang, H. Wang, and M. Fang, Magnetoresistance and Kondo Effect in Nodal-Line Semimetal $VAs_2$, Chinese Phys. Lett. **38**, 017202 (2021).

[285] G. Dhakal, M. M. Hosen, W.-C. Chiu, B. Singh, C.-Y. Huang, K. Dimitri, B. Wang, F. Kabir, C. Sims, S. Regmi, W. Neff, J. Denlinger, H. Lin, D. Kaczorowski, A. Bansil, and M. Neupane, Cleaving plane-dependent electronic structures of transition metal diarsenides, Phys. Rev. Research **3**, 023170 (2021).

[286] J. Bannies, E. Razzoli, M. Michiardi, H. H. Kung, I. S. Elfimov, M. Yao, A. Fedorov, J. Fink, C. Jozwiak, A. Bostwick, E. Rotenberg, A. Damascelli, and C. Felser, Extremely large magnetoresistance from electron-hole compensation in the nodal-loop semimetal $ZrP_2$, Phys. Rev. B **103**, 155144 (2021).

[287] C. Xu, J. Chen, G.-X. Zhi, Y. Li, J. Dai, and C. Cao, Electronic structures of transition metal dipnictides $XPn_2$ ($X =$ Ta, Nb; $Pn =$ P, As, Sb), Phys. Rev. B **93**, 195106 (2016).

[288] Y. Luo, R. D. McDonald, P. F. S. Rosa, B. Scott, N. Wakeham, N. J. Ghimire, E. D. Bauer, J. D. Thompson, and F. Ronning, Anomalous electronic structure and magnetoresistance in $TaAs_2$, Sci. Rep. **6**, 27294 (2016).

[289] G. Autès, D. Gresch, M. Troyer, A. A. Soluyanov, and O. V. Yazyev, Robust Type-II Weyl Semimetal Phase in Transition Metal Diphosphides $XP_2$ ($X =$ Mo, W), Phys. Rev. Lett. **117**, 066402 (2016).

[290] D. Gresch, Q. Wu, G. W. Winkler, and A. A. Soluyanov, Hidden Weyl points in centrosymmetric paramagnetic metals, New J. Phys. **19**, 035001 (2017).

[291] J. Chen, Y.-K. Li, J. Dai, and C. Cao, Electronic structure and topological properties of centrosymmetric $MoAs_2/WAs_2$ from first principles, Sci. Rep. **7**, 10491 (2017).

[292] Y. Shao, Z. Sun, Y. Wang, C. Xu, R. Sankar, A. J. Breindel, C. Cao, M. M. Fogler, A. J. Millis, F. Chou, Z. Li, T. Timusk, M. B. Maple, and D. N. Basov, Optical signatures of Dirac nodal lines in $NbAs_2$, Proc. Natl. Acad. Sci. **116**, 1168 (2019).

[293] C. Sims, M. M. Hosen, H. Aramberri, C.-Y. Huang, G. Dhakal, K. Dimitri, F. Kabir, S. Regmi, X. Zhou, T.-R. Chang, H. Lin, D. Kaczorowski, N. Kioussis, and M. Neupane, Termination-dependent topological surface states in nodal-loop semimetal $HfP_2$, Phys. Rev. Mater. **4**, 054201 (2020).

[294] M. S. Alam, P. K. Tanwar, K. Dybko, A. S. Wadge, P. Iwanowski, A. Wiśniewski, and M. Matusiak, Temperature-driven spin-zero effect in $TaAs_2$, J. Phys. Chem. Solids **170**, 110939 (2022).

[295] R. Lou, Y. Wang, L. Zhao, C. Xu, M. Li, X. Chen, A. Zhang, Y. Huang, C. Cao, G. Chen, T. Xia, Q. Zhang, H. Ding, and S. Wang, Electronic structure and open-orbit Fermi surface topology in isostructural semimetals $\mathrm{NbAs_2}$ and $\mathrm{W_2As_3}$ with extremely large magnetoresistance, Appl. Phys. Lett. **120**, 123101 (2022).